Contributions to the understanding of meso/submesoscale turbulence and their impact on the ocean functioning

Xavier Capet

UNIVERSITE PARIS 6 PIERRE ET MARIE CURIE

Contributions to the understanding of meso/submesoscale turbulence and their impact on the ocean functioning

THESE D'HABILITATION A DIRIGER DES RECHERCHES

Specialité : Océanographie Physique

Défendue par

Xavier Capet

Juin 2015

Jury :

Rapporteurs :	V. Garçon	- LEGOS
	A. Wirth	- LGGE
	H. Giordani	- CNRM
President :	P. Bouruet-Aubertot	- LOCEAN
Examinateurs :	P. Klein	- LPO
	Y. Morel	- LEGOS

Contents

Chapter 1

Introduction

This manuscript is personal reflexion on the research area I have been most involved for the past 15 years. The studies I have contributed to are in cited in bold. To help the reader aach section starts with a short summary, also in bold.

Over the course of my (still) short career in physical oceanography the field has undergone substantial transformations, say from the mid 1990's as I was about to start my PhD, until now. These transformations are briefly described in this section which help place my contribution in a broader perspective.

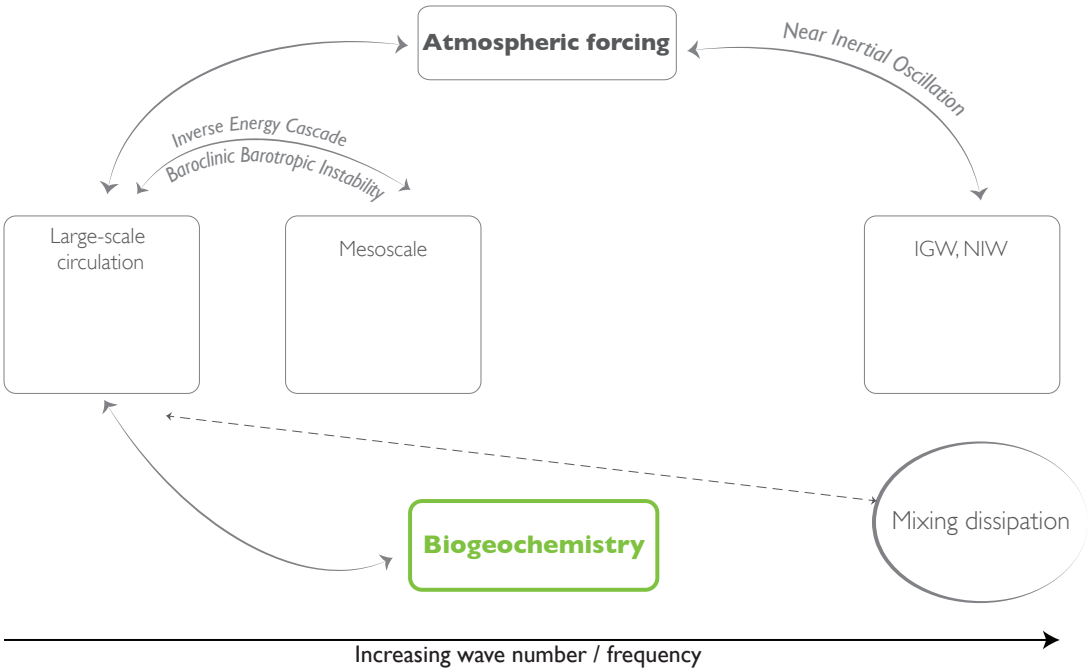

Figure 1.1: Schematic scale representation of oceanographic research in the early/mid 1990's.

Schematically, I would divide oceanographic research in the mid 1990's in three

poles ((Fig. 1.1): large scale circulation and ocean functioning; mesoscale turbulence (with a dominance of process studies); and internal gravity waves and their role on mixing. A connection between these poles that was actively investigated and had been put on firmer ground was on the role of mesoscale eddies in the climate system (Gent and McWilliams, 1990; Gent et al., 1995). Retrospectively the connection between the interior ocean functioning and small scale mixing was quite rudimentary, although perhaps less so in the minds of the observationalists (Kunze and Sanford, 1996; Peters et al., 1995) than in the OGCM (Ocean General Circulation Models) implementations (Large et al., 1994). Some circumstantial links were also established between the mesoscale activity and near-inertial wave breaking (Lueck and Osborn, 1986; Kunze, 1986), with substantial theoretical developments to rationalize them (Kunze, 1985; Young and Jelloul, 1997). Overall, even though many pieces of the puzzle were known they had not made their way into OGCM parameterizations. As for biogeochemical activity it was essentially considered in relation to basin-scale circulation patterns although work on mesoscale had been initiated observationally (Tourbillon, 1983; Lochte and Pfannkuche, 1987) and, more tentatively, numerically (Smith et al., 1996; Dadou et al., 1996).

The current situation is fundamentally different in many respects (Fig. 1.2):

1. A large fraction of the community is now directly involved with the mesoscale in their regional context *i.e.,* regional mesoscale regimes and their temporal variability are becoming fairly well known. In certain circumstances ocean individual mesoscale events can be described with a level of details that is more customary in atmospheric sciences (Hamilton et al., 2011). Deviations from the canonical Gent and McWilliams (1990) are numerous and partly justify the ongoing transition toward eddy resolving OGCMs (as opposed to a complete reliance on parameterization of eddy effects). Modeling platforms have undergone major improvements that have strongly benefited realistic modeling of coastal systems (compare for example the modeling work of Batteen (1997), Marchesiello et al. (2003) and Rose et al. (2015) in the California current system).

2. Research has been and remains very active on submesoscale since the early 2000's. By submesoscale we refer to dynamical features whose typical scale is smaller than the deformation radius. The current vision tends to emphasize

upper ocean submesoscale fronts and eddies (see chapter. 2) but the role of interior submesoscale vortices, which have been observed for a long time, may also be important.

3. Dissipation/mixing intermittency and spatial variability is under intense investigation. The aim is to quantify their intensity for each important water mass of the world ocean, in relation to specific mechanisms (Ito and Marshall, 2008; Oka and Niwa, 2013; Melet et al., 2013; de Lavergne et al., 2015). Ultimately, this would provide reliable region dependant (or preferably process-based) map of vertical diffusivities K_v to be incorporated in OGCMs.

4. atmosphere-ocean coupling is now considered on a much broader range of scales. In particular ocean feedbacks operative at mesoscale are a subject of considerable interest. Subtle effects of atmospheric forcings on submesoscale have also been uncovered.

5. BGC applications provide a strong motivation and guidelines to the developments pertaining to 1 and 2. More generally there has been a very strong integration effort between physics and BGC over a broad range of scales.

I have contributed sometimes modestly and sometimes more significantly to the development of these new reseach threads. One way to classify my contributions with some acceptable degree of coherence is based on both the scale range of processes and methodology:

Processes and scales:

✓ submesoscale processes and their role in the ocean functioning at regional scale. My contributions to this include in-depth investigations of submesoscale regimes (Capet et al., 2008e,f,d,a; Klein et al., 2008a) and of their consequences (see Chapter 2).

✓ description and understanding of regional current systems, with an emphasis on the role of mesoscale turbulence (Capet et al., 2008b; Colas et al., 2012, 2013; Vic et al., 2014) (see Sec. 3.1), ocean response to fine-scale details of the atmospheric forcings (Capet et al., 2004), downscaling of large scale climate anomalies (Colas et al., 2008; Montes et al., 2010), and biogeochemical/ecosystem implications (Carr et al., 2008)

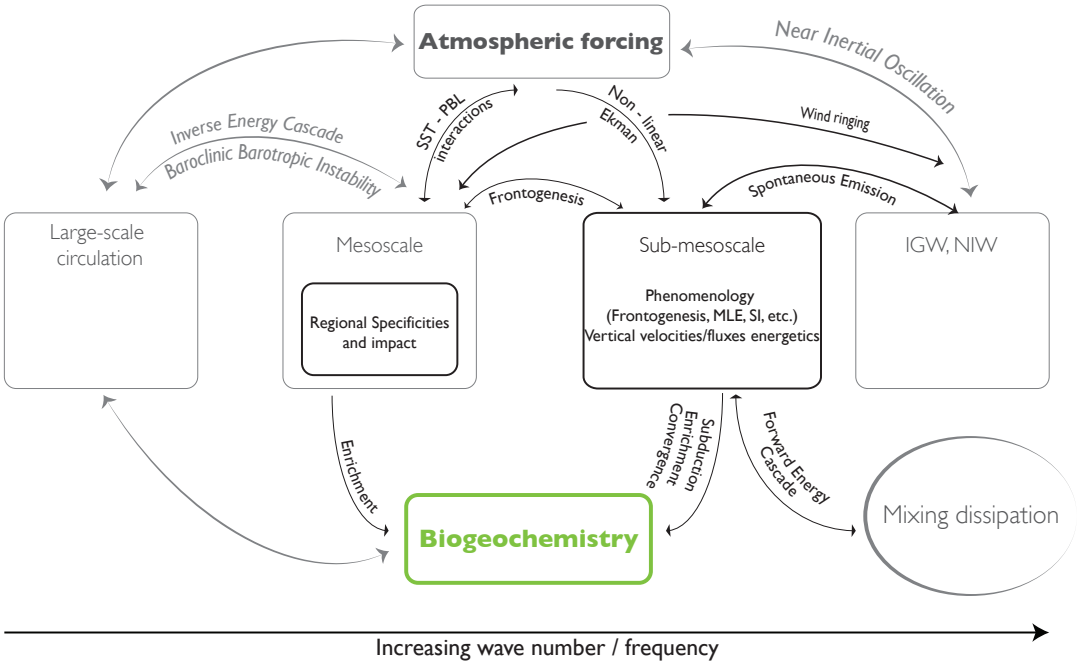

Figure 1.2: Schematic scale representation of oceanographic research in 2015.

✓ new research topics I have recently started working on and for which my track record is slim are inertia-gravity waves (as a dynamical component that shape nearshore dynamics along the West African coast, Capet et al., 2015b) and near-inertial motions (as contributors to ocean interior dissipation and mixing, Jouanno et al., 2015). Both imply a descent in scales compared to what I have been doing so far. The latter is a contribution to the SMOC project (Submesoscale Ocean modeling for Climate, ANR Jeune Chercheur 2012-2015) that I have led. Details can be found in Sec. 2.6. The former subject is studied in the context of the AWA project (integrated approach of the coastal ecosystems off West Africa, http://www.awa-project.org/; https://skyros.locean-ipsl.upmc.fr/ Xavier.Capet/WA/WA.html in french). Recent findings are described in Sec. 3.2. Investigations of the interactions between subinertial and near-inertial or superinertial motions are an important aspect of my research perspectives presented in sections 2.7 and 3.3.

Methodology:

✓ most of my research has involved numerical modeling with more or less ex-

treme forms of idealization. I have early on developed an interest for idealized model frameworks (see Insert 1; **Capet et al., 2002**; **Capet and Carton, 2004**; **Capet et al., 2008c**; **Duarte et al., 2011**; **Roullet et al., 2012**; **Capet et al., 2015a**), interventions to modify the real ocean geometry/bathymetry/forcings (Capet et al., 2008e; Vic et al., 2014), and sensitivity studies in general (Capet et al., 2004, 2008b,e). These are all essential aspects of my work. In many circumstances, these approaches offer insightful perspectives on the ocean functioning.

✓ contribution to the evaluation and refinement of model skills and approaches (for regional and process studies). The sensitivity of model simulations to nearshore wind profiles (Capet et al., 2004) was part of a larger investigation intended to evaluate model skills at reproducing coastal circulation off central California. This grander goal has led to more specific studies such as Colas et al. (2013) but the manuscript initially envisioned (P. Penven, 2002 personal communication) has never been written. An enduring bias has been the insufficiently steep thermocline slope at Calcofi Line 67, mainly during the spring season when the system is most frontal (see Fig. 1.3). It has stimulated a long series of sensitivity experiments and model improvements but remains to this day. The bias is, in my opinion, not major. It has not prevented us from learning instructive lessons. The high standard of model realism seeked during over a decade is to put to the credit of J. C. McWilliams and his successive Central California researchers (P. Marchesiello, P. Penven, J. Molemaker, F. Lemarié, and myself). On the other hand, it might be about time to try to report on this robust model bias. Other ventures in model assessment/improvement territory have been with the COMODO team and NEMO developers G. Madec and S. Masson). Being most relevant to submesoscale turbulence, they are briefly mentionned in chapter 2 (see Figs. 2.13 and 2.16 and related text), while two manuscripts are under review (Jouanno et al., 2015; Soufflet et al., 2015).

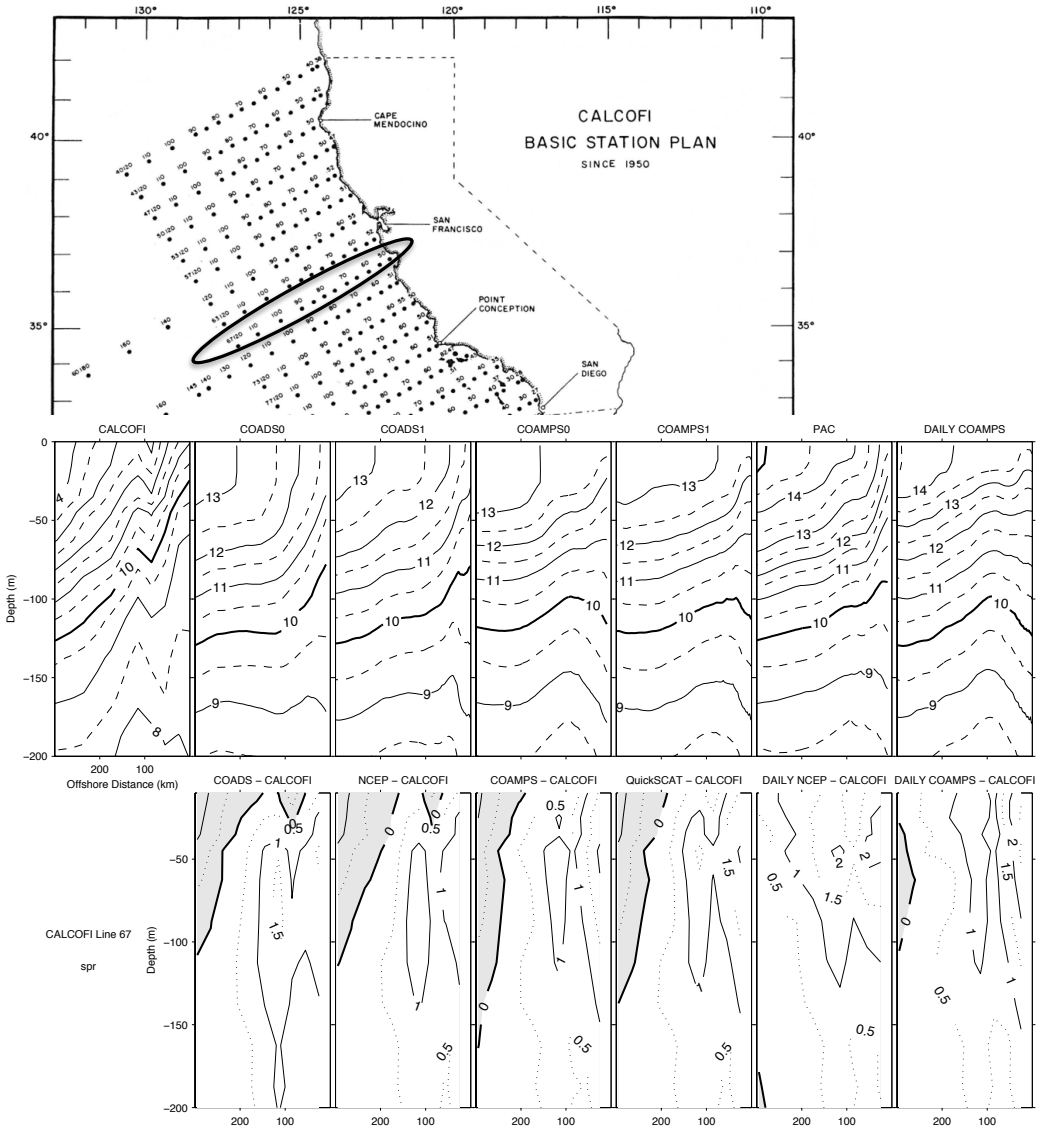

Figure 1.3: Top: Calcofi observation grid with Line 67 encircled in black. Bottom: Temperature across-shore section along Line 67 from 0 to 300 km offshore for Calcofi (upper left) and six different numerical experiments testing the sensitivity of ROMS thermal structure to winds (2 variants of COADS, and 3 variants of a mesoscale atmospheric simulation outputs including daily winds) and lateral oceanic boundary conditions (the fifth column). Overall a coastal bias of $\sim$ 1.5-2^{o}C is systematically present.

Insert 1: PhD work

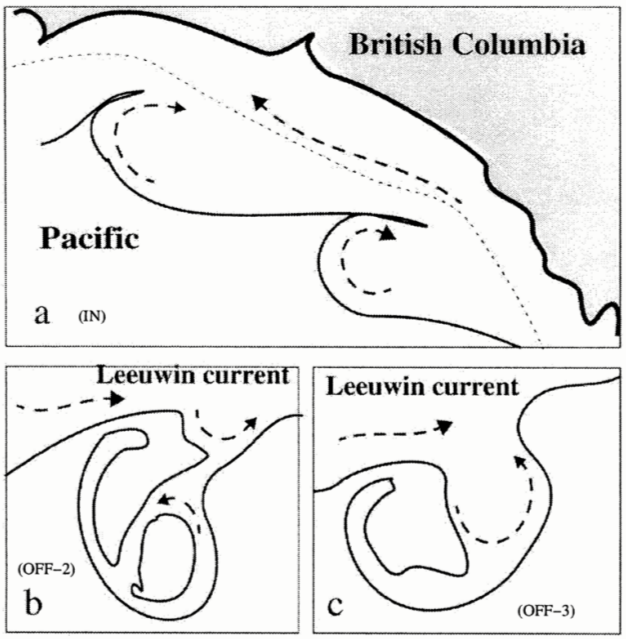

Sketch of different eddy formation from boundary currents as suggested by satellite SST maps. In each case, the solid thick line indicates the approximate location of the largest temperature gradient. Arrows indicate water motion expected by the authors. (a) Part of a six-vortex string whose formation is reported by Thomson and Gower (1998). The coast (bold line), 1000-m isobath (dashed line) are indicated. (b,c) Formation of the structure respectively labeled "A" and "B" through destabilisation of the Leeuwin Current (Griffith and Pearce, 1985). From Capet et al, 2004a.

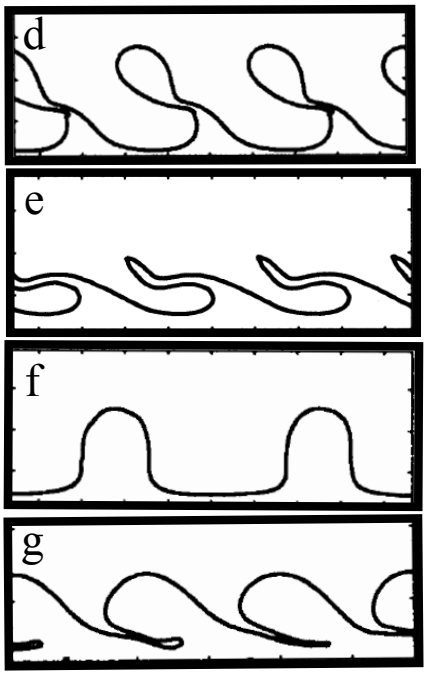

Nonlinear evolution of the interface between onshore and offshore waters in the upper layer of a 2-layer QG model with piecewise constant potential vorticity. Four situations corresponding to different horizontal and vertical velocity shears are represented. The coast is situated at the bottom of each panel. Note the resemblance between panels a and g, b and d, c and f. From Capet et al, 2004a.

During my PhD I have studied how very simple models and frameworks can give insight into the destabilisation processes giving rise to mesoscale activity. This work was in the particular context of continental slope currents subjected to parallel flow instabilities (baroclinic, barotropic). One important result was that the basic flow (mean or prior to the destabilization) contains useful information with respect to how the flow is going to behave nonlinearly and more specifically how the shape of the unstable wave will evolve. The figures above represent various situations of ``boundary current destabilization" that exchange waters with the offshore in ways that involve distinct meso or submesoscale types of structures. This approach to baroclinic/barotropic instability is insightful everytime a well-defined ocean current is subjected to baroclinic/barotropic instabilities.

This is for example the case with the Mauritanian current that flows offshore of the Senegale coast. At times it exhibits clear manifestations of instability modes that also involve the equatorward upwelling flow.

The California current mesoscale activity that accompanies the quasiwide unstable zone is one particular case where my PhD approach to baroclinic/barotropic instability is not useful * Fig California CS qque part ***.**

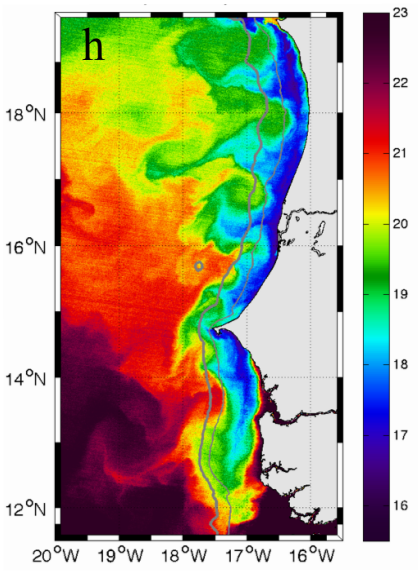

Nighttime MODIS-A SST image taken on 21 February 2013. Note how upwelling and offshore waters interlace through eddies and filaments.

Chapter 2

Submesoscale frontal turbulence

Contents

This Chapter describes my research activities on submesoscale turbulence. Significant space is dedicated to reviewing the studies of others, insofar as they address the same research questions I have been interested in. My main submesoscale collaborators have been P. Klein, J. McWilliams, G. Roullet, J. Molemaker and J. Jouanno.

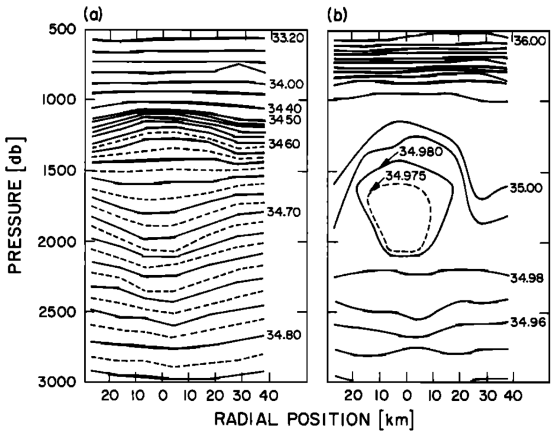

Figure 2.1: contour plots of a) potential density and b) salinity (per mil) across a subthermocline SCV observed during the Local Dynamics Experiment (Elliott and Sanford, 1986). Reproduced from McWilliams (1985).

2.1 Submesoscale and upper ocean frontal intensification

Until the early 2000s the term sub-mesoscale was sporadically used to describe ocean eddies whose size is of the order of R_d where R_d is the first internal deformation radius (McWilliams, 1985). Such submesoscale eddies or submesoscale coherent vortices are essentially balanced features [1] that populate the ocean interior and in particular the thermocline region (see Fig. 2.1 for an example). So defined submesoscale vortices have a weak or no surface signature and long life times.

From Levy et al. (2001) onward submesoscale increasingly refers to features whose dynamics is fundamentally different. Over the last 15 years rapid accumulation of HR satellite images from different sources and increased resolution in numerical models have led to the realization of the ubiquity of rapidly evolving 1-10 km scale ocean tracer contrasts (temperature, salinity, density, biogeochemical properties) or fronts. Note that it is the cross front scale that is in the range 1-10 km while alongfront invariance can be preserved over much longer distances or not depending on conditions (see Fig. 1).

[1] "Balanced" features are ones that are appropriately described in a balance model, *i.e.*, a set of equations that filters out fast oscillations and describes the slow evolution of a system. Quasi-geostrophy is the usual balance model to most physical oceanographers.

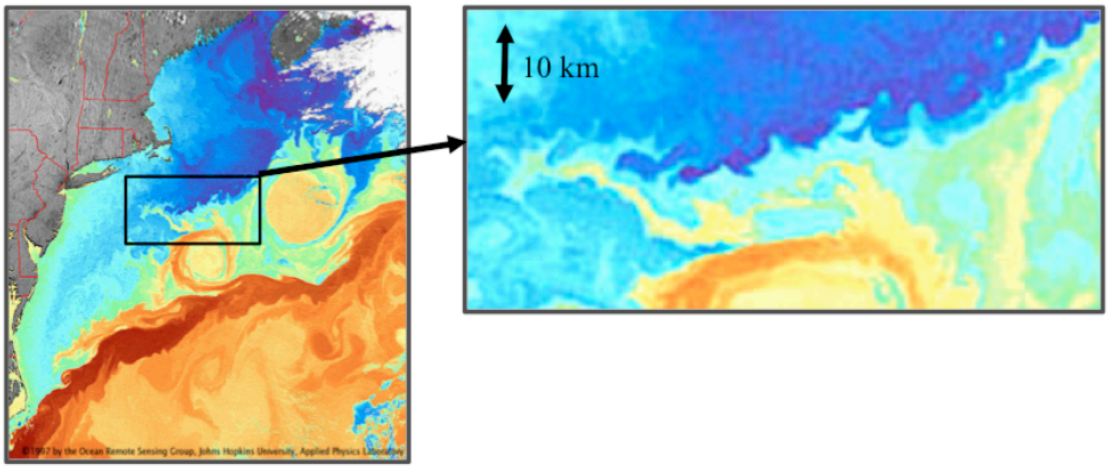

Figure 2.2: AVHRR SST image over a region off the U.S. East coast. The left panel depicts the mesoscale turbulence that accompanies the Gulf Stream while the blow-up shows the presence of fine-scale frontal activity, especially in the vicinity of the eddies.

Preferential locations for the presence of these structures are deformation regions, between/around mesoscale eddies, *i.e.,* where the straining field is conducive to frontogenesis (Hoskins, 1982). Consistent with the mechanism of frontogenesis (see Sec. 2.5) submesoscale fronts also exhibit a large degree of near-surface intensification close to the ocean surface, typically within a few tens of meters from the ocean surface, and in particular within the oceanic boundary layer when there is one.

In this work the terminology "submesoscale" will be used as a shorthand to refer to 1-10 km scale frontal upper-ocean intensified structures or turbulent activity

The ubiquity of submesoscale fronts is illustrated with several AVHRR SST images in the Gulf Stream region: fronts are present in many places, *e.g.,* surrounding spiral vortices (Munk et al., 2000), or grouped in pairs to form filaments (Flament et al., 1985), with more or less alongfront irregularity.

The remainder of this chapter reviews the recent progress that has been made on submesoscale dynamics and puts the emphasis on my contribution and view on submesoscale. Sec. 2.2 reconsiders the results and role played by the in-depth investigation of California current submesoscale regime (my first experience in submesoscale territory). The issue of idealized approaches of submesoscale turbulence, diversity of submesoscale regimes, submesoscale vertical velocity and fluxes and energetics of the submesocale are then successively discussed.

2.2 The transition from mesoscale to submesoscale

This section discusses the contribution of Capet et al. (2008a),Capet et al. (2008b) and Capet et al. (2008d) to the study of submesoscales.

Numerous in situ observation experiments have taken place in frontal regions and demonstrated the importance of the processes that were taking place there, in particular with regard to vertical exchanges of ocean properties ; numerical models have transitioned from being eddy-permitting (a few grid points per deformation radius) to fully eddy-resolving, *i.e.,* dynamics in the straining regions at edge of mesoscale eddies can be represented in details. Thanks to these parallel and often combined efforts reinforced by progress on theory we have considerably improved our general understanding on submesoscale and their role in the ocean.

My primary contribution to this effort has been a series of three papers published in 2008 **(Capet et al., 2008e,f,d)** whose content is summarized below. This contribution has matured in the context of the Climate Process Team "Eddy Mixed Layer Interactions" (CPT EMILIE, PI: R. Ferrari) with the research carried out by B. Fox-Kemper and coauthors (Boccaletti et al., 2007; Fox-Kemper et al., 2008; Fox-Kemper and Ferrari, 2008) on mixed layer instabilities. It also took advantage of recently published work that had recently laid out insightful concepts and frameworks to rationalize upper ocean fine-scale turbulence (Lapeyre and Klein, 2006; Lapeyre et al., 2006), including on its modifications by atmospheric forcings (Thomas and Lee, 2005; Thomas, 2005).

The aim of this series of articles was to present the turbulent fields statistics (rms, turbulent correlations, power spectral density ...); describe the dominant dynamical processes associated with submesoscale flow structures; assess the degree to which existing simpler models (interior quasigeostrophic, surface quasigeostrophic, and balanced dynamics) are apt at representing the submesoscale turbulence regime; and analyze the energetics aspects of submesoscale flows. In other words, the intent was to help establish a conceptual framework for the submesoscale regime resembling the one we find useful to conceptualize mesoscale turbulence. Indeed the ubiquity of mesoscale eddies in the ocean is associated with a preferred length scale — the first baroclinic deformation radius R_1 — where kinetic energy tends to accumulate. Quasigeostrophic theory (*e.g.,* Pedlosky, 1987) provides a framework for understanding this behavior as a combination of inverse energy cascade and/or forward potential enstrophy cascade on scales smaller than R_1; inhibition of inverse cas-

cade by topography and Coriolis-frequency gradients to scales much larger than R_1; potential-to-kinetic energy conversion around R_1; and a large potential-to-kinetic energy partition ratio on larger scales. It is useful to recall that this framework valid at scales of tens of kilometers may not a priori be applicable at finer scales. Scale invariance is a fairly common characteristic of non-linear systems. It refers to the fact that the properties of the system (eg, the characteristics of its temporal evolution or the way it occupies the physical space) follow scaling laws, *i.e.,* they are similar across the range of scales on which the invariance manifests itself. In the ocean as in many geophysical situations, the dominant balance of forces within the fluid is scale-dependant as are, consequently, the turbulence statistics and underlying driving processes. It follows that the turbulence at horizontal length scales of the order of one kilometer cannot be explained with the theories developed for turbulent motions on scales of tens of kilometers. Understanding the transitions/interactions between the successive turbulent regimes is also a source of complexity.

In **Capet et al. (2008e,f,d)** a suite of computational simulations for an idealized subtropical, eastern-boundary, upwelling current system was analyzed for the emergent submesoscale flows that arise once the horizontal grid resolution increases to $\mathcal{O}(1)$ km. The high resolution solutions (1.5 km and 0.750km horizontal resolution) exhibit abundant near-surface submesoscale features especially in between the mesoscale eddies. These features are conspicuous in tracer, velocity, and vorticity fields with a high degree of correlation among them (Fig. 2.3).

The salient aspects of CCS numerical solutions with dx $\approx$ 1 km are the correlations between vertical velocity w and the thermohaline fields (*i.e.,* potential temperature, salinity, and potential density; (T, S, ρ)) at the submesoscale, mainly confined in the $\approx$ 30 m deep mixed layer. Underlying the correlations is a $\approx$ 10-fold increase in vertical velocity rms in that depth range and limited changes below. These correlations imply significant vertical thermohaline eddy fluxes, absent or much weaker at lower resolutions. They also imply that baroclinic instability is a key process fueling submesoscale activity through available potential energy (APE) to eddy kinetic energy (EKE) conversion. The mixed-layer confinement of that release can be rationalized using mixed-layer instability theories that were in development (Boccaletti et al., 2007; Fox-Kemper et al., 2008) as I was analyzing the CCS submesoscale solutions. Geostrophic/ageostrophic flow decompositions and also a more elaborate estimation of flow imbalance revealed the smallness of ageostrophic effects, besides

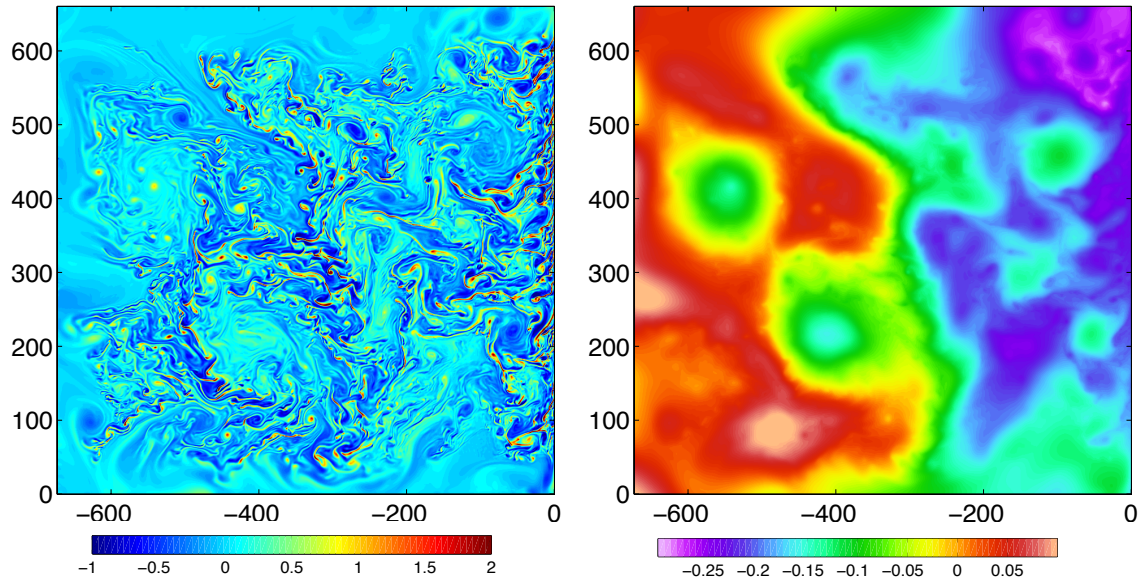

Figure 2.3: Surface vorticity (normalized by $f_0 = 8\ 10^{-5}\ s^{-1}$, left) and sea level at $t = 120$ days (right) in the numerical simulations for an idealized California current with rectilinear coasline and 4000 m deep flat bottom). Note the submesoscale filaments and vortices concentrated outside the mesoscale eddy cores and the dominance of cyclonic vorticity over anticyclonic (with a colorscale not centered on 0). Distances along x- and y-axis are in km. Reproduced from (Capet et al., 2008e).

wind driven surface currents. This had not been widely anticipated; some expectations had been that new forms of ageostrophic instabilities (Molemaker et al., 2005) would set off at such scales. It turns out that it is only around a few hundred meters or less that ageostrophic effects become dominant (Taylor and Ferrari, 2010; Molemaker et al., 2010) (this had also been anticipated in **Capet et al. 2008d** based on simple extrapolations) and various forms of ageostrophic instabilities can become important depending on the conditions.

Perhaps the most novel aspect of Capet et al. 2008 (Parts 1-3) was to consider a "realistic" configuration in which a variety of processes that had previously been considered in isolation were free to express themselves. This has for example allowed us to: contribute to establishing standards in terms of spectral distribution of EKE (Fig. 2.4) and tracer variance against which observations could be confronted (Le Traon et al., 2008; Xu and Fu, 2012; Callies and Ferrari, 2013; Qazi et al., 2014); confirm the importance of mixed-layer eddies and instabilities for submesoscale frontal turbulence; demonstrate the statistical significance of the modulation of frontal intensity by winds (Thomas and Lee, 2005; Thomas, 2005) confirm the complexity of the frontogenetic processes at work; downplay the importance of ageostrophic instabilities whose relevance to the ocean had been a primary motivation for this work (McWilliams et al., 2001; Molemaker et al., 2005). An advantage of the quasi-realistic setting is that the submesoscale statistical description proposed in these papers has since then been experimentally tested, and for the most part widely accepted (Pallàs-Sanz et al., 2010a,b; Johnston et al., 2011; Kim et al., 2011; Cole et al., 2010; Chavanne et al., 2010; Shcherbina et al., 2013). It has also been demonstrated that many of its conclusions hold in more realistic numerical configurations, for the California current (Koch et al., 2010) or other regional systems **(Marchesiello et al., 2011)**,(Koszalka et al., 2009; Sasaki and Klein, 2012; Mensa et al., 2013; Romero et al., 2013; Zhong and Bracco, 2013; Veneziani et al., 2014; Rosso et al., 2014). Among the noteworthy differences are the emission of near-inertial waves in the simulations of Zhong and Bracco (2013) and the net restratifying effect due to submesoscale in Veneziani et al. (2014), due to their synoptic forcings.

2.3 Submesoscale regimes

In this section we draw the attention on the fact that submesoscale tracer

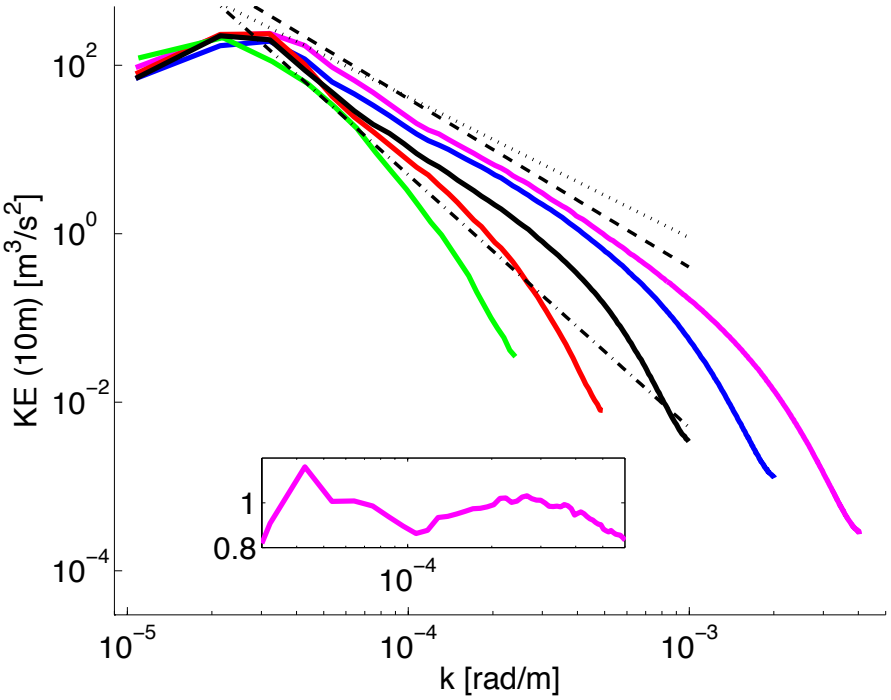

Figure 2.4: KE spectra for the horizontal velocity $\mathbf{u}_h$ fluctuations at 10m depth as a function of horizontal wavenumber magnitude, $k = |\mathbf{k}_h|$ The five solid lines correspond to spectra for the different simulations with the wavenumber range increasing from $\Delta x = 12$ km to $\Delta x = 750$ m (i.e., horizontal grid scale decreasing from 12 to 0.75 km. For comparison the straight lines indicate -5/3 (dotted), -2 (dashed), and -3 (dot-dash) spectrum slopes. Increasingly shallower spectra are one evident manifestation of the frontal intensification allowed as resolution increases. The spectrum for $\Delta x = 750$ m multiplied by k^2 is plotted in the inset with a linear ordinate scale over the indicated intermediate k range. Reproduced from (Capet et al., 2008d).

arrangements (and statistics) vary depending on the environmental conditions. We also describe a peculiar regime arising over weakly stratified continental shelves because submesoscale activity is generated but mesoscale eddies are absent. This regime may be important in mid- and high-latitude coastal areas.

2.3.1 Toward a classification of submesoscale regimes

Some exploration of the submesoscale activity arising in diverse situations, regional or temporal) has led to Capet et al. (2008a) and Marchesiello et al. (2011)[2]. Both studies have enriched my understanding of submesoscale turbulence and have contributed to a broader effort aimed at exploring and establishing what could be seen as a typology of submesoscale regimes. This effort is still ongoing. The diversity of submesoscale regimes is suggested in Fig. 2.5 using surface tracer snapshots for model solutions I have worked with. How can these distinct front arrangement be rationalized ? Submesoscale surface fronts develop under different types of stirring conditions that can be schematically categorized following Scott (2006) (see also Bartello 2000):

1. stirring by mesoscale eddies; the straining field associated with mesoscale eddies leads to folding, elongation and compression of tracer features (McWilliams 1984). Tracer contours tend to organize into thin filaments (see Fig. 2.5a). In the submesoscale range, the underlying cascade of tracer variance toward smaller scales is nonlocal in wavenumber, as it is governed by velocities at larger (meso)scales. An archetypal regime with stirring by mesoscale eddies is the interior QG turbulence regime.

2. stirring by submesoscale eddies; submesoscale mixed layer baroclinic instabilities (Boccaletti et al., 2007; Fox-Kemper et al., 2008) can lead to submesoscale turbulence that will also act on the tracer field and contribute to the formation of submesoscale fronts and eddies. In the submesoscale range, the underlying cascade of tracer variance toward smaller scales is local in wavenumber, as it is governed by submesoscale velocities. An archetypal exemple is represented in

[2]Comparison of several eastern boundary systems in terms of potential submesoscale content is proposed in Colas et al. (2013) based on the extrapolation of analyses obtained from mesoscale resolving numerical solutions.

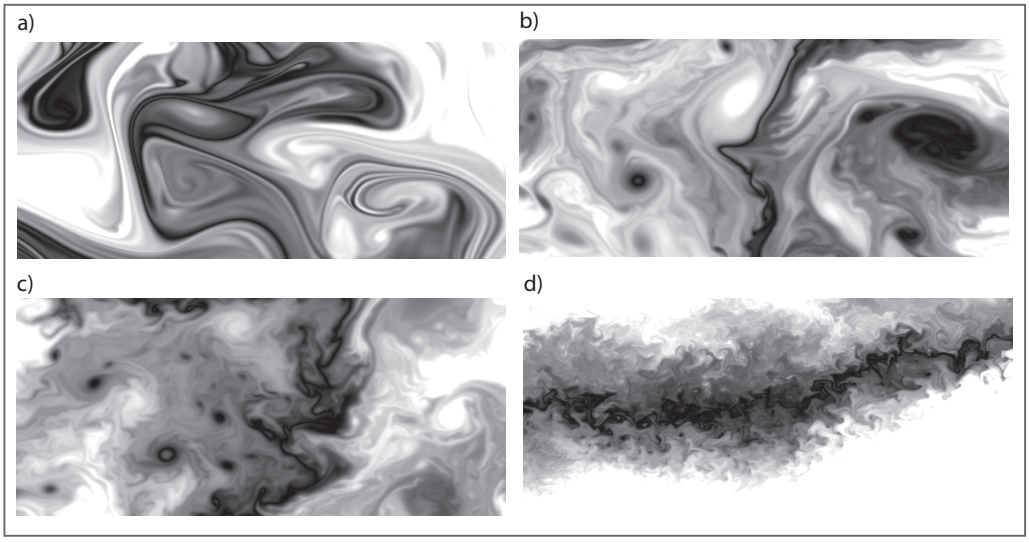

Figure 2.5: Surface density arrangements resulting from different meso/submesoscale turbulent regimes. The scales in x and y are identical between different panels (approximately 500 km x 250 km). The choice of the color scale is arbitrary. In a nutshell, when turbulence is driven by interior baroclinic instability with limited surface density contrasts (a) surface density is stirred into long filaments around mesoscale vortices generated by this instability. In the real ocean temperature (and density) is often inhomogeneous at the surface which yields intensified kinetic energy in the submesoscale range. Surface tracer fields can then take very different appearances depending on whether mixed layer depth is large and mixed layer instabilities are very energetic (c) or not (b). In idealized simulations of the Argentine shelf wintertime dynamics (Capet et al., 2008b), O(100) km mesoscale turbulence is absent a while submesoscale mixed-layer instability is very intense, which is reflected by the dominance of kilometer scale variability in SST (d).

Fig. 2.5d and corresponds to the temperature field for a weakly stratified continental shelf over which mesoscale eddies are absent and short-scale baroclinic activity is intense. This example is further discussed below.

Note that flows with minor differences in spectral distribution of KE lead to the situations shown in Figs. 2.5b,c, that clearly differ in the appearance of their submesoscale tracer features (they are more densely packed and have more convoluted filamentary structures in panel c). Lagrangian statistics, *e.g.,* of relative dispersion or Lyapunov exponents, may be useful to quantify the submesoscale influence and classify submesoscale regimes (Lumpkin and Elipot, 2010; Schroeder et al., 2011; Özgökmen et al., 2011, 2012; Zhong and Bracco, 2013; Poje et al., 2014).

2.3.2 Application to coastal environments and submesoscale seasonality

Because water depth is limited in coastal environments they are characterized by small Rossby deformation radii of the order of a few kilometers or less. A key implication is that mesoscale structures whose length scale is by definition of the order of a few deformation radii are no bigger than typical open ocean submesoscale structures and tend to behave similarly (importance of ageostrophic effects and large Rossby numbers in particular). Although this convention is not universally accepted I favor the use of the terminology "submesoscale" to qualify 1-10 km scale fronts and vortices that populate continental shelves.

In Capet et al. (2008a) the dynamics of the Argentinian shelf is modeled with a focus on its seasonal variability. Mesoscale resolving simulations ($\Delta x \approx 5$ km) forced using climatological forcings exhibit limited variability below seasonal time scales. In constrast solutions at resolution O(1 km) reveal major differences between summer and wintertime submesoscale activity (see a wintertime surface temperature in Fig. 2.5d) These differences are rationalized based on the theoretical work by Fox-Kemper et al. (2008) on mixed layer baroclinic instability. Shelves under sustained destabilizing atmospheric forcings can turn into canonical manifestations of the idealized mixed layer instability regime considered by Fox-Kemper et al. (2008). This is the case over the Argentinian shelf where the growth of these instabilities is favored by environmental conditions in fall and winter (deep surface boundary layer and cross-shelf density gradient).

Submesoscale eddies, like mesoscale eddies, are a cause of lateral stirring, only with lesser intensity as can be easily understood intuitively using a weakly perturbed situation. With typical length scales of the order of 1 km and $u'_{rms} \sim 0.1$ m s^{-1} diffusivity values of the order of 100 m^2 s^{-1} can be expected to accompany submesoscale turbulence. In Capet et al. (2008a) a more rigorous estimation yields horizontal diffusivities in the range 30-100 m^2 s^{-1} with significant modulations related to bathymetric accidents (areas with water depth shallower than ~ 50 m where friction strongly controls the flow have low diffusivities). Such values are small in regard to typical open ocean diffusivities (associated with mesoscale turbulence, O(1000 km)) but they are large compared to typical shelf diffusivities, 10 m^2 s^{-1} or less (Sundermeyer and Ledwell, 2001). Note that diffusivities due to submesocale motions can be much weaker in situations of mesoscale stirring and/or shallow mixed layer

(Nencioli et al., 2013).

In addition to contributing to tracer redistribution (mainly salt over the Argentinian shelf) lateral dispersion by the submesoscale may have profound effects on marine ecosystems' functioning. A Lagrangian experiment conducted in Capet et al. (2008a) demonstrates the effectiveness of submesoscale flows at concentrating buoyant organisms about fronts and eddies (see Fig. 2.6). The process is so rapid that it is likely to also aggregate organisms with partial buoyancy (e.g., some phytoplanktons), and may explain some aspects of life distribution patchiness on scale $\sim$ 1-10 km.

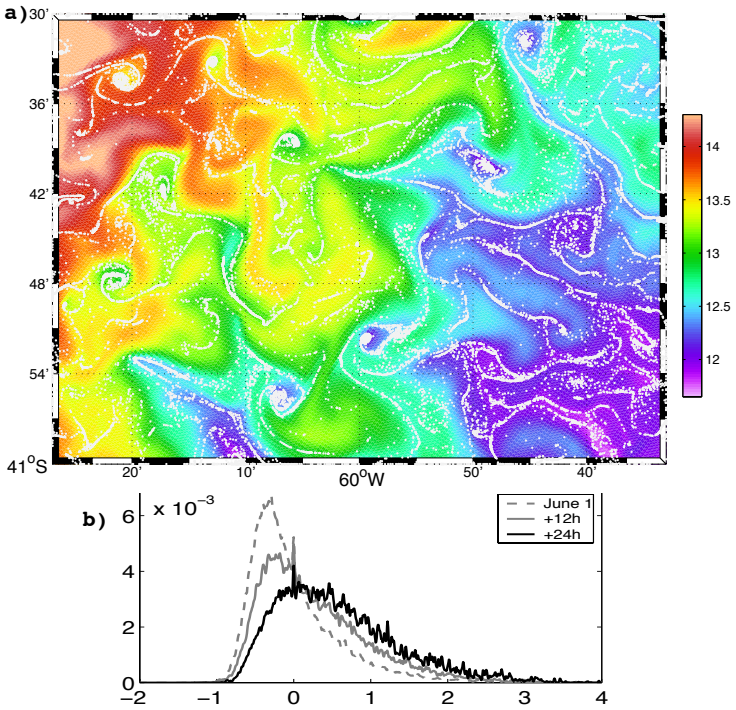

Figure 2.6: a): SST and drifter location (white dots) 24 hours after their simultaneous release at every grid node of an Argentinian shelf high resolution solution (Capet et al., 2008a). Particules are supposed to have positive buoyancy and they remain at the ocean surface. Note the accumulation of particles within cold-core spiral eddies (Munk et al., 2000) and on the cold side of temperature fronts. b): Vorticity pdf at drifter locations at release time (1 June), 12 and 24 h later . Since the drifters are evenly distributed at release the June 1st 12AM distribution is representative of the eulerian vorticity pdf and it is skewed toward anticyclonic vorticity that occupies most of the inter-fronts areas (not shown). Changes of the pdf are minor after 24 hours.

These findings are probably relevant to other mid-latitude shelves, such as the

Middle Atlantic Bight, for which AVHRR image processing reveals enhanced frontal activity in winter (Ullman and Cornillon, 1999) (see Fig. 2.7). These ideas have reached the coastal modeling community. I am co-supervisor of a PhD on the frontal activity in the Bay of Biscay **(Yelekci et al., 2014)**. The role of the Louisiana shelf submesoscale activity is a subject of great interest for its role in the dispersion of surface pollutants released in the environment as a consequence of the Deep Water Horizon oil spill (Poje et al., 2014). How the inclusion of submesoscale activity will affect our understanding of shelf dynamics is still uncertain and will certainly vary from place to place (Schroeder et al., 2011). Like anywhere in the ocean submesoscale turbulence may be an important process for mixed layer restratification and overall buoyancy budget. This should be the case at mid- and high- latitudes where synoptic events leading to destratification are common, *e.g.,* cold front passages over the Argentinian shelf during winter).

Several other ways that submesoscale can influence coastal dynamics have been uncovered recently. Long-lived subsurface mesoscale anticyclones prevalent in the California Current System at a depth range of 100 m to 500 m seem to be generated through episodes of intense submesoscale instability in the California Undercurrent (Molemaker et al., 2015), with major implications for the dynamics and thermohaline variability of the Monterey Bay area. Submesoscale coastal eddies modify the fate of river runoffs in the Baltic Sea (Gurova and Chubarenko, 2012) or nutrient transport in the Santa Barbara channel (Bassin et al., 2005).

The seasonal modulation of submesoscale activity by atmospheric conditions analysed in Capet et al. (2008a) is not restricted to shelves and the submesoscale driven variability of the open ocean is currently a subject of great interest (Sasaki et al., 2014; Mensa et al., 2013).

2.4 Theoretical models of submesoscale turbulence

Classical QG driven by interior potential vorticity is unsuited to represent frontal intensification but QG frameworks accounting for the presence of surface and/or bottom density contrasts capture important characteristics of real ocean submesoscale activity.

There are now ample evidences, observational and numerical, that the submesoscale range is populated by more than passive tracer filamentary structures as in

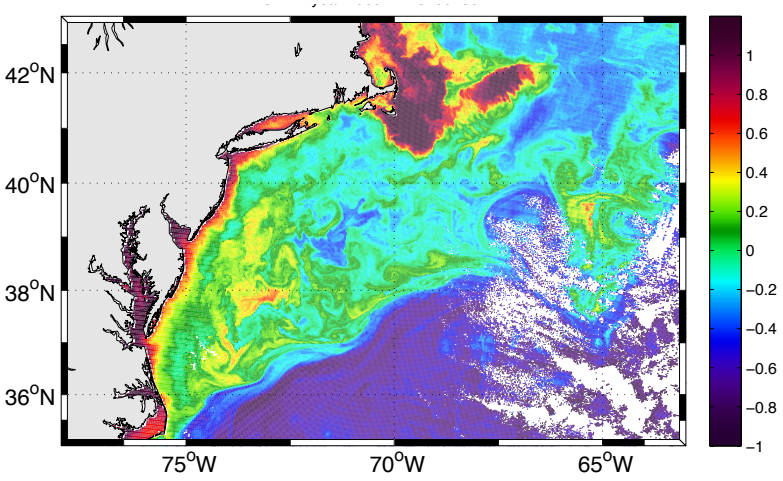

Figure 2.7: Aqua MODIS Chlorophyl-a image of the Mid-Atlantic Bight on 24 April 2009. The field is stirred by turbulent structures whose scale is in the submesoscale range.

quasigeostrophic turbulence, *i.e.,* the ocean rarely resembles Fig. 2.5a). In classical quasigeostrophy there is little energy on scales below the first baroclinic deformation radius R_1, and the tracer variance at these scales is controlled almost entirely by mesoscale eddy stirring (*i.e.,* nonlocally in wavenumber). Near-surface tracer fields exhibit filamentary structures that are elongated by the mesoscale straining field. As discussed in Blumen (1978) and alluded to in Charney (1971) (see also Lapeyre and Klein 2006 and **Roullet et al. 2012** for more modern presentations) this is because because a key assumption in **classical QG** suppresses the so-called "**surface mode**" by assuming that the upper and lower boundary conditions for the streamfunction ψ are simply $\partial_z\psi$ constant at $z = 0$ and $z = -H$ (see Fig. 2.8. In the general case upper and lower boundary conditions are non trivial[3] which is equivalent to considering non-uniform surface and bottom density, ρ_s and ρ_b (because $\partial_z\psi$ is proportional to density owing to the hydrostatic balance).

More generally, a **complete QG** ocean is defined by the evolution of three PV type scalars, interior, surface and bottom:

$$q = \nabla^2\psi + \partial_z\left(\frac{f^2}{N^2}\partial_z\psi\right) \tag{2.1}$$

$$\rho_{s,b} = -\frac{f\rho_0}{g}\,\partial_z\psi \qquad \text{at } z = 0, -H \tag{2.2}$$

[3]In the case where lateral sides are present boundary conditions are also needed there (Roullet et al., 2012) but we ignore this aspect for simplicity.

where q is the QG interior potential vorticity, $\rho_{s,b}$ are respectively surface (s subscript) and bottom (b subscript) densities, and $N^2(z) = d\bar{b}(z)/dz$ is the squared buoyancy frequency of the mean stratification $\bar{b}(z)$. The presence of $\partial_z\psi$ in the stretching term (second rhs term in 2.1) allows a reformulation of the conditions (2.2). They are equivalent to having surface and bottom potential vorticity sheets (Bretherton, 1966)

$$q_s = \frac{f^2}{N^2}\partial_z\psi|_{z=0}\,\delta_0 \tag{2.3}$$

$$q_b = -\frac{f^2}{N^2}\partial_z\psi|_{z=-H}\,\delta_{-H} \tag{2.4}$$

where the Dirac delta function δ expresses the confinement of these extra potential vorticities at the boundaries.

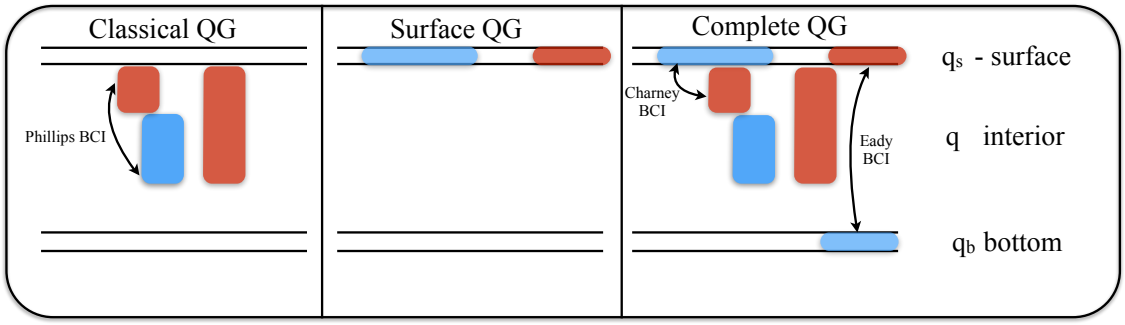

Figure 2.8: Schematic representation of the **complete quasi-geostrophic model** *(right) and two of well-known simplifications. Colored cylinders represent potential vorticity patches. QG is a framework in which the knowledge of potential vorticity distribution suffices to determine the system state. In particular PV can be diagnostically inverted and provide the pressure field (i.e., the geostrophic flow streamfunction ψ) from which velocities can be deduced. Traditionally QG has been used in conditions where surface and bottom potential vorticity are neglected, i.e., upper and lower boundary conditions are trivial and only interior potential vorticity exists. In this manuscript this QG framework is refered to as* **classical QG**. *Another important simplification consists in neglecting interior and bottom potential vorticity, in which case the flow is entirely driven by surface potential vorticity. The forms of baroclinic instability (BCI) that can exist in the different models (no BCI is possible in SQG). Barotropic instability is possible in all three QG models variants.*

The existence of surface gradients in ρ_s being associated with PV it is dynamically important and introduces a surface mode. This mode significantly modifies QG flows and in particular energizes them near the surface. A significant part of my research

has been dedicated to understanding the characteritics of QG turbulence in presence of inhomogeneous ρ_s and its relevance to the real ocean. Because of its simplicity the case where interior and bottom potential vorticity are zero (or constant) is particularly useful. It is generally refered to as "**surface QG**" (hereafter SQG). By definition, SQG is characterized by zero interior and bottom PV: $q \equiv 0$ and $\rho_b \equiv 0$.

In this case the flow dynamics is dominated by (quasi-geostrophic) frontogenesis of the active surface tracer and offers in many respects a better suited representation of upper ocean submesoscale turbulence than traditional interior QG ($\rho_s \equiv 0$, $\rho_b \equiv 0$). In particular, this regime possesses near-surface EKE and potential energy distributions that are consistent with those found in many regions of the real ocean (Kim et al., 2011; Sasaki and Klein, 2012; Xu and Fu, 2012) with wavenumber spectral distributions for these two quantities that roll-off as $\mathrm{k}^{-5/3}$.

One particularly attractive aspect of SQG is that equation (2.1) with $q \equiv 0$ implies that solutions decaying away from the surface can be found in the form of Fourier modes in the horizontal with:

$$\hat{\psi}(m,n,z) = -\frac{g}{N\rho_0}\frac{\hat{\rho}_s(m,n)}{k} exp\left(k\frac{N}{f}z\right) \tag{2.5}$$

where $(\hat{\cdot})$ is the horizontal spectral transform, m, n are the zonal and meridional wavenumbers, and $\mathrm{k} = (m^2+n^2)^{1/2}$. In short, surface density drives the entire flow evolution in SQG. As a diagnostic tool SQG thus offers the interesting possibility to reconstruct all 3D dynamical fields (*i.e.,* also the interior flow) solely based on the knowledge of fine-scale surface density or free-surface fields and large-scale interior stratification.

Favorable but limited assessments of the methodology were carried out in Lapeyre and Klein (2006), LaCasce and Mahadevan (2006), Isern-Fontanet et al. (2006), **Klein et al. (2008a)** (see Fig. 2.9) and Lapeyre (2009a). The latter study demonstrates that eddy resolving model surface velocities in many ocean sectors in the north atlantic "project" mainly on the SQG mode (as opposed to the first baroclinic mode), a conclusion that is consistent with the work based on observations by (Isern-Fontanet et al., 2006). Note that one of the most interesting applications would be on the reconstruction of interior vertical velocities (hence a possibility to infer vertical fluxes of properties provided some high resolution knowledge of their distribution). A promising proof of concept is presented in Klein et al. (2009) in which vertical velocities in a PE numerical solution and their SQG reconstructions are shown to

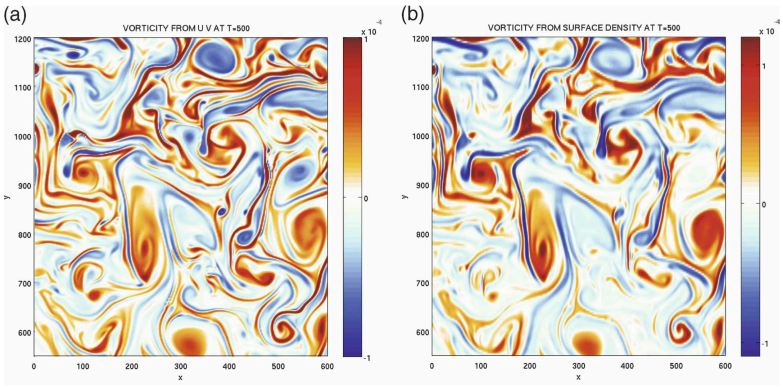

Figure 2.9: Zoom of the surface relative vorticity field (a) deduced from u and v and (b) reconstructed from the surface density using eq (2.5); units in the x and y directions in are km and vorticity units are s^{-1}. Reproduced from **Klein et al. (2008a)**.

be in good agreement. Note though that the simulation used in this study have a tight coupling between surface and interior dynamics (because it is subjected to Charney baroclinic instability, see below) and may be particularly favorable. The only observational test of that method for vertical velocities is by LaCasce and Mahadevan (2006). It consists in the comparison of vertical velocities inferred from the omega equation (see Sec. 2.5) and from SQG framework. Important differences are found that are difficult to attribute, owing to important simplifications and sources of errors in both methods.

There are several reasons why SQG reconstruction may fail. Among them is the surface-interior decoupling due to the mixing in the surface boundary layer **(Ponte et al., 2013)**. A perhaps more worrisome limitation that has received limited attention so far concerns the existence of fine-scale interior PV structures in the ocean. As stated above SQG requires $q \equiv 0$ to be formally valid. This assumption may be relaxed in practice and one may only need to have q vary slowly enough to be considered constant on submeso/mesoscales so that on such scales the dynamics is driven by constrasts in surface PV q_s. Alternatively, if interior and surface PV are well correlated (or, more likely, anticorrelated) the effect of interior PV can be accounted for by adjusting the Brunt-Vaisala frequency, following the so-called effective SQG method (Lapeyre and Klein, 2006) (see also (Lapeyre, 2009b)). An important example where this approach is unlikely to work concerns frontal situations where atmospheric winds blow downfront and intense subduction episodes

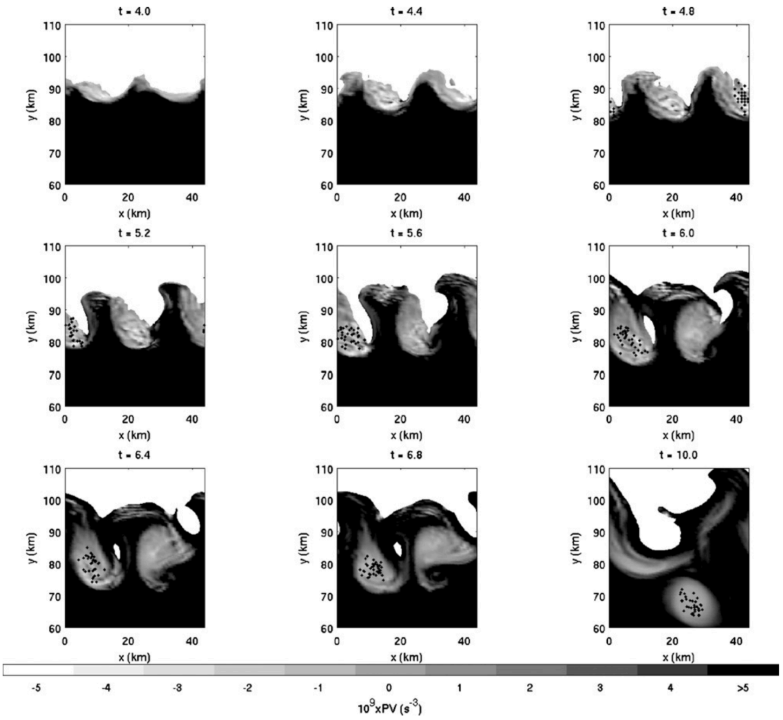

Figure 2.10: Potential vorticity on the 28.335 kg m^{-3} isopycnal surface at different times (in units of inertial periods, indicated at the top of each panel) during a simulation of subduction forced by a downfront wind. Also plotted in black dots are the locations of Lagrangian floats released in the low-PV plume. Light shades indicate low PV values. Subduction leads to the formation of fine-scale interior PV structures. Reproduced from Thomas (2008).

produce fine-scale interior PV structures (Thomas, 2005; Thomas and Taylor, 2010; Thomas et al., 2010) (see Fig. 2.10 and also Sec. 2.5.3). How frequent these situations are is unclear but mounting evidence suggests that they are not uncommon and may have a disproportionate importance in terms of vertical fluxes, *e.g.,* in mode water formation regions (Thomas and Joyce, 2010). This sets stringent limitations to the SQG relevance and realism.

The SQG model as a prognostic framework is peculiar in that it has no baroclinic instability mechanism. Indeed PV is non zero only at the surface boundary and can therefore not satisfy the Charney Stern necessary condition for baroclinic instability (Charney and Stern, 1962) that the lateral gradient of QG potential vorticity changes sign on the vertical. Thus it cannot generate intrinsic mesoscale variability at horizontal scales commensurate with a first deformation radius. On the other hand, more complex situations with $q \neq 0$ or $q_b \neq 0$ permit the interaction of sur-

face potential vorticity (*i.e.,* the surface mode) with interior or bottom potential vorticity. In these conditions the flow can be subjected to, respectively, Charney ($q \neq 0$, $\rho_s \neq 0$) or Eady ($\rho_s \neq 0$, $\rho_b \neq 0$) baroclinic instability. This is, again, best understood with the help of the Charney-Stern necessary condition for baroclinic instability. In the general case described by eqs (2.1-2.2) the PV sign change can occur in the ocean interior if $\partial_y q$ changes sign (Phillips baroclinic instability), or involve boundary PV q_s and/or q_b. The Charney (respectively Eady) baroclinic instability corresponds to the case where the change of sign is due to the fact that surface and interior (respectively bottom) PV gradients are of opposite sign (*e.g.,* see (Tulloch et al., 2011)). Note that the flow considered in **Klein et al. (2008b)** satisfies the condition for Charney instability which substantially contributes to the intensification of its upper ocean submesoscale activiy (including vertical velocities) and presumably reinforces the coupling between surface and interior dynamics.

My research has been concerned with the turbulent behavior and characteristics of Eady flows (in QG and also in non-Boussinesq models, **Molemaker et al., 2010**) as well as Charney flows (in QG and primitive equations **Roullet et al., 2012**, **Capet et al., 2015a**). Overall, and in agreement with conclusions previously reached for the simplest SQG model, these studies have confirmed the importance of the surface mode as a source of frontal intensification. The topic on which they have been most useful is the energetic functioning and role of the submesoscale turbulent regime which are presented below. Although the relevance of these turbulent regimes should be considered cautiously they have been and will presumably remain useful to explore submesoscale properties and guide the research in the area.

2.5 Submesoscale vertical velocities and fluxes of properties

Significant efforts have been put on trying to gain insight into vertical velocities and fluxes in the ocean. We review the different approaches adopted over the past $\sim$ 20 years and discuss their limitations. Estimations of vertical fluxes in the ocean remain difficult although much progress has been made in the understanding of the key processes.

2.5.1 An enduring observational challenge

A key issue in relation with meso and submesoscale features is the extent to which they contribute to vertical fluxes of ocean properties, in particular biogeochemical. Since the 1990's several important field programs have attempted to map and quantify the vertical velocities that accompany a mesoscale turbulent field, essentially on the edge of the eddies, *i.e.,* at submesoscale (Leach, 1987; Pollard and Regier, 1992; Rudnick, 1996; Allen and Smeed, 1996; Shearman et al., 1999; Garabato et al., 2001; Allen et al., 2001; Martin and Richards, 2001; Pascual et al., 2004; Kouketsu et al., 2007; Legal et al., 2007; Gil and Gomis, 2008; Thomas et al., 2010; Thomas and Joyce, 2010; Pallàs-Sanz et al., 2010b; Benítez-Barrios et al., 2011; Nagai et al., 2012). The approach is based on frontogenesis theories (QG but also more elaborate forms, see below) and the omega equation (Hoskins, 1982). The underlying principles involve two types of arguments:

- ✓ a turbulent field stirring an heterogeneous surface buoyancy field produces regions of gradient intensification. Specifically, frontogenesis is promoted in the confluence and shear situations, *i.e.,* particular configurations of the tracer and eddy field that are frequently encountered in mesoscale turbulent conditions (see Fig. 2.11).

- ✓ If frontogenetic straining is performed by eddy structures at meso/submesoscale it disrupts the dominant thermal wind balance because it tends to enhance the buoyancy gradient intensity while reducing the vertical velocity shear (Hoskins et al., 1978; MacVean and Woods, 1980; Bleck et al., 1988; Thomas et al., 2008). Thermal wind balance disruption leads to the development of an ageostrophic secondary circulation (ASC) that reduces imbalance by restoring shear and slumping of the isopycnals. In the ocean interior this process is very efficient at preventing frontal intensification. In the upper ocean (or near the bottom) the constraint $w \approx 0$ limits the efficiency of ageostrophic circulations. Consequently, frontal intensification is difficult to halt. It is even reinforced by the quasi-horizontal ageostrophic velocities close to the surface; and mixing processes (of momentum and tracer) are necessary to prevent singularities from developing. A variant of this process applicable to cold filaments has been proposed by McWilliams et al. (2009a).

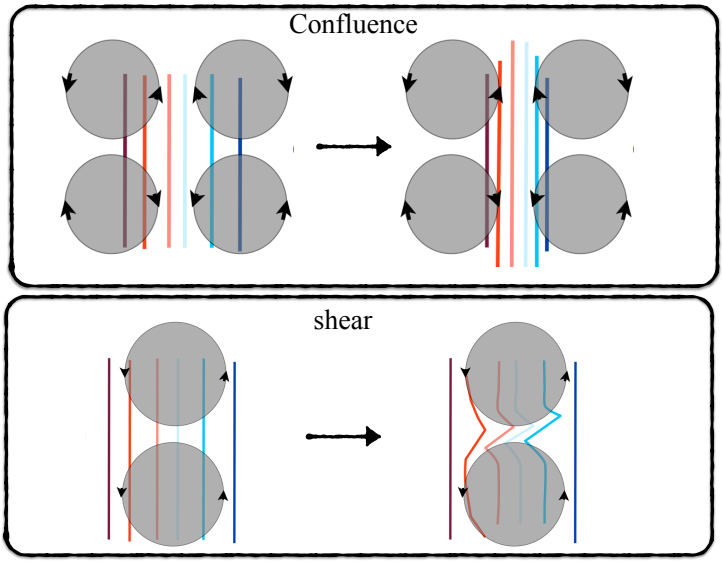

Figure 2.11: Schematic representation of the two canonical frontogenetic situations (top:confluence; bottom: shear). In both situations a temperature gradient is present (warmer on the left) that undergoes straining by an eddy field (gray shading with circulation represented by black arrows). As time increases (from left to right) the temperature gradient intensifies and forms a frontal zone.

More or less elaborate versions of the omega equation are available (Pinot et al., 1996; Shearman et al., 2000; Viúdez and Dritschel, 2004; Sanz and Viúdez, 2005) and frontogenetic processes other than mesoscale straining can be incorporated. Indeed, any process acting on large enough scales to disrupt thermal wind balance in geophysical flows provokes a response involving vertical velocities (*e.g.,* Nagai et al., 2006; **Ponte et al., 2013**). These velocities can a priori be estimated using a generalized form of the omega equation (Giordani et al., 2006; Thomas and Taylor, 2010). Vertical velocities induced in the context of thermal wind balance disruption/restoration are widely believed to play an important role in the vertical exchanges of biogeochemical tracers, *e.g.,* across the euphotic layer (subduction of organic material, uplifting of nutrients).

There are numerous methodological obstacles when attempting to observationally estimate ageotrophic secondary circulations and their effects on tracer vertical fluxes. Vertical velocity is highly variable in space and time, particularly in the strain regions where frontogenesis/frontolysis is active and w is most intense. Therefore, lack of synopticity, limited spatial resolution, and noise level in the measurements of

horizontal velocities and density (needed to solve the ω equation) introduce significant uncertainty in the w estimate (Allen et al., 2001; Rixen et al., 2001; Rixen and Beckers, 2002; Rixen et al., 2003; Gomis and Pedder, 2005; Pidcock et al., 2013). Other limitations include the finite-size of the observational domain (or alternatively the imperfect conditions imposed at the domain boundaries when solving the equations, Pascual et al., 2004) and the simplications inherent to the approach (Pinot et al., 1996). Refining the latter puts a heavier burden on data acquisition, often beyond practical feasibility (Giordani et al., 2006; Thomas and Taylor, 2010).

Overall, vertical velocities obtained from solving the omega equation tend to be weak (LaCasce and Mahadevan, 2006; Koszalka et al., 2009), presumably as a consequence of insufficient resolution. They are sometimes even grossly inconsistent with tracer distribution as in Ruiz et al. (2009) where vertical velocities from the omega equation barely reach $\pm$ 1 m d^{-1} whereas chlorophyl subduction suggest vertical velocities over one order of magnitude larger. Thomas et al. (2013) and Legal et al. (2007) are counterexamples. The former obtains vertical velocities of 100-200 m d^{-1} during an intense episode of mode water formation in the vicinity of the Gulf stream axis (see also Thomas and Joyce, 2010). The latter has vertical velocities that are only 10-20 m d^{-1} but this is for a situation of moderate mesoscale straining in which primitive equation numerical simulations (Paci et al., 2005; Lévy et al., 2005) develop vertical velocities of magnitude 5 to 10 times smaller, perhaps as a consequence of insufficient model resolution $\Delta x = 5$ km.

Another issue is that net vertical exchanges are frequently a small residual resulting from successive upward and downward water mass displacements of large amplitude (Lindstrom and Pandolph Watts, 1994; Allen and Smeed, 1996; Martin and Richards, 2001), *i.e.,* Lagrangian observations would be better suited. Additional complexity may arise if net vertical exchanges are the consequence of minute irreversible processes taking place as water parcels are displaced up and down following quasi-isopycnal trajectories. At last, robust estimates of the correlations between vertical velocities and tracer distribution at the relevant scales (meso- and submesoscale) are presumably difficult to obtain, given the widely different nature of the processes involved in their respective evolutions. For all these reasons and because of constant increase in computational power numerical modeling has become the approach of choice to quantify vertical turbulent fluxes in the ocean. In the remainder of this section we review the recent work done on vertical velocities. In doing so, we

discuss how our appreciation of the role of submesoscale has progressively evolved over the last 10-15 years.

2.5.2 Sensitivity of vertical velocities to subsurface stratification

In a previous section (Sec. 2.2) we have described how and why vertical velocity magnitudes may increase ten-fold or more when kilometer scale processes are properly resolved **(Capet et al., 2008e)** (see also Levy et al., 2001; Lévy et al., 2010; Rosso et al., 2014; Zhong and Bracco, 2013). This increase is a consequence of better resolved frontogenetic processes and of the representation of short-scale baroclinic instabilities near the ocean surface. The latter performs sustained APE to EKE conversion and strongly depends on atmospheric APE input into the upper ocean to do so. In many places of the ocean atmospheric APE inputs are well confined within a relatively shallow mixed layer and so are intense frontal ageostrophic circulations[4]. The submesoscale may therefore not systematically contribute in important ways to BGC-useful vertical exchanges. An illustration of that is provided by Fig. 2.12 taken from **Capet et al. (2008f)**. A PV section across an idealized upwelling transition zone shows the thermohaline structure of the upper 600 m including the surface mixed layer with low PV. In particular, the thermocline doming associated with a mesoscale eddy structure is noticeable around x=300 km. Submesoscale frontal circulations that trigger exchanges between the mixed layer and the subsurface are easily identifiable through their signature in PV, *i.e.,* $\sim$ 5 km wide intertwined low and high PV fingers. These fingers are the manifestation of PV fluxes between the upper thermocline and the mixed layer. The largest excursions occurs around y = 200 km on the southern edge of the mesoscale structure. Large excursions are also found on the opposite edge. In the former region a mixture of high and low PV (in yellow green) extends downward at most 25 m below the average mixed layer base. Overall only a small fraction of the upper thermocline is implicated in the PV exchanges with the surface and these exchanges take place in specific areas. Submesoscale frontal activity discernable in SST within the eddy or around the northern mesoscale feature (y = 600 km) has for example a very limited effect. This descrip-

[4]This view underlies for example the form of the parameterization proposed by Fox-Kemper et al. (2008),Fox-Kemper et al. (2011) to represent the effect of mixed layer eddies. Indeed the parameterization assumes zero exchanges across the mixed layer base

tion is for summer mean climatological forcings and may differ for other seasons or during upwelling events. In the California current system Barth et al. (2002) observe chlorophyl concentrations at depths between 150 and 250 m that they attribute to mesoscale driven subduction Numerical models tend to confirm that sufficiently close to shore, where fronts are most intense, the biogeochemical functioning of upwelling systems is influenced by subduction (Gruber et al., 2011; Lathuilière et al., 2008).

On the other hand, submesoscale processes may be of limited importance in the biogeochemical functioning of typical subtropical regions. In Ascani et al. (2013) multi-year Lagrangian observations (nitrate, temperature, conductivity and dissoved oxygen) in the northern subtropical Pacific (vicinity of ALOHA station) are analyzed. The main focus is on the origin of nitrate high frequency variability in the upper 250 m of the ocean. In the subtropical Pacific the mixed layer is not deep enough to reach the nutricline except in winter/early spring in some instances. Therefore the intense submesoscale frontal activity associated with mixed layer eddies does not significantly contribute to episodic nutrient injection and primary production. On the other hand, part of the submesoscale frontal activity is due to mesoscale stirring and inherits its typical depth scale from that of the mesoscale, hence it is able to reach down to the nutricline.

These observations substantiate the description of Fig. 2.12 but they are in sharp contrast with a number of pioneer modeling studies suggesting significant modification of the BGC functioning when submesoscale structures are represented. Ascani et al. (2013) argue that the reason behind the differences is in the position of the nutricline relative to the depth range of surface density fronts; all numerical studies showing the importance of submesoscale processes have a nutricline that intersects their upper ocean density front (Levy et al., 2001; Nurser and Zhang, 2000; Spall and Richards, 2000).

There is no doubt that the nutricline position is a crucial aspect of such idealized studies. Having the nutricline cross outcropping isopycnals is essential in permitting frontal circulations to flux nitrate within the surface layer which can then be done adiabatically, along isopycnals. We see at least one additional reason why the conclusions drawn from this series of idealized studies should be considered cautiously. Indeed their density profiles is generally representative of mid- or high-latitude destratified (wintertime) conditions with small deformation radii and plenty of surface available potential energy to fuel short-scale baroclinic instability modes. This is

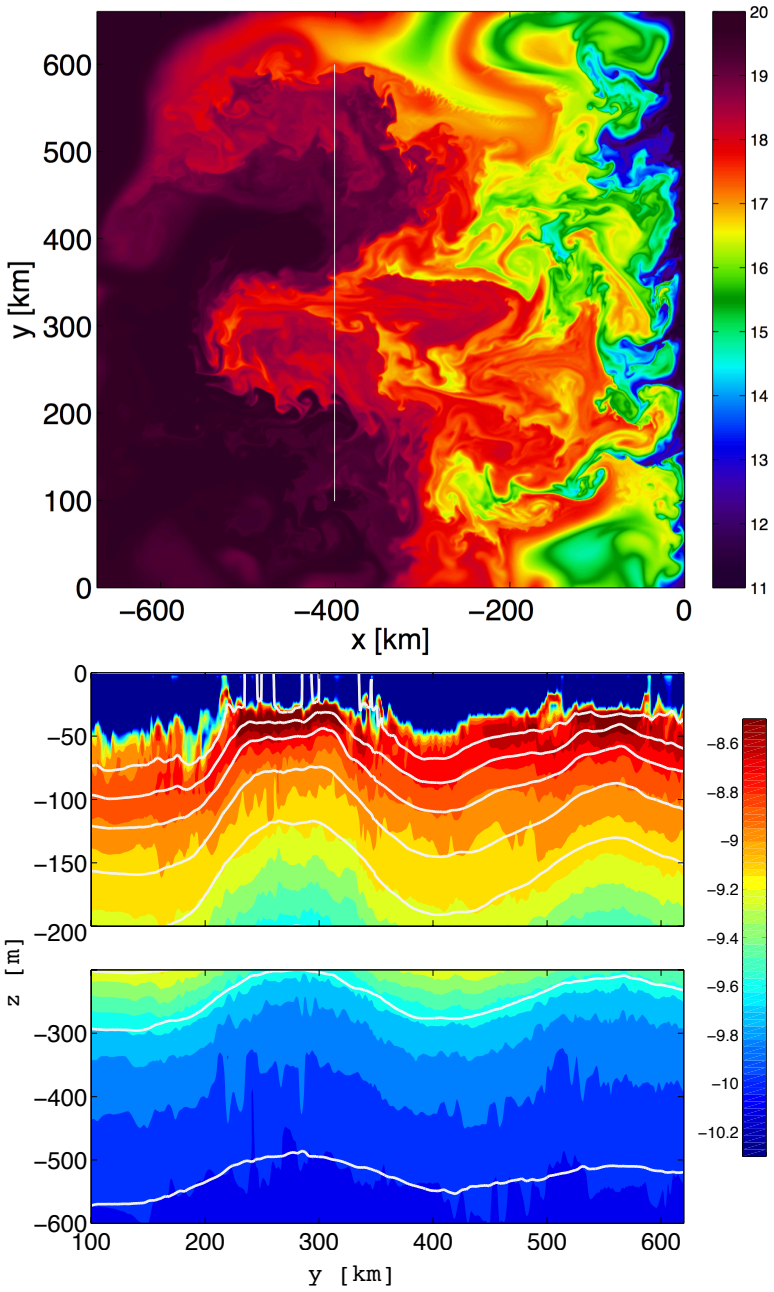

Figure 2.12: Top:Instantaneous SST in the Δx= 750 m idealized California current simulation of Capet et al. (2008f). Bottom: Cross section of Ertel potential vorticity (m^{-1} s^{-1}) in logarithmic scale, with superimposed isopycnals (white lines) along the meridional section represented in top panel with a white segment. Note the different vertical scales for the [-200 0] and [-600 -200] m depth ranges.

particularly clear for Levy et al. (2001) and Spall and Richards (2000). It is intuitively evident that weakly stratified environments are more favorable to long range vertical exchanges.

To illustrate this I now present preliminary results on the sensitivity of subduction to stratification. A surface passive tracer is used to quantify subduction during the spindown of two idealized Antarctic circumpolar currents similar the ones considered in **Klein et al. (2008a)**, **Ponte et al. (2013)** and **Capet et al. (2015a)**. The two solutions, S1 and S2, differ only through their vertical stratification but mean meridional density gradients are identical in both. The solution with weak stratification (S1) is subjected to a Charney type baroclinic instability (see Sec. 2.4) which contributes to intensifying submesoscale turbulence. The presence of that instability intensifies submesoscale activity and places us in a potentially peculiar situation. On the other hand, it does not seem unreasonable that more instability modes arise in weakly stratified environments (Stone, 1966; Haine and Marshall, 1998; Thomas et al., 2013; Qiu et al., 2014). A $\approx$ 80m mixed layer is created in the simulations through the application of a zero net heat flux composed of penetrant short-wave radiation and opposite outgoing longwave/turbulent heat flux. At t=0 the tracer is injected in the mixed layer while the heat forcing and zonal restorings are switched off. Overall, we see this experiment as an idealization of late-winter ML restratification episodes. S1 corresponds to a situation where the subsurface stratification has been significantly eroded, as in mode water formation regions whereas S2 is representative of a more classical subtropical situation where significant stratification has persisted below the winter mixed layer.

Tracer distributions in S1 and S2 are represented in Fig. 2.13 after 30 of spindown for $\Delta x = 1$ km and $\Delta x = 8$ km. Tracer distributions in S1 are also shown when the lateral diffusion operator for tracer is rotated to limit its diapycnal effect (Lemarié et al., 2012), which leads to more intense fronts, more intense APE to EKE conversion rates but also subduction processes that are less susceptible to diapycnal mixing.

Tracer subduction is significantly different in S1 and S2. Maximum depth for tracer values at 1% (respectively 1 ‰) of the surface concentration is around 300 m (resp. 400 m) in S1 *i.e.,* nearly twice the depth obtained for S2 (170 m for 1%, 220 m for 1 ‰). In S1 simulated with $\Delta x = 8$ km subduction depth is significantly reduced, roughly by a factor 2 so that subduction in S1 at 8 km resolution resem-

bles that for S2 at $\Delta x = 1$ km. Note that differences between S1 and S2 are more limited at low resolution. In short, enhanced subduction in S1 is driven by frontal intensification and fine-scale dynamics. It is therefore very sensitive to horizontal resolution and/or subgrid scale parameterization of mixing and dissipation. This latter point is corroborated by the analysis of the simulation where the tracer advection operator is rotated to attempt to operate along isopycnal directions. Using this operator produces a noticeable increase in average tracer distribution although maximal subduction depth are not strongly affected.

Overall, we interpret these results as an indication that eddy resolving/permitting models strongly underestimate the subduction sensitivity to stratification and are particularly unsuited to representing high latitude environments. This also provides a confirmation that subsurface stratification is a critical aspect of vertical exchanges. The numerical sensitivity to the choice made for the diffusion operator highlights the need for Large Eddy Simulation standards against which such submesoscale permitting solutions can be confronted.

2.5.3 The role of destabilizing forcings and symmetric instability

The development of a research line considering frontal environments under detabilizing atmospheric conditions seems to implicitely recognize the difficulty to flux ocean properties across stratifications. Most subduction regions share two important characteristics, i) the presence of major density contrasts and ii) the influence of destabilizing atmospheric forcings which modify the frontal environment and ageostrophic circulations (Yoshikawa et al., 2012). Although not systematic important ties can exist between i) and ii). This is perhaps most evident when forming the upper ocean PV balance. In a rotating, stratified fluid the Ertel potential vorticity is defined by

$$q_e \;=\; -\frac{1}{\rho_o}\,(f\hat{\mathbf{z}} + \nabla\times\mathbf{u})\cdot\nabla\rho\,. \tag{2.6}$$

and its governing equation is

$$\frac{Dq_e}{Dt} \;=\; -\,\nabla\cdot\mathbf{J} \tag{2.7}$$

where $\mathbf{J}$ is the non-conservative PV flux (Marshall et al., 2001)

$$\mathbf{J} = \frac{1}{\rho_o}N_\rho\,(f\hat{\mathbf{z}} + \nabla_h\times\mathbf{u}) \;-\; \frac{1}{\rho_o}\nabla\rho\times\mathbf{N_u}\,. \tag{2.8}$$

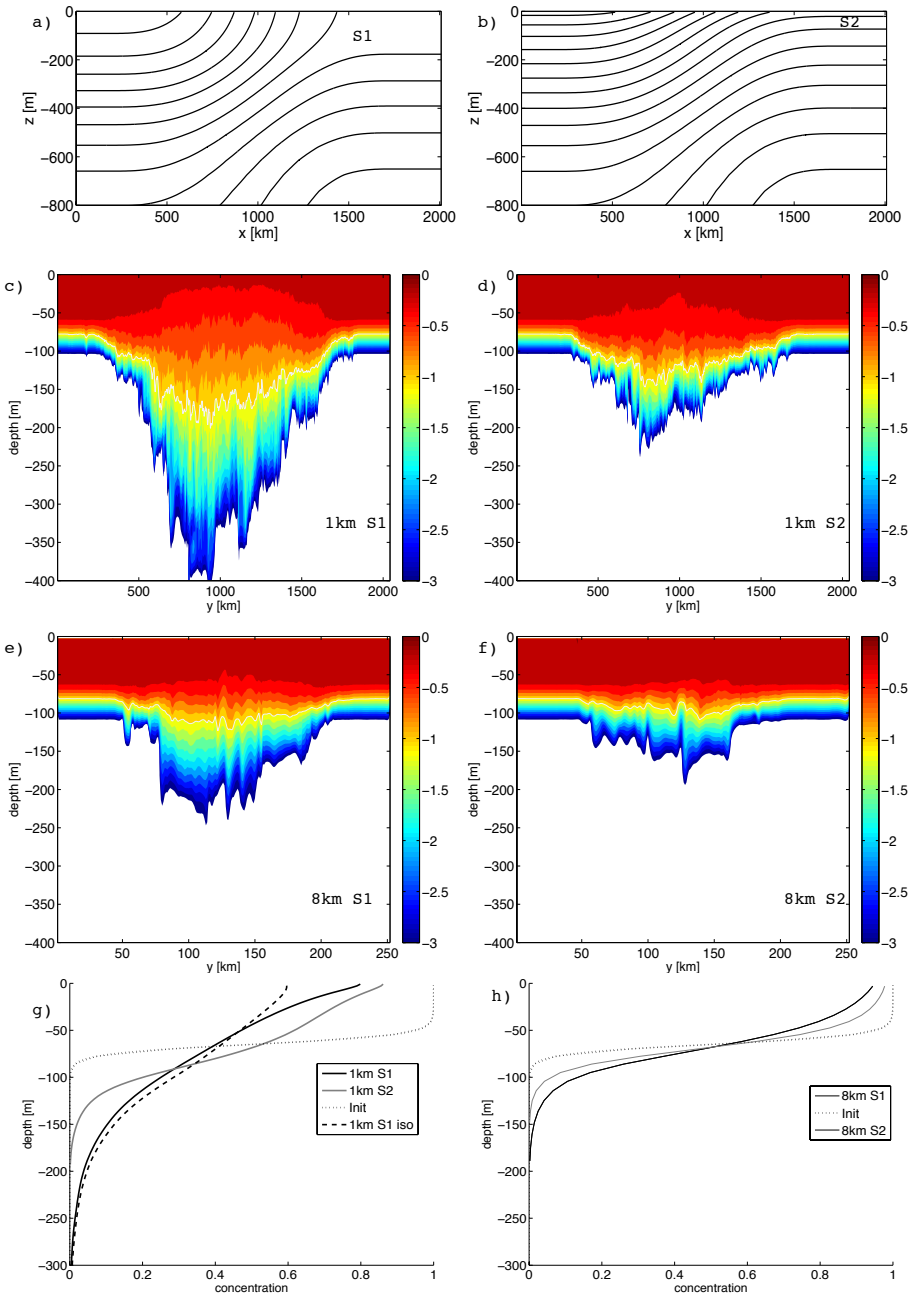

Figure 2.13: a-f): y-z section of initial density (a,b; contour interval is 0.25 kg m^{-3}) and tracer concentration (c-f, log scale) after 30 days of spindown for two baroclinically unstable flows S1 (left, weak stratification) and S2 (right, moderate stratification) with the same mean meridional density gradient. g-h): Horizontally averaged tracer profiles after 30 days at 1km (left) and 8 km resolution for the different experiments. The initial distribution is also shown. In g) tracer distribution is also shown for an experiment using a rotated lateral diffusion operator that minimizes diapycnal mixing (Lemarié et al., 2012) (S1 iso).

All vectors are fully three-dimensional in (2.8), N_ρ is the diabatic term in the potential-density equation, and $\mathbf{N_u}$ is the non-conservative force (including wind-induced friction).

PV is in general dominated by stratification effects and low PV is a reliable marker of subducted water. Either term in (2.8) can be a PV sink and generate low PV water masses by exchanges with the atmosphere. In the surface boundary layer where $\mathbf{N_u}$ is dominated by wind-induced friction the second rhs term scales as the quantity (Thomas, 2005):

$$Q_w = -\frac{1}{\rho_0 f} M_e \cdot \nabla_h \rho \tag{2.9}$$

where M_e is the Ekman transport in the boundary layer. This term represents an Ekman density/buoyancy flux. It is destabilizing wherever winds blow over an ocean front in such a way that Ekman transport forces dense fluid to override lighter fluid. This so-called downfront wind situation necessarily leads to some form of convective process. L. Thomas and coauthors have provided ample numerical and observational evidences of the importance of the PV destruction taking place in downfront wind conditions (Thomas, 2008; Thomas and Joyce, 2010; Thomas et al., 2010; Yoshikawa et al., 2012). In upwelling systems this process is present but its overall effect seems modest in average conditions **(Capet et al., 2008f)**. In the subtropics it can be responsible for vertical intrusions and fluxes between the mixed layer and the seasonal pycnocline (Hosegood et al., 2013). In other places, Ekman buoyancy fluxes equivalent to -10 000 W m^{-2} can be found, which has major consequences in terms of water mass transformation and subduction. By nature, convection driven by destabilizing EBF occurs in an environment combining thermal wind shear and low stratification, hence low Richardson numbers which tends to favor slantwise convection, a.k.a, symmetric instability.

Symmetric instability is a modified form of convection that takes place along slantwise pathways because a frontal environment and thermal wind shear constrain the unstable motions (Stone, 1966; Haine and Marshall, 1998). Just like convection and baroclinic instability symmetric instability grows from the release of APE. It is refered to as symmetric because it is invariant in the along-front direction in its canonical form. The across-front length scale of the unstable flow is generally smaller than 1 km, *i.e.,* at the lower end of the submesoscale range.

Although much remains to be learned about symmetric instability, destabilized frontal environments and their importance for the ocean functioning, significant

progress has been made thanks to Taylor and Ferrari (2009),Taylor and Ferrari (2010), Taylor and Ferrari (2011), Thomas and Joyce (2010), and Thomas et al. (2013). The complementary roles of symmetric and fine-scale baroclinic instabilities are well illustrated by the simulations of frontal regions under destabilizing heat forcings of Taylor and Ferrari (2011): restratification occurs very rapidly (less than a day) due to symmetric instability whereas baroclinic instability achieves a much stronger restratification but on much longer times (several days). Both modeling and observational studies indicate that symmetric instability is able to produce boundary layers in which mixing is efficiently counteracted and partial restratification is achieved despite destabilizing atmospheric conditions. Then, when symmetric instability is present, vertical mixing takes place in a relatively organised manner along slantwise pathways. This increase the residence time of planktons in the sunlit region which increases primary production. Interestingly, these new developments shift the attention on the role of submesoscale in alleviating light limitations (as opposed to nutrient limitation) which may be particularly appropriate for weakly stratified subpolar environments (Mahadevan et al., 2012). Nevertheless, near the axis of intense frontal jets, turbulent mixing may be responsible for large subsurface vertical fluxes (Aoki and Akitomo, 2007), including nutrient fluxes into the euphotic layer (Garabato et al., 2002; Kaneko et al., 2013).

2.6 Small-scale dissipation through submesoscale turbulence

The possibility that submesoscale allows mesoscale energy to cascade toward smaller scales where it dissipates and, hence, substantially contributes to the energetic equilibration of mesoscale flows is reviewed. Significant progress has been made over the past 10 years. Despite contradicting results this route to dissipation is unlikely to be significant in my opinion.

The way mesoscale KE and APE are dissipated is not very well constrained (Wunsch and Ferrari, 2004). It is widely believed that a large fraction of that dissipation occurs through barotropization and bottom friction (Salmon, 1980). In the early 2000's several studies consider the possibility that balanced flows be inherently capable of locally developing fine scale motions that would significantly contribute

to the dissipation of the large reservoir energy stored at the mesoscale. Among these studies two main research lines can be distinguished, one focusing on the spontaneous emission of inertia-gravity waves (Vanneste, 2013; Plougonven and Snyder, 2007); the other focusing on the role of local flow intensifications leading to the simultaneous violation of balance requirements and development of unbalanced flow instabilities (Molemaker et al., 2005; Müller et al., 2005). The latter line has been an important initial motivation for my submesoscale investigations. In particular a key question to be addressed with the idealized California current solutions (Sec. 2.2) concerned the role of submesoscale in the overall energetics of the system, including in the ocean interior. Although research is still ongoing on this topic an assessment of 10 years of investigations is instructive. Essentially we see two groups of numerical studies that partly contradict each other on the overall significance of the forward route to dissipation through submesoscale.

Before discussing these studies we introduce the underlying methodology. It essentially relies on Fourier manipulations of the dynamical equations that are decomposed with respect to horizontal wavenumber. We start with the spectral density of a 1D field f:

$$\mathcal{S}_f(k) = \hat{f}^* \cdot \hat{f} \tag{2.10}$$

where $\hat{.}$ denotes the Fourier transform and * the complex conjugate. $\mathcal{S}_f$ describes how the variance of f is distributed over the wavenumber components into which f can be decomposed. Likewise, the co-spectrum of two 1D fields f and g defined over a similar domain writes:

$$\mathcal{S}_{f,g}(k) = \mathcal{R}e\left(\hat{f}^* \cdot \hat{g}\right) \tag{2.11}$$

and describes how the co-variance of the two functions is distributed over the wavenumber components into which they can be decomposed ($\mathcal{R}e$ selects the real part of a complex).

A spectral KE balance can be constructed by taking the Fourier transform of the PE momentum equation, multiplying it by $\widehat{\mathbf{u}}_h^*$ and taking the real part of the equation. This yields

$$\frac{1}{2}\mathcal{R}e\left[\partial_t\left(\widehat{\mathbf{u}}_h^*\widehat{\mathbf{u}}_h\right)\right] = \mathcal{R}e\left[-\widehat{\mathbf{u}}_h^*\cdot\widehat{(\,\mathbf{u}_h\cdot\nabla)\mathbf{u}_h} - \widehat{\mathbf{u}}_h^*\cdot\widehat{w\,\partial_z\mathbf{u}_h} - \frac{1}{\rho_o}\,\widehat{\mathbf{u}}_h^*\cdot\widehat{\nabla_h p} + \widehat{\mathbf{u}}_h^*\cdot\widehat{\mathbf{D}}_h + \widehat{\mathbf{u}}_h^*\cdot\widehat{\partial_z\kappa\partial_z\mathbf{u}_h}\right] \tag{2.12}$$

where the subscript h denotes a horizontal vector (in bold), u_h is the horizontal velocity vector and D_h represents horizontal viscosity implying energy dissipation. In the equation above $\hat{\cdot}$ can be 1D or 2D. Additional treatment of the original fields can be needed, *e.g.,* when the domain is not periodic. In any case, (2.12) is an equation describing the time evolution of the power spectrum components of KE (the left-hand side term) resulting from the wavenumber dependent work performed by the different rhs terms. As advection can only redistribute energy in a closed or periodic domain it can also only do so in wavenumber space. The sum of the second and third rhs terms vertically integrated fluxes energy across wavenumbers with no net sink or source. An evaluation of that flux can be formed as a wavenumber integral of their contributions to (2.12):

$$\Pi(k) \;=\; \int_k^{k_{max}} \mathcal{R}e\left[-\widehat{\mathbf{u}}_h^*\cdot\widehat{(\,\mathbf{u}_h\cdot\nabla)\mathbf{u}_h} - \widehat{\mathbf{u}}_h^*\cdot\widehat{w\,\partial_z\mathbf{u}_h}\right] dk\,. \tag{2.13}$$

So defined the KE flux is downscale (respectively upscale) wherever the integral is positive (resp. negative). The integral bound can be at k=0 or k=k_{max} if the total KE conservation by advection is strictly valid. This is not always the case, *e.g.,* when lateral fluxes of KE are permitted through open boundary conditions. Because the spectral budget is often difficult to interpret at low wavenumber anyway k=k_{max} is generally chosen as the integral bound. Note that in the presence of open boundary conditions periodization of the fields to be Fourier transformed is desirable and further complicates the interpretation of the resulting spectral balance. This is evident if periodization through windowing is used. An alternative is to apply domain mirroring to the input fields (*i.e.,* switching to discrete cosine transforms) is an appropriate choice (Denis et al., 2002). On the other hand, it should be kept in mind that the (u,v,w) field periodized (and extended) through horizontal domain mirroring are no longer fully nondivergent, which also complicates the interpretation of the spectral KE budget. Despite these issues the spectral approach has proved useful in analysing energy transfers (mainly kinetic energy but available potential energy

can, provided some developments be treated similarly, Molemaker and McWilliams, 2010,Roullet and Klein, 2009). The remainder of that section summarizes and elaborates on the findings of several studies having recently computed spectral fluxes for submesoscale resolving numerical simulations. Note that computing spectral KE fluxes from observations has been attempted (Scott and Wang, 2005) but estimates remain highly uncertain (Arbic et al., 2013; Qiu et al., 2014) in the submesoscale range.

Molemaker et al. (2010) demonstrate that the QG and non-Boussinesq non hydrostatic solutions of an Eady flow (Sec. 2.4) strongly differ in their submesoscale regime, with implications for the spin down or forced-dissipative equilibration of the solutions. The spin-down experiments are particularly enlightening. Fig. 2.14 represents the fraction of energy (kinetic plus potential) dissipated during the quasi-geostrophic and non-Boussinesq spin-downs of initially identical Eady flows. Results are plotted as a function of numerical resolution expressed in terms of a Reynolds number Re. Dissipation does not differ significantly between the two physics at low Re (corresponding to an eddy resolving Δx). As the submesoscale is progressively resolved small scale dissipation decreases dramatically in QG whereas it reaches a plateau in non-Boussinesq, with about 1/3 of the initial state energy being dissipated irrespective of resolution. Furthermore, unbalanced (ageostrophic) motions are shown to be of fundamental importance in establishing a direct route towards dissipation at fine scales[5].

Similar findings and conclusions are obtained by Barkan et al. (2015). In direct numerical simulations for a wind and buoyancy forced periodic flow they find a vigorous forward EKE cascade associated with frontal instabilities. Dissipation occurs preferentially at small scale in these simulations with a secondary role played by bottom friction, *i.e.,* the dissipation route toward larger scales.

Other numerical solutions for varied flows analyzed in **Capet et al. (2008d)**, **Klein et al. (2008a)** and **Marchesiello et al. (2011)** also exhibit robust for-

[5]The fundamental role of ageostrophic motions in the forward route to dissipation is further corroborated by diagnosing their contribution to the KE advective fluxes (in eq 2.13) in primitive equations solutions **(Capet et al., 2008d; Klein et al., 2008a)**. This result is in accordance with the theoretical work of (Molemaker et al., 2005; Müller et al., 2005) but it should be kept in mind that mesoscale frontogenesis with O(1) Rossby and Richardson numbers would suffice to produce a forward energy flux. The fact that the minor forward KE flux found in SQG solutions is not robust vis a vis horizontal numerical resolution **(Capet et al., 2008c)**.

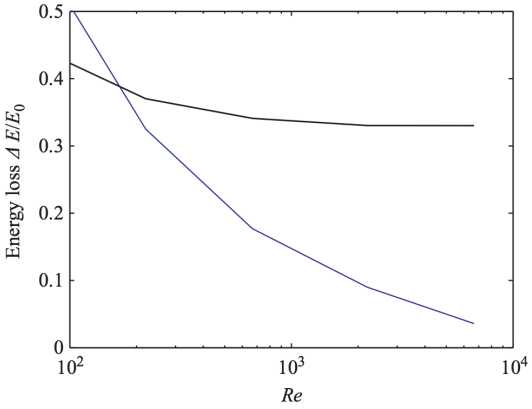

Figure 2.14: Total energy loss during spin-down for different values of Reeff : BOUS (Ror = 0.5, black) and QG (blue).

ward KE cascades in the submesoscale range, *i.e.,* at horizontal scales smaller than the first baroclinic deformation radius[6]. In these studies though forward KE fluxes have a negligeable importance in the energetic functioning except in a relatively shallow upper ocean layer. In **Capet et al. (2008d)** and **Marchesiello et al. (2011)** downscale KE fluxes rapidly vanish below 50-80 m depth (*e.g.,* see Fig. 2 bottom panel in **Capet et al. 2008d**). In **Klein et al. (2008a)** KE transfers remain important down to a few hundred meters depth. The actual depth range is indeed very sensitive to the upper ocean stratification as are the vertical velocities (see Sec. 2.5; **Capet et al., 2015a**). Low stratification environments have more available potential energy on which baroclinic instabilities can feed, larger APE to EKE conversion rates, and more efficient advective fluxes to redistribute this KE source across wavenumbers, toward finer **and** larger scales. In the solutions considered in **Capet et al. (2015a)** where the lateral buoyancy gradient (*i.e.,* also the vertical shear) is fixed and stratification $N^2(z)$ varies small enough N^2 permit a new form of submesoscale baroclinic instability that couples surface and interior Rossby modes, the so-called Charney instability (see Sec. 2.4). This further reinforces the

[6]A relatively good coincidence between the first deformation radius and the zero-crossing scale at which KE spectral flux switches from negative (KE moves upscale) to positive (KE moves downscale) is worth noting. In particular, zero-crossing is found at larger scale in the equatorial region where f is small *i.e.,* R_d is large. Because mesoscale resolving simulations do not resolve well the deformation radius scale they do not produce dowscale energy transfers (Schlösser and Eden, 2007)

intensity of the energy transfers. Nonetheless, the importance of the forward route to dissipation remains limited for the overall equilibration of the baroclinic flow.

There is thus an apparent contradictions between the situations explored in **Capet et al. (2008d)**, **Marchesiello et al. (2011)**, **Klein et al. (2008a)** or **Capet et al. (2015a)** where resolving submesoscale turbulence leads to a modest enhancement of small-scale dissipation in a relatively shallow upper ocean region and those in **Molemaker et al. (2010)** and Barkan et al. (2015) for which the energetics of the depth integrated flow is significantly altered by submesoscale turbulence.

Which view is more appropriate to the real ocean functioning has important theoretical and practical implications, particularly for how we design turbulence closures (Eden et al., 2014). To help clarify the issue we first note that both **Molemaker et al. (2010)** and Barkan et al. (2015) are characterized by large M^2/N^2 ratios ($M^2 = -\frac{g}{\rho_0}|\nabla_h \rho|$ is the lateral buoyancy gradient) over the entire water column such that the thermohaline structure has isopycnal surfaces intersect both the ocean surface and bottom. This is clear in Barkan et al. (2015) from their Fig. 3 (upper right panel; the Brunt-Vaisala frequency is 5 to 10 times smaller than in the real ocean). The basic state of **Molemaker et al. (2010)** has a constant M^2/N^2 by definition of the Eady problem and its dimensional value is chosen equal to $\varepsilon^{-1} = Ro/Fr^2 = 0.2$ which is very large (see their equation (2.1) and the parameter regime section 2.4; Fr and Ro are the Froude and Rossby number respectively). Nonlinear equilibration of the solution implies some restratification and a reduction of that ratio but we remain far from typical ocean values, as noted by the authors. As a result, the configurations considered in these two studies have deep reaching surface modes and frontogenetic circulations, which makes their estimates of bulk dissipation questionable.

Another important related remark concerns the intimate link between the submesoscale-driven forward KE route and the presence of atmospheric forcings to maintain a low stratification upper ocean against rapid restratification by mixed layer eddies (Fox-Kemper et al., 2008). For example the shutdown of wind forcing in the experiments described in **Capet et al. (2008d)** results in a rapid (few days) switch-off of submesoscale turbulence and their associated KE spectral transfers whereas mesoscale activity is essentially unaffected on such times scales. **Capet et al. (2008d)** propose several estimates to illustrate the significance of the downscale KE flux for the larger scale dynamics (their section 5d). One of them is a decay time scale for the depletion of mesoscale KE by submesoscale-driven dissipa-

tion. One issue with this estimate is the contrasted depth ranges associated with mesoscale and submesoscale eddies, several hundred meters versus tens of meters. It is therefore suggested that submesoscale-induced dissipation may act like a top-boundary frictional process. An alternative estimate is constructed based on the ratio of submesoscale-induced dissipation to the wind work and a value around 5% is found. The underlying interpretation is that submesoscale turbulence draws its energy from a small but non-negligeable fraction of the wind input (as opposed to from mesoscale flow) The latter estimate is more consistent with the results of the wind shutdown experiment mentioned above. This interpretation has since received support from LES simulations of a single front subjected to downfront winds Thomas and Taylor (2010).

Several more recent studies have shed further light on the complexity of the air-sea interactions in frontal environments with a coupled energetic functioning that can involve the upper ocean over hundreds of meters; trigger a variety of flow instabilities (Thomas et al., 2013; Mahadevan et al., 2012); and produce weakly stratified environments with distinct characteristics compared to usual fully mixed boundary layers (see Sec. 2.5).

Although it does resolve the entire fine-scale range of scales and processes we now tend to attribute the submesoscale-driven dissipation present in **Capet et al. (2008d)** to a similar dynamics. In retrospect, the schematic explicative of the relationships and energy transfers between the different scales of ocean circulation in this paper (Fig. 11 reproduced here with modifications in Fig. 2.15) should probably have explicitely included atmospheric forcings. Having said that some observations have shown the dissipation enhancement taking place locally in frontal zones, in (D'Asaro et al., 2011) and more importantly below the mixed layer (Johnston et al., 2011; Nagai et al., 2009; Kaneko et al., 2012; Nagai et al., 2012). Whether this enhanced dissipation results from the mesoscale frontogenetic tendency itself, unbalanced fine-scale instabilities, trapping of inertia-gravity waves produced away from the frontal region, interaction with atmospherically forced near-inertial oscillations (D'Asaro et al., 2011) or a combination of those remains uncertain (Johnston et al., 2011). More generally, the ways fronts equilibrate and evolve in nature, under complex external strain and atmospheric forcings are still poorly understood, despite ongoing numerical explorations at very fine scale (McWilliams et al., 2009b; Skyllingstad and Samelson, 2012; Hamlington et al., 2014). alford spontaneous

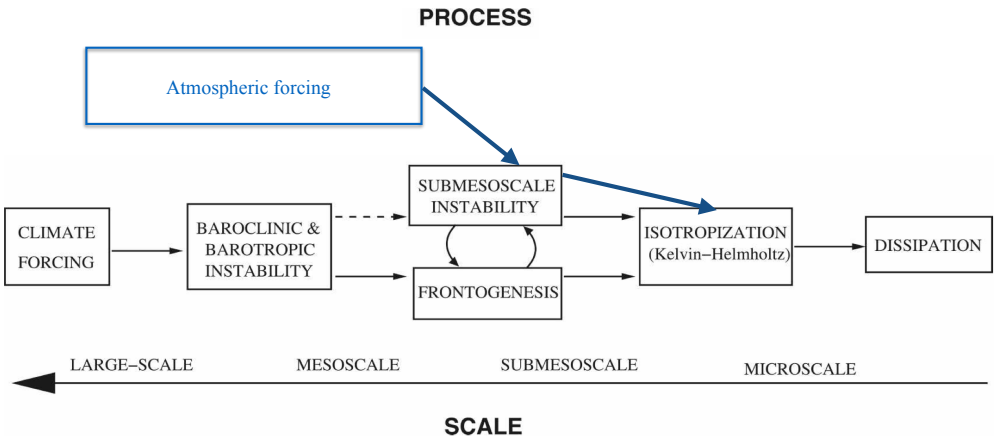

Figure 2.15: Schematic diagram for the important dynamical regimes by scale (increasing to the left) and their connecting total-energy transformation processes in an equilibrium oceanic circulation. Adapted from Capet et al. (2008d). Research posterior to this study tends to suggest that the role of atmospheric forcings is key to sustaining submesoscale turbulence (preferentially in the upper ocean) and its associated dissipation pathway. It also suggests that a significant fraction of the KE energy injected at submesoscale by short-scale baroclinic instabilities undergoes an inverse cascade and fuels the mesoscale (Sasaki et al., 2014).

Another missing piece in Fig. 2.15 pertains to the inverse cascade of KE from submesoscale to mesoscale (Klein et al., 2008b). It is now very clear that some of the submesoscale KE fueled by destabilizing atmospheric fluxes undergoes an upscale transfer and contributes to enhancing the mesoscale turbulent activity (Fox-Kemper and Ferrari, 2008)**(Capet et al., 2008d)**. A particularly enlightening demonstration of the importance of this inverse cascade has recently been offered by Sasaki et al. (2014) in which seasonal fluctuations in mesoscale KE are shown to respond to the modulations of mixed layer eddies driven by atmospheric APE inputs (see also Qiu et al., 2014).

Another instructive study on the effectiveness (or lack thereof) of the submesoscale cascade toward dissipation is under consideration for publication **Jouanno et al. (2015)**. This study is the main outcome of the ANR Jeune Chercheur SMOC (Submesoscale Ocean modeling for climate, 2012-2015) I have been awarded with G. Roullet, P. Klein and G. Madec as collaborators. **Jouanno et al. (2015)** investigate the fate of near-inertial (NI) energy injected by storms in an idealized ACC driven by simple climatological forcing fields. The ACC transport, thermohaline

structure, and turbulent intensity are comparable to observations owing to random fine-scale bathymetry. Analytical storm characteristics are fitted to the Southern Ocean climatology and includes the seasonal cycle. As a result NI energy inputs into the ocean are consistent with southern Ocean estimates. Different horizontal and vertical resolutions are used down Δx= 1 km in the horizontal and 320 levels in the vertical. Solutions with and without the storms are compared. They shed light on the significance of the interior dissipation due to NI motions or loss of balance alone, in mesoscale resolving and submesoscale permitting simulations. Results are shown in Fig. 2.16. Below the surface boundary layer, total (*i.e.,* vertical + horizontal) dissipation of NI energy increases slightly with resolution to reach levels around 2-6 10^{-10} W kg^{-1}, consistent with Southern Ocean microstructure measurements. The slight increase is presumably the consequence of a more intense upper ocean mesoscale turbulence which enhances the dispersion of NI motions and their downward propagation. In contrast, enhancing horizontal resolution in the absence of storms leads to a dramatic reduction of KE dissipation of subinertial currents. Dissipation asymptotically approaches 0. At Δx= 1 km energy dissipation is below 5 10^{-11} W kg^{-1} at all depths below 200 m, *i.e.,* around or below measurement levels of state-of-the-art microstructure sensors. These negligeable dissipation values in the interior of a semi-realistic ACC invites to a cautious interpretation of the results obtained in **Molemaker et al. (2010)** and Barkan et al. (2015).

In summary the emergence of a forward energy cascade present is a robust aspect of the transition from mesoscale to submesoscale. It is intimately tied to upper ocean ageostrophic effects that accompany quasi-balanced frontal flows, particularly under sustained APE inputs by the atmosphere to the ocean. Based on existing assessments the significance of this forward route to small scale dissipation for the overall energetic balance of mesoscale flows is limited. On the other hand, energy dissipation (and mixing) achieved by submesoscale frontal turbulence are important processes for the surface boundary layer and its interactions with the atmosphere and the subsurface. They may also be important in the local equilibration of frontal zones subjected to sustained straining as recent observations and numerical experiments would tend to confirm.

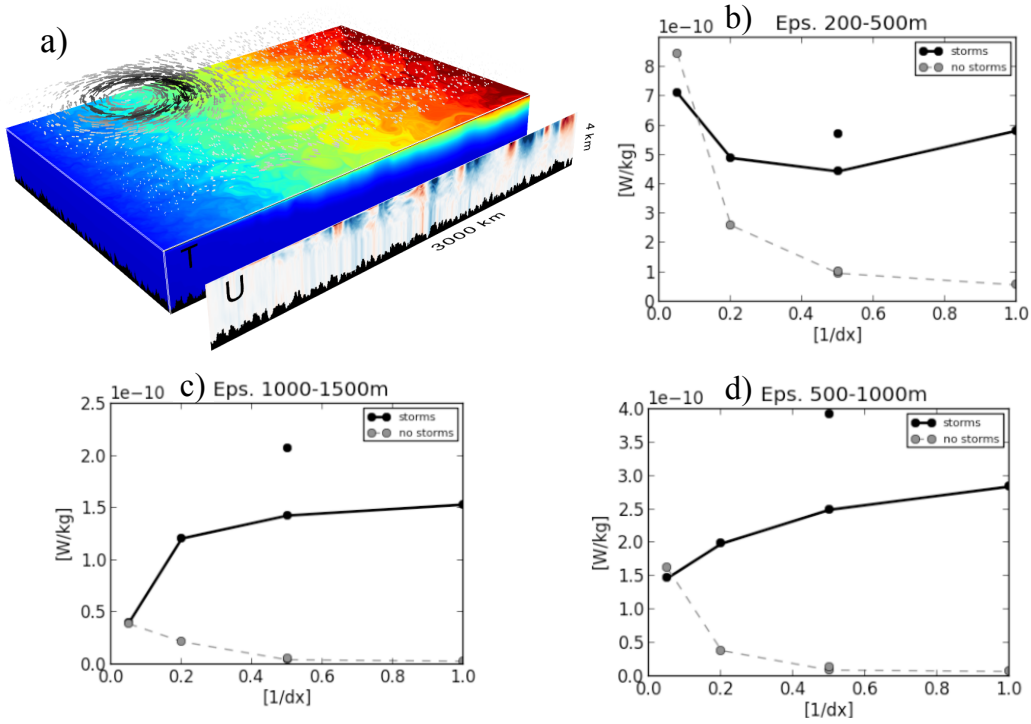

Figure 2.16: a) 3D representation of instantaneous buoyancy (rectangular box) and zonal velocity (vertical section) for the idealized ACC simulation at 2-km with storms analysed in Jouanno et al. (2015). The domain is a 2000 km long - 3000 km wide reentrant channel, representative of the the Southern Ocean between 40° and 70°S. Average ocean depth is 3500m with irregular bottom topography. The atmospheric forcings can include synoptic storms. b)-d): Total dissipation [10^{-10} W kg^{-1}] as a function of model resolution, in experiments with (black continuous lines) and without storms (gray dashed lines) averaged in the depth ranges 200-500m (b), 500-1000m (c) and 1000-1500m (d). Values are computed using 5-day snapshots of the entire domain for a 2 years period. Isolated dots represent for the 2-km experiment with 320 vertical levels.

2.7 Concluding remarks and perspectives

Research on submesoscale is progressively shifting from relatively generic studies and regimes to specific investigations of submesoscales in their diverse regional contexts. Thus, it has become evident that submesoscales play a variety of roles depending on the situations. These roles can concern the ocean physics of smaller/larger scales, ocean biogeochemistry, air-sea interactions. I tend to find this regional approach most attractive and intend to pursue it, in several contexts that are outlined below.

Our understanding of submesoscale dynamics and its effects on the ocean functioning is still partial; and so is the parameterization of its effects in our representations of the climate system. A major role played by submesoscales is to contribute to the restratification of the upper ocean wherever lateral fronts are present. A parameterization exists to mimic this process in model that cannot resolve the appropriate scales (Fox-Kemper et al., 2011). One of the limitations concerns weakly stratified environments in which the paradigm of a mixed layer directly overlying the well stratified interior is not suited. The study of more complex upper ocean boundary layers is in its infancy. Irrespective of their stratification major frontal regions of the world ocean are also places that are not well represented in OGCMs, in part because their state and functioning is strongly affected by turbulent motions at scales around or below 1km, with some indications that interactions between quasi-balanced and IGW processes are important (Whitt and Thomas, 2013, 2015; Grisouard and Thomas, 2015; Alford et al., 2013),**(Jouanno et al., 2015)**.

Understanding the submesoscale dynamics of mid-/high-latitude frontal regions and improving the associated OGCM parameterizations is a key priority because i) this is where the surface/subsurface exchanges heat, carbon and other biogeochemical tracers are most important to the Earth climate ii) ii) OGCMs are nowhere near resolving the appropriate processes and scales (Bachman and Taylor, 2014),**(Talandier et al., 2014)**. To help in this respect, I intend to keep working on the Southern Ocean fine-scale dynamics. Follow-up studies to **Jouanno et al. (2015)** should incorporate a wider range of IGWs, in addition to near-inertial waves forced by winds. While doing so, an eye will be kept on opportunities to account for ocean-atmosphere interactions. Through a collaboration with C. Talandier and J. Deshayes I would also like to contribute to the exploration of the weakly stratified Labrador sea dynamics. Concerning this latter perspective an inspiring study will be (Magaldi and Haine, 2015).

The overall impact of submesoscales on biogeochemical activity and ecosystems remains poorly understood. This partly stems from the stringent observational requirements to properly resolve the relevant scale range, ideally from $\sim$ 1 km or less to the regional/basin scales. Doing this observationally is beyond reach. Long term integrations of submesoscale resolving OGCMs with biogeochemistry modules are still uncommon. Levy et al. (2012) analyse mesoscale and submesoscale-resolving simulations for a double-gyre system resembling the North Atlantic. In the subtropical gyre submesoscale activity results in a net reduction of primary and secondary production, as a consequence of numerous changes in ocean physics that partly compensate each other. Likewise, compensating effects lead to a reduction of primary production but an increase in secondary production in the subpolar gyre. Such numerical ventures will become increasingly common. They will be most useful if the submesoscale dynamics they permit is an accurate representation of the more complex fine-scale processes taking place in the real ocean. Recent studies such as Bachman and Taylor (2014) confirm that the vertical motions and fluxes taking place under destabilizing atmospheric forcings will (at least) require careful evaluation. Contributing to this evaluation work and establishing standards to test and improve 1-10 km resolution OGCMs with biogeochemistry are natural perspectives I have for future collaborative research.

Some research plans on fine-scale dynamics consequences on ecosystems are formulated in the context of the West African perspectives (Sec. 3.3) where they fit more naturally because they have grown in contact with the southern Senegal upwelling center and my AWA colleagues. Likewise perspectives on more elaborate modeling approaches than the primitive equation simulations I have relied on so far are described in Sec. 3.3

By providing high resolution SSH along swaths tens of kilometers wide the SWOT altimeter (Fu and Ferrari, 2008) will provide for a (too) brief period of 3 years an invaluable opportunity to shed new light on submesoscale phenomena. The description of mesoscale processes will clearly be impacted down to horizontal scales of a few tens of kilometers. Vertical velocities seem to have relatively white spectra **(Klein et al., 2008a; Ponte et al., 2013)** down to scales of hundreds of meters. In addition, they pose stringent observational requirements to be estimated. Therefore, it is unlikely that their estimation will be directly affected by SWOT, unless new methods allow to heavily complement the SSH information, including

in the subsurface. This issue fits well with the ones mentionned above concerning the need to better quantify vertical fluxes. It is anticipated that the preparation of the SWOT mission will structure my research for several years, beyond the satellite launch (planned in 2020).

Chapter 3

Regional oceanography and turbulence regimes

Contents

3.1 The turbulent functioning of Eastern Boundary systems

In this section we describe how mesoscale activity affects the dynamical functioning of several upwelling sectors, in particular in terms of heat and buoyancy redistribution on lateral scales of tens to hundreds of kilometers. This description is based on research carried out with F. Colas and J. McWilliams primarily. The VOCALS program (Mechoso et al., 2014) **has provided important motivations for this work.**.

In Eastern Boundary Current systems, running along the West coasts of the Americas, Africa, and the Iberian Peninsula, strong equatorward winds interact with Earth's rotation to drive near-surface water away from the coast and promote upwelling of cold, nutrient-rich water from depth. Coastal upwelling plays a major role in the world ocean. By contributing to surface layers enrichment it helps sustain important nearshore fish resources. More generally, this process strongly influences the biogeochemical (BGC) functioning of the coastal ocean, with global implications on the budget of many BGC tracers. As the climate model are progressively refined enduring biases in EBS regions with consequences for the physics and biogeochemistry on much larger scales have started to draw increasing attention (Large and Danabasoglu, 2006; Grodsky et al., 2012; Richter, 2015). Beside environmental and climate issues, the turbulent nature of upwelling systems make them appealing regions to fluid dynamicists. In particular, upwelling systems lends themselves to idealization quite naturally because there are subject to one dominant process (upwelling) as opposed to a myriad of them like in other coastal areas.

Eastern boundary systems reveal ubiquitous turbulent activity suggestive of baroclinic instability, which has been confirmed numerically (Batteen, 1997; Marchesiello et al., 2003). Eastern boundary upwelling systems are not places where mesoscale eddies have an order one rectification effect on the dynamics like in the Antarctic circumpolar current. The influence of baroclinic instability and its associated cohort of turbulent structures is generally considered as modest. Having said that, kinetic energy of the eddies is much larger than that of the mean circulation and eddy fluxes of properties can have substantial effects as we are progressively learning. A significant part of my research has focused on the description and understanding of eddy fluxes in eastern boundary systems, with the California current System as a main playground. The California Current System (CCS) is one of the main four upwelling systems and roughly goes from the southern tip of Baja California (Mexico) to the Oregon/Washington (USA) border - although differences exist between subregions of this area, that spans almost 30 degrees in latitude. Compared to the other systems it has received significantly more attention and large datasets are available against which models can be reliably evaluated (Bograd et al., 2015). In terms of dynamics the CCS tends to be more frontal (Marchesiello and Estrade, 2009) than the other systems which does not automatically translate into the largest eddy rectification effects (see below).

Capet et al. (2008b), **Colas et al. (2012)** and more comprehensively **Colas et al. (2013)** further clarify the importance of baroclinic instability in driving mesoscale turbulence in several upwelling sytems. Their focus is on the role of mesoscale activity in the regional heat/buoyancy budget which complements a set of contributions on biogeochemic tracer turbulent fluxes in EBSs (Marchesiello et al., 2003; Plattner et al., 2005; Gruber et al., 2006; Lathuilière et al., 2010; Gruber et al., 2011),**(Chenillat et al., 2013)**. The most elaborate description of the turbulence role is in **Colas et al. (2013)** where the equilibrium eddy buoyancy fluxes $\overline{\mathbf{u}'b'}$ in three regional upwelling systems is analyzed using a decomposition across and along the mean buoyancy gradient field, *i.e.,* approximately an isopycnal/diapycnal decomposition

$$\begin{aligned} \overline{\mathbf{u}'b'} &= \frac{\nabla\bar{b}\times\overline{\mathbf{u}'b'}}{D^2}\times\nabla\bar{b}+\frac{\overline{\mathbf{u}'b'}\cdot\nabla\bar{b}}{D^2}\nabla\bar{b} \\ &= \quad\boldsymbol{\Psi}^*\times\nabla\bar{b}+\quad\mathbf{F}_b \end{aligned} \tag{3.1}$$

where $\mathbf{u}$ is the 3D velocity vector, $\bar{\cdot}$ is an averaging operator, $'$ indicates deviations from this average that select mesoscale perturbations, $D = |\nabla\bar{b}|$, and $\boldsymbol{\Psi}^*$ is the eddy induced vector streamfunction for the bolus velocity $\mathbf{u}^*$ ($\mathbf{u}^* = \nabla\times\boldsymbol{\Psi}^*$). The eddy-flux divergence in the buoyancy balance equation is

$$\nabla\cdot\overline{\mathbf{u}'b'} = \mathbf{u}^*\cdot\nabla\bar{b}+\nabla\cdot\mathbf{F}_b\,, \tag{3.2}$$

which confirms the advective nature of the flux component corresponding to the first term in the r.h.s. of (3.1). These cross-gradient, "adiabatic", advective fluxes are dominant in the stratified interior. With a suitable gauge choice that minimizes the irrotational, non-divergent component in a Helmholtz decomposition of $\nabla_h\bar{b}$, we find that the horizontal eddy flux is mostly down-gradient, consistent with the GM parameterization scheme. This is consistent with the dominance of baroclinic instability in our solutions with eddy fluxes well related to $\overline{w'b'}$. The eddy fluxes differ strongly between the interior ocean and the surface boundary layer. In the boundary layer where $\partial_z\bar{b}$ is small, both the eddy advection and residual diffusive flux $\mathbf{F}_b$ are horizontally oriented and diapycnal.

The major elements of the eddy buoyancy fluxes are summarized in Fig. 3.1. Fig. 3.1 is for the Peru-Chile upwelling but the represented processes are generic to Eastern Boundary upwelling systems. In the stratified interior, eddy buoyancy fluxes act to balance the effect of the upwelling-favorable winds, *i.e.,* to flatten the

tilted upper thermocline. The strength with which they do that is modest compared to other regions where surface fronts reach deeper such as western boundary currents (Bryan et al., 1999). This implies a shoreward eddy-induced flow above and an offshore flow in the lower thermocline, connected by a generally upward flow throughout the eastern boundary zone. The pattern of the eddy fluxes is broadly consistent with the expectation from baroclinic instability of the mean along-shore flow, but the relative strength among the three regional systems is not consistent with the traditional scalings (based on linear arguments). In particular, eddies are not very effective at advecting buoyancy in the California Current System oceanic interior despite the relatively high level of upper-ocean EKE. We attribute this to the concentration of stratification in the upper ocean (responsible for a rapid reduction of EKE with depth) and also possibly to the adverse role of topographic irregularities in disrupting baroclinic disturbances to be suboptimal with respect to release of available potential energy.

In the mixed layer there are several places where the combination of mean advection and atmospheric forcings produce surface temperature extrema, mostly simply nearshore minima from upwelling and offshore maxima from air-sea heating. Eddy fluxes act to reduce these extrema and maintain the equilibrium climate gradients. This is in particular the case off Peru-Chile and to a lesser extent off California. Another role turbulent motions play in the mixed layer has to do with frontal scale vertical circulations. The strength of this process varies from one upwelling system to another. It seems most intense in the CCS and weakest in the SHS. This gives rise to additional eddy-induced circulation cells within the mixed layer, mostly in the same sense as the thermocline cells, *i.e.,* shoreward flow above, offshore flow below, and upward flow in between. The gives a restratification effect. In this study model resolution is insufficient to fully represent frontal processes that extend strongly into the submesoscale range but the results are qualitatively consistent with those discussed in Chapter 2. In contrast, the lateral eddy fluxes in the mixed layer are overwhelmingly associated with mesoscale eddies that are well resolved.

As a sidenote on eastern boundary systems circulation and turbulence regime I briefly point out their large sensitivity to winds as discussed in **Capet et al. (2004), Capet et al. (2008b) and Colas et al. (2012)**. This is a research subject of great importance because the fine-scale structure of the nearshore winds remains uncertain, which results in large uncertainties in ocean circulation, fluxes

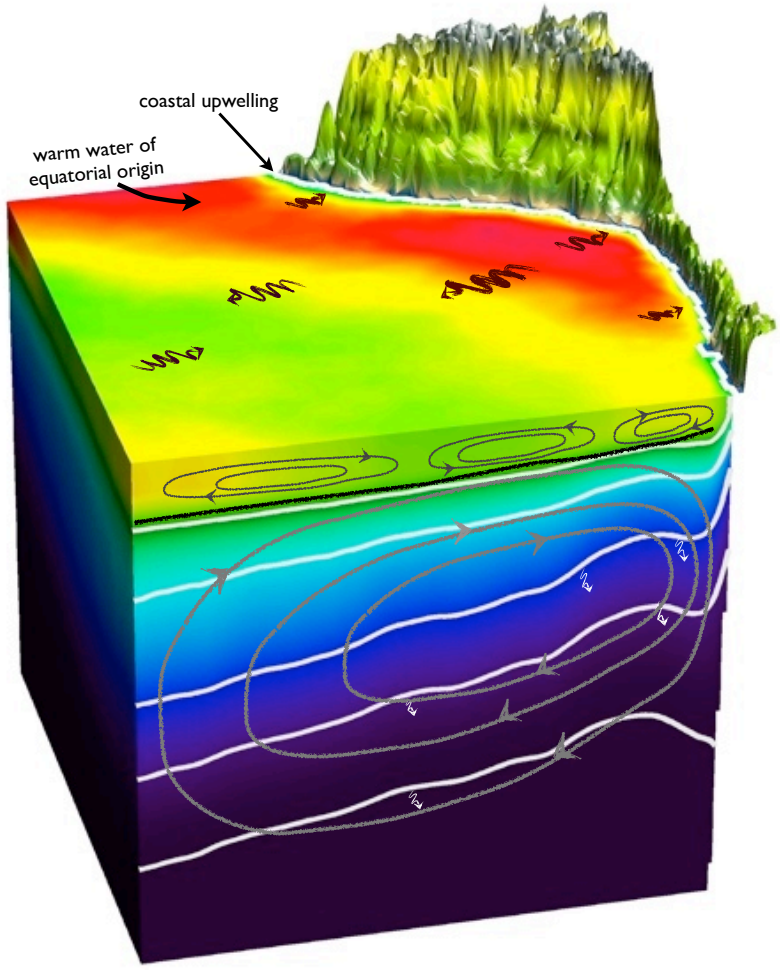

Figure 3.1: 3D schematic representation of the eddy effects as decomposed in Colas et al. (2013). In the mixed layer, the adiabatic advective component is associated with the restratification tendency of fronts with scales O(1 km) and is poorly simulated. It is represented by its associated streamfunction (black closed contours in the foreground vertical plane). The diabatic component acts to smoothen out surface buoyancy extrema and is shown as sinuous arrows in the top plane. Interior diabatic fluxes represented by white arrows in the foreground vertical plane are found negligeable in our mesoscale-resolving solutions. Interior adiabatic advective fluxes (whose associated streamfunction is shown with gray closed contours in the vertical plane) oppose Ekman-induced transport. Both adiabatic components can be seen as the manifestation of APE release, by baroclinic instability and (weak) frontogenesis near the surface. Modified from Colas et al. (2013).

and thermohaline structure. Over ten years have passed since **Capet et al. (2004)** and the issue remains although significant research has dramatically improved our understanding of the issue (Kara et al., 2008; Jin et al., 2009; Burls and Reason, 2008; Boé et al., 2011; Renault et al., 2012; Jacox and Edwards, 2012).

3.2 Going down in scale: functioning of the Southern Senegal Upwelling center

Research activities I have started developing since 2012 in West African waters are described. The main focus is on an original upwelling sector, the southern Senegal upwelling center (SSUC). Several SSUC characteristics make it an ideally suited place to investigate i) the coupling between subinertial and superinertial dynamical processes ii) trophic interactions and how they are modulated by ocean physics on a broad range of scales. The scientific approach combines regional modeling, insitu observation programs and in-depth analysis of satellite data (SST so far). The social context and potential benefits of this research are briefly discussed.

3.2.1 General context

Coastal countries in West Africa strongly depend upon their ocean, which provides major food supply and employment to local populations as well as export to foreign markets (Europe and Asia). This is particularly true for Senegal, Mauritania, Guinea-Bissau, Guinea and Gambia (henceforth WWA for Western West Africa), whose exclusive economic zone makes up the southern sector of the Canary current Upwelling system. The SCCS hosts one of the most productive world ecosystems. The abundant small pelagic fish resource is predominantly exploited by an artisanal fleet still expanding, competing with foreign industrial fisheries. This raises serious concern about exploitation levels, but with much uncertainty given the natural system variability, limited knowledge on fish stocks status and complexity of fishermen behavior (opportunistic strategies, fleet heterogeneity, biases in landing reports, diversity of fishing gears).

Coastal upwelling systems have received widespread attention for several decades owing to their importance for human societies. Although the primary driving mech-

anism is generic important difference exist between systems and also between sectors of each given system. Stratification, shelf/slope topographic shapes, coastline irregularities and subtleties in the wind spatial/temporal structure have a major impact on upwelling water pathways and overall dynamical, hydrological, biogeochemical (Messié and Chavez, 2014) and ecological (Pitcher et al., 2010) characteristics of upwelling regions. Over the past decade processes associated with short time scales (daily and faster) have progressively been incorporated which adds further complexity and many local specificities.

These advances have to a large extent taken place in the California Current System (Woodson et al., 2007, 2009; Ryan et al., 2010; Kudela et al., 2008; Lucas et al., 2011a) and to a lesser extent in the Benguela system (Lucas et al., 2014) and Northern Canary system (Espinoza-González et al., 2012; Rossi et al., 2013). Conversely, our understanding of West African upwellings remains to a large extent superficial (*i.e.,* guided by satellite and sometimes surface in situ measurements; Roy, 1998; Demarcq and Faure, 2000; Lathuilière et al., 2008; Benazzouz et al., 2014), low-frequency and relatively large scale (Cropper et al., 2014).

Since 2012, I am contributing to research and capacity building activities whose primary objective is to help West African scientists gain the type of understanding that has strongly benefited to other upwelling sectors, particularly off the U.S. West Coast. Given financial limitations and difficulties of different kinds the adopted approach is to concentrate our efforts in Senegal which encompasses a scientifically and socially attractive upwelling sector, the southern Senegal upwelling center (SSUC). The SSUC is characterized by a wide continental shelf which is a major fishing ground for artisanal fishermen. Our wish is to turn the SSUC into a coastal laboratory for innovative environmental studies. Given the key role of Senegal within the region, this would place West African scientists and societies at the center of an interdisciplinary scientific effort of international dimension. We see this as a potentially cost-effective way of empowering West Africa on the subject of marine changes. The research project SOLAB aims at an improved description, understanding, and numerical representation of the SSUC plankton ecosystem accounting for: the complex interactions between auto-, hetero- and mixo-trophs eukariotes spanning from O(1μm) to O(1cm); the role of the physical environment in shaping these interactions, particularly at fine scale. At the time of writing the project SOLAB rejected twice by the Agence Nationale de la

Recherche has no specific fundings. It progresses slowly on the margins of the AWA project (http://www.awa-project.org/), LMI ECLAIRS (https://www.ird.fr/la-recherche/laboratoires-mixtes-internationaux-lmi/lmi-eclair-etude-du-climat-en-afrique-de-l-ouest) and FP7 PREFACE (http://preface.b.uib.no/) in which I and SOLAB co-PI E. Machu are involved.

3.2.2 Physical Context

Between the Cape Verde frontal zone (which approximately runs between Cape Blanc ($\sim 21^o$N, Mauritania) and the Cape Verde archipelago (Barton, 1998), see Fig. 3.2) and Cape Roxo (12^o 20'N) the wind regime is responsible for quasi-permanent Ekman pumping and winter/spring-time coastal upwelling. The former extends hundreds of kilometers offshore and drives a large scale cyclonic circulation whose manifestation includes the Mauritanian Current (MC hereafter, see Fig. 3.2). The MC differs from poleward undercurrents typical of many upwelling systems in that it is generally intensified at or close to the surface (Peña-Izquierdo et al., 2012; Barton, 1989), reflecting the strength of the forcing. In the south, the MC connects with the complex equatorial current system and the connection involves a quasi-stationary cyclonic feature, the Guinea dome (more details can be found in Barton 1998, Arístegui et al. 2009). Fig. 3.2 is suggestive of the role of the MC in maintaining a relatively warm environment in the immediate vicinity of the shelf break over the latitude band 12^o-17^oN, despite sustained coastal upwelling.

Seasonality of hydrology and circulation of the coastal ocean off this part of West Africa are tightly controlled by the displacements of the Inter-Tropical Convergence Zone (Citeau et al., 1989). During the monsoon season (Jul.-Oct.) weak westerly winds (interrupted by occasional storm passages and easterly waves) dominate and the region receives the overwhelming fraction of its annual precipitations. From approx. November to May the ITCZ is located to the south and upwelling favorable trade winds dominate. Their peak intensity is in February-April. The migration of the ITCZ also drives the cyle of freshwater run-offs to the coastal ocean, a presumably large fraction of which occurs through the Senegal, Sine-Saloum, Gambia and Casamance river outflows. The effect of freshwater input to the coastal ocean is evident during the monsoon season when warm and fresh so called Guinea waters cover most of the area. It is conversely insignificant during most of the upwelling season.

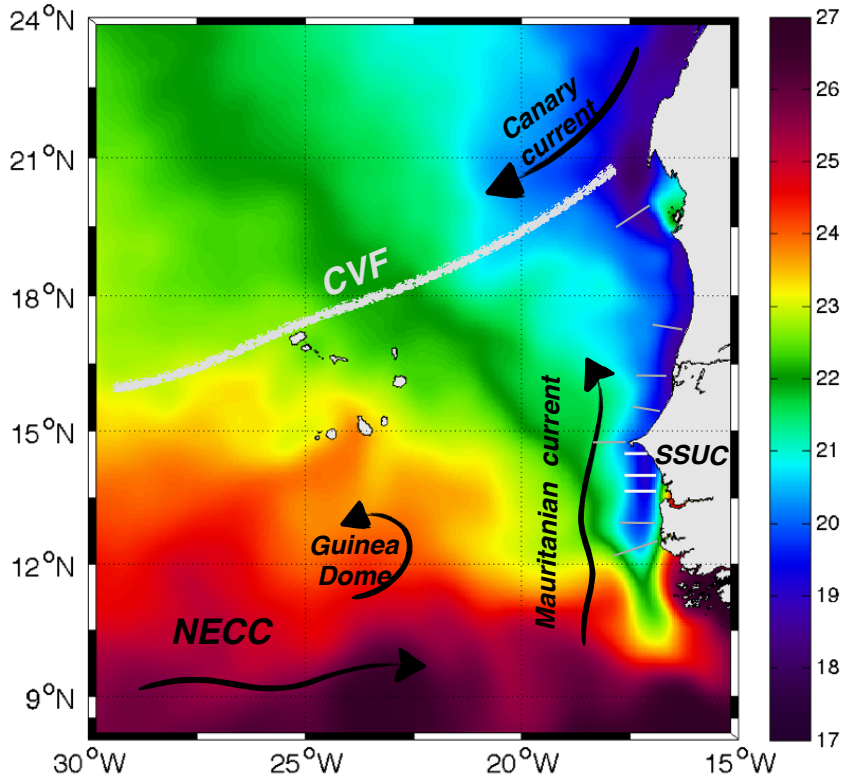

Figure 3.2: Averaged OSTIA composite SST over the northeastern tropical Atlantic for the period 21 February - 18 March 2013 corresponding to the UPSEN2-ECOAO field experiments. Superimposed is a schematic representation of the main circulation features of the region including the North Equatorial counter-current (NECC) and the Cape Verde Frontal zone (CVF, thick gray). Our study area, the southern Senegal upwelling center (SSUC), stands out as the tip of the coastal upwelling system. White lines indicate the location of the three main hydrological transects around which the field experiments UPSEN2 and ECOAO (2013) were designed. These transects were repeated in 2014 as part of the regional-scale 2014 AWA experiment which included measurements further north and south along the gray lines. A more specific experiment (UPSEN) took place in 2012 in the SSUC.

Two coastal sectors can be distinguished in this region, based on small distinctions in their atmospheric forcings, influence of the surrounding ocean and also shelf/slope morphology. North of the Cape Verde peninsula the shelf is relatively narrow (up to the Banc d'Arguin), and, because this is the northern limit of the ITCZ migration, the upwelling season is longest. A number of constraints and deliberate choices have led us to focus on the southern sector: accessibility from Dakar harbour; gentler sea states than North of Dakar; originality of the geomorphology.

After pioneer study in the 1980's-1990's the Southern Senegal upwelling center has been understudied (observationally and numerically) for about 20 years while it has several original specificities that make it a very attractive testbed for integrated physical/biological/biogeochemical and ocean/atmosphere research. The wind regime exhibits regular patterns on time scales of days to the season. Outside the summer season, upwelling events lasting from days to a couple weeks alternate with relaxation periods. Wind aloft upwelling comes from two dominant directions, the NW and the NE with the latter (resp. the former) being more (resp. less) prominent toward the end of the season (from January till April). The daily cycle is well marked with a tendency for upwelling winds to strengthen at night. Overall, wind variability on seasonal, intraseasonal to daily time scales suggests a strong coupling with the larger scale sub-Saharan meteorological features (Mesoscale Convective Systems and the Saharan heat low) that would need to be elucidated. Given the width of the shelf the nearshore dynamics ($\sim$ 50-100km from the coastline) is strongly constrained by friction. Together with the relative alongshore invariance of the topography this yields well-defined separations between SSUC subareas with distinct physical and biogeochemical regimes. A high-resolution SST image for April 17 2010 reveals the typical cross-shore structure of the system (see Fig. 3.3c). The inner shelf within 20-30 km from the coastline is partly sheltered from the upwelling, waters tend to be warm and rich. Over the mid-shelf (40 to 70 km offshore) is where most of the upwelling occurs with a maximum intensity south of the Cap-Vert peninsula (Dakar, Senegal) and a progressive reduction southward. Farther offshore on the shelf and beyond the shelf break, upwelling may also take place but waters are generally increasingly warmer and stirred by meso/submesoscale turbulent structures.

A resembling zonation is found off Western Sahara (Barton et al., 1977) but it has not received significant attention either. On the other hand, the better known

shelves offshore of Oregon and central Peru have distinct SST patterns and cross-shore structure with a comparatively insignificant inner shelf region. It is evident from the few existing studies that a broad inner shelf has important implications for the ecosystem (Roy, 1998) and the existence of a small pelagic fish nearshore nursery in the SSUC may be one of them. On the basis of these limited elements our research plan aimed at better understanding the SSUC dynamical functioning combines standard and more ambitious scientific goals.

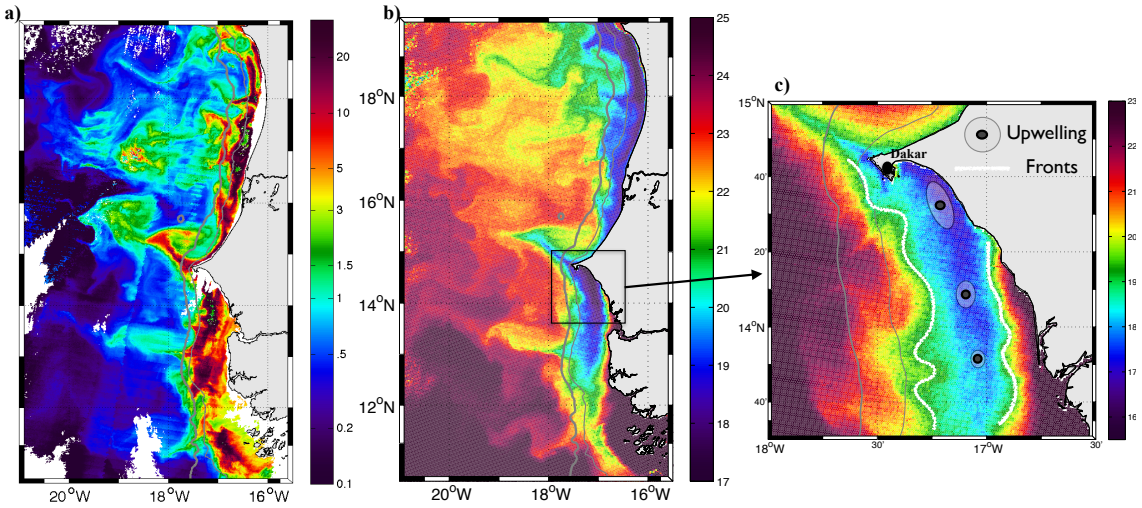

Figure 3.3: MODIS Chlorophyl-a (a) and SST (b,c) on 10 April 2010. Panel c) is a zoom on the SSUC sector in which the system zonation is indicated with three areas separated by two SST fronts: the warm inner shelf; the cold mid-shelf subjected to upwelling ; and the progressevily warmer outer shelf and slope region. The 100 (resp. 1000 m) isobath is represented with a thin (resp. thick) gray line. Note the reduced export of Chla south of Dakar compared to north of Dakar.

Standard goals include an appropriate description of the shelf subinertial circulation, of its cross-shore exchanges (mean and eddy) with the open ocean, and more generally of its connections with the regional scale dynamics.
Schematically, the shelf break is the porous offshore boundary of the SSUC across which flow subsurface Atlantic central waters feeding the coastal divergence, and surface waters advected offshore by the Ekman transport. Surface exchanges across the shelf break are evidently affected by mesoscale turbulence during sustained upwelling events with cold upwelling water exiting the shelf as filaments (see Fig. 3.3 and **Ndoye et al., 2014**). Upwelling filaments have received tremendous attention in the context of the California Current System and northern Canary system

(Ramp et al., 1991; Barton et al., 2004; Rossi et al., 2013). They have been identified as important subduction places that have the potential of significantly affecting biogeochemical coastal budgets transporting large amounts of carbon and nitrogen down to 200m depth or more (Barth et al., 2002). Offshore export in filaments is also detrimental to primary production (Gruber et al., 2011; Hernández-Carrasco et al., 2014). Little is known about SSUC filaments and their impact on export of biogeochemical material.
SST patterns (*e.g.,* , in Fig. 3.3c) suggest a continuous upwelling attenuation toward the south. Off Guinea Bissau the cold SST signal fades away significantly. This is in part due to slower winds in the south (see Fig. 14 in Ndoye et al. 2014). The degree to which advection from the north fuels productivity further south, as opposed to local upwelling is unknown but should also be quantified.
On larger scales, the way the system is connected to the equatorial band needs to be clarified. The shape of the coastline between 0 and 10^{o}N suggests some attenuation of oceanic coastal wave signals from equatorial origin. On the other hand, the Mauritanian current is an important circulation ingredient that has connections with the Northern Equatorial Counter Current. The Mauritanian current contributes to the renewal of slope waters that feed the upwelling and would need to be investigated.

A more ambitious focus of my research in the SSUC is on fine-scale processes and their interactions with the larger scale environment. Of particular interest is the functioning of the inner shelf and its sources of enrichment, given its apparent separation from the upwelling area during most of the upwelling season (see Fig. 3.3c and 3.5). The task is immense given the sparseness of existing in situ observations (manpower and financial resources are also significantly more limited than for typical coastal regions off the U.S. or European shores).

These goals are being pursued to a large extent because they are key to making progress in the understanding of the ecosystem functioning. How we approach and tackle them is collectively elaborated with other dynamicists (P. Estrade, L. Marié, A. Lazar), biogeochemists (E. Machu) and fisheries scientists (P. Brehmer, T. Brochier, A. Sarre).

The SSUC environment leads to several key simplifications in its functioning. They arise from the regularity of the SSUC wind regime, the importance of frictional control over the circulation, and the north-south quasi invariance of the topography. In addition, interannual variability arising from Atlantic (*e.g.,* North Atlantic Oscil-

lation) or global (*e.g.,* El Niño) climate modes have a relatively small imprint in the SSUC. Major insight can thus be gained by studying a small number of recurrent system states during the upwelling season. Long-term modifications of the system should also emerge more clearly than in many oceanic regions. These simplifications have, so far, greatly accelerated our research (*e.g.,* , Ndoye et al., 2014) and our expectation is that they will continue to do so in the coming years. It is also expected that our approach combining insitu and satellite measurement analyses with modeling will lead to rapid progress owing to synergies between them. Recent findings pertaining to each of these approaches are discussed below.

3.2.3 SST patterns and dynamics of the Southern Senegal-Gambia upwelling center

A systematic investigation of the L2 SST MODIS has been carried out by S. Ndoye, PhD student (2013-2015) under my supervision. In Ndoye et al. (2014) analyses and careful examinations of over 1500 satellite images of sea surface temperature scenes contextualized with respect to wind conditions allow us to precisely document SST patterns and variability on a broad range of time scales, for the upwelling period (Oct-May). Insofar as SST reflects ocean dynamics our examination of the MODIS SST archive also offers an interesting perspective on the SSUC dynamics[1]. Given the number and high spatial resolution of the images this perspective includes fine-scale details of the SSUC functioning that are by construction (using monthly or seasonal averaging) statistically meaningful.

In this study we confirm the regularity and stability of the SSUC dynamical functioning (as manifested by the recurrence and persistence of particular SST patterns). The analyses also reveal subtle aspects of its upwelling structure (see Fig. 3.4): 1- shelf break cooling of surface waters consistent with internal tide breaking/mixing ; 2- synoptic variability presumably driven by instabilities of the shelf/shelf break/slope current system ; 3- complex interplay between local upwelling and the Mauritanian current off the Cape Verde headland ; 4- complexity of the

[1]SST is a nonconservative tracer strongly affected by air-sea fluxes and having complex links with subsurface shelf dynamics and its thermohaline structure. This brings important limitations to the approach but our focus is on upwelling dynamics which is generally well reflected in SST. Furthermore, relying primarily on nighttime images ensures that SST is representative of temperature in a 10-30 m mixed layer.

coastal front separating the inner- and mid-shelf regions; 5- significance of the SST (and wind) diurnal cycle suggesting that large uncertainties exist in the SSUC heat budget. 1-2 and to a lesser extent 3 are corroborated by observations carried out during UPSEN2 and ECOAO in 2013 (see next section). 4- remains speculative at this stage. 5- will be in investigated in the context of the PhD work of Lala Kounta (IRD ARTS, 2015-2017) under my supervision.

SST climatologies in upwelling systems are subjected to major uncertainties given the unreliability of standard algorithms that separate good and bad pixels (Dufois et al., 2012). An outcome of Ndoye et al. (2014) has been a SST climatology for the area that differs significantly from other products and is more reliable, owing to careful visual screening. The SST annual cycle can be simply described in terms of expansion (from Oct.-Nov. to Feb.) and rapid retraction (May) of the cold water tongue present over the southern Senegal-Gambia shelf (see Fig. 3.5a-c). Likewise, upwelling and relaxation events with time scales of 3 to 10 days modulate the upwelling intensity and manifest themselves, on average, as expansion/retractions phases of the upwelling tongue. This SST climatology is systematically used to evaluate model skills in our modeling activities (Sec. 3.2.5) (cross-shore frontal strength, SST minimum location over the shelf . . .).

3.2.4 The southern Senegal upwelling center: state and functioning during the UPSEN2/ECOAO field experiments (Feb.-Mar. 2013)

Acquiring observational knowledge and competencies has been an important of my occupations over the past three years. I was on the UPSEN 2012 experiment (Chief-scientists: A. Lazar and P. Estrade). My responsabilities have been more significant during the UPSEN2 2013 (R/V Antéa; chief scientist) and AWA 2014 (R/V Thalassa; chief scientist assistant). This has offered me new perspectives on coastal ocean functioning that are great complements to my regional modeling views.

Measurements for the ocean physics carried out in 2013 during UPSEN2 and ECOAO have now been analysed and a manuscript will be submitted within weeks (Capet et al., 2015b). Because this manuscript helps understand some of the perspectives laid out in the final section it is proposed as an appendix.

A key objective was to repeatedly map 3 cross-shore transects allowing us to

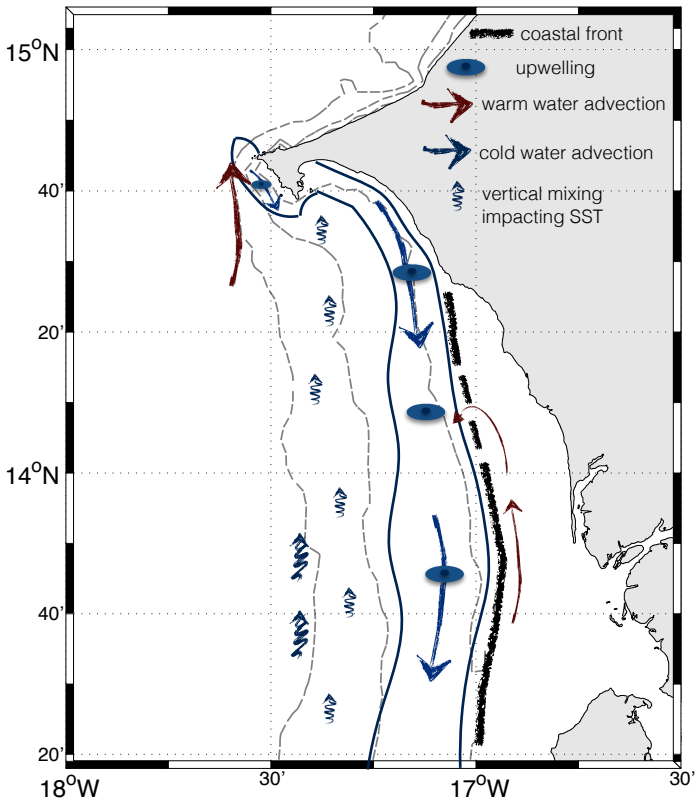

Figure 3.4: Schematic representation of the key dynamical elements apparent during the Feb. to Apr. upwelling period from our analysis of MODIS L2 SST patterns (Ndoye et al., 2014). Sinuous thin lines delineate the upwelling zones. Grey dashed lines represent the 20, 50 and 100 m isobaths. The latter roughly coincides with the shelf break. Thick black lines indicate the position of the coastal front which is represented as partly interrupted around 14°10'N. We tentatively relate this to the bifurcation of a (possibly intermittent) northward flow of warm coastal water (red arrows). Off the Cape Verde headland, interplay between the poleward flowing Mauritanian current (thick red arrow) and the localized coastal upwelling is often noticeable in MODIS SST images. Elevated probability of SST minimum presence at the shelf break under low wind conditions (see Fig. 10 in Ndoye et al. (2014)) is interpreted as a consequence of internal tide breaking. This effect is most evident in the southern part of the domain but may also be present in other parts of the shelf including just south of Dakar in the vicinity of the 50m isobath.

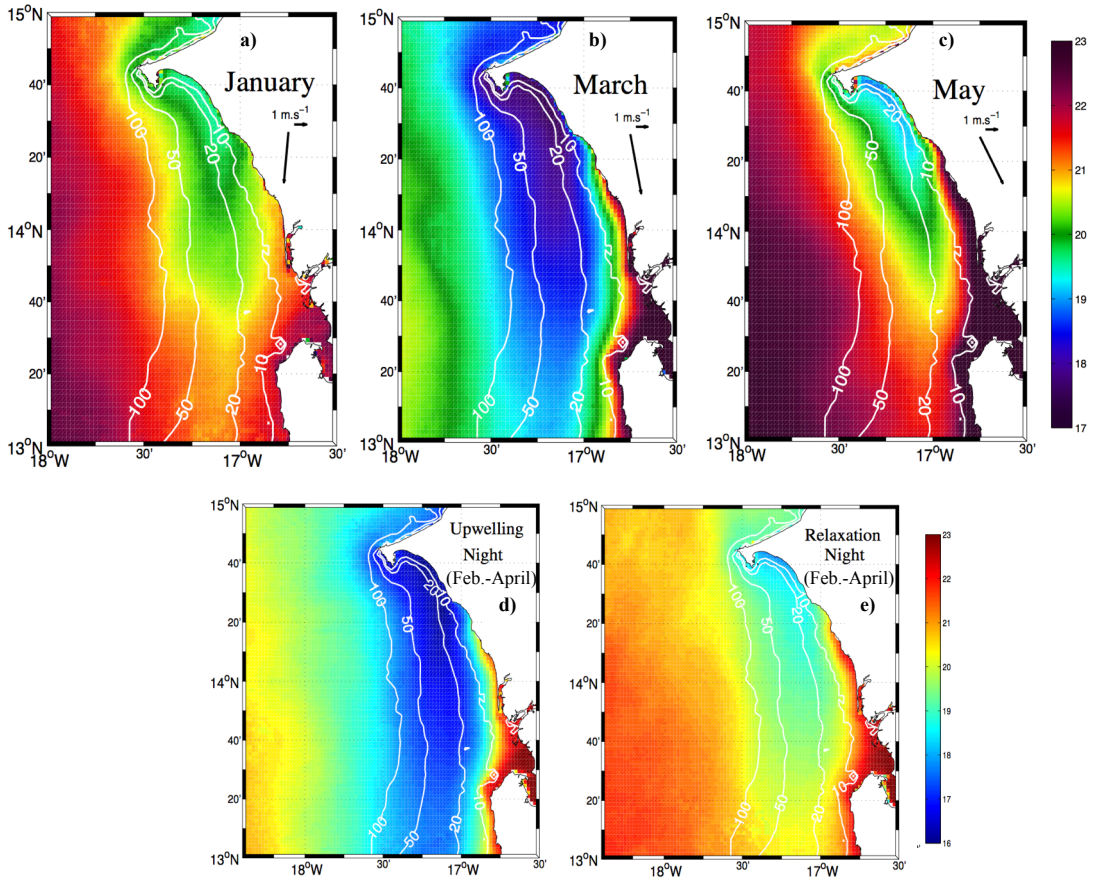

Figure 3.5: a-c) Monthly mean SST climatologies for January, March and May, constructed using all available SST images over the study period (2005-2012). Isobaths are indicated from 10 to 100 m depth (white lines, depth in meters). Climatological winds at the Dakar Airport weather station (DWS) are shown for each month as black vectors. d-e) Composite average SST during February to April upwelling events (d) and relaxation (e) conditions respectively defined by 4-day averaged DWS winds being above (resp. below) 5.5 m s^{-1} (resp. 4 m s^{-1}).

resolve the variability of the SSUC on synoptic time scales (around 5 days) and north-south contrasts, *i.e.,* an alongshore space scale of the order of 100 km. In the cross-shore direction we covered the mid-shelf, outer shelf, upper slope but only the offshore part of the inner shelf. Water shallower than 15 meters were not routinely accessible and waters shallower than 10 meters were not explored, owing to restrictive safety rules. Ship based measurement were complemented with moored instruments: 5 ADCPs located over the central transect in 23-28 m of water depth and 1 thermistor chain in about 27 m water depth. These mooring were recovered toward the end of a second experiment ECOAO (PI: P. Brehmer) focused on the trophic chain from phytoplankton to small pelagic fish (and their eggs and larvae). ECOAO and UPSEN2 were strongly coordinated. In particular, the three cross-shore transects were repeated during ECOAO.

Overall, this $\sim$ 4 weeks intensive measurement period sheds light on the synoptic and superinertial variability of the SSUC. A number of findings complement and qualify previously known aspects of the SSUC dynamics. They also lay out the physical context to which biogeochemical and fish observations will be related.

The way the upwelling zone and front positions are established has previously been seen as a consequence of the shutdown of surface Ekman transport in shallow waters, in a 2D vertical subinertial framework. Essential to the conceptual model is the assumption that momentum is vertically well mixed inshore of the upwelling zone so that wind and bottom friction equilibrate without involving the Coriolis force (Estrade et al., 2008) (see Fig. 3.6). In this conceptual model it is wind strength which modulates the position of the front by affecting surface (Lentz, 1992) and, more indirectly, bottom turbulence intensity. Overall, our continuous observations reveal that the water column is rarely destratified and momentum is not well mixed even tens of kilometers inshore of the upwelling front. Although the model may retain some validity at other times or on different time scales, other processes may be more important when trying to rationalize the functioning of upwelling over periods of a few weeks, including: where subsurface water is upwelled ? Which parts of the shelf it enriches ? And how the enriched area and its frontal edge may migrate across-shore with time ? In the light of our analyses and findings we hypothesize that two previously undiscussed processes (with possible interplays between them) play a role in the synoptic variability of the SSUC.

First, the upwelling tongue and its frontal separation with the offshore waters

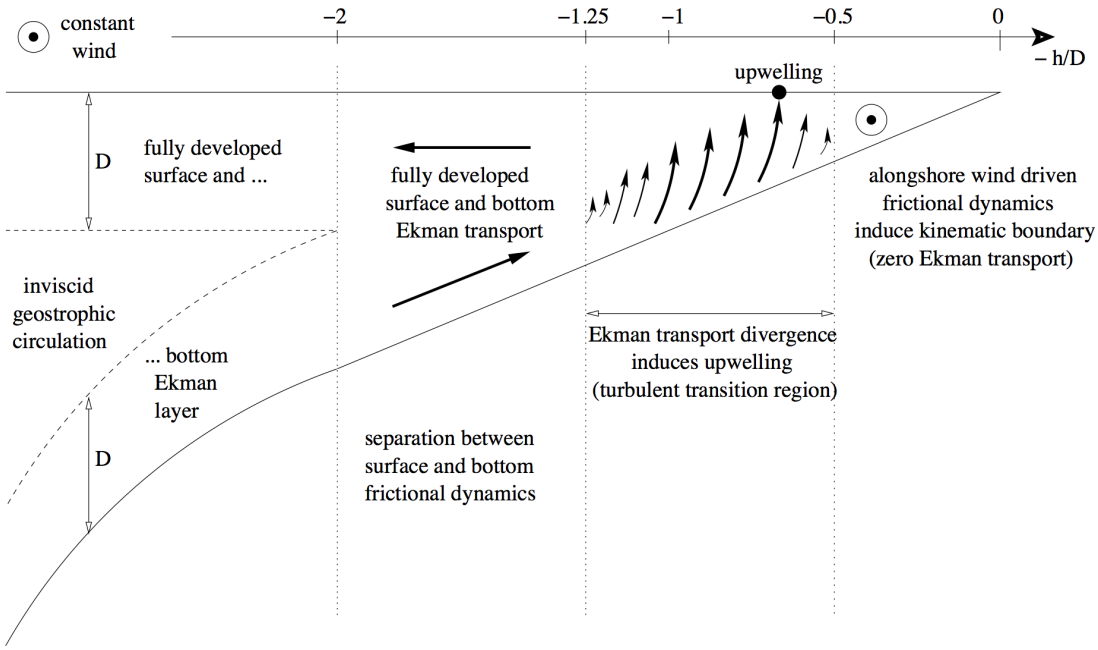

Figure 3.6: Conceptual view of the Ekman model over a shelf topography presenting the different physical processes at work in a depth across-shore distance section. The crucial role is played by the interaction of bottom and surface Ekman layers for sufficiently shallow depths. The upwelling cell is found in a transition zone between 2 regimes : a coastal regime completely dominated by friction whereby the flow is parallel to the coast, and a deep ocean regime where the top and bottom Ekman layers are well separated (they still interact but indirectly through the interplay of the interior geostrophic flow). The inshore boundary of the transition zone is defined as the place where the top and bottom Ekman layers overlap. Because it encloses an area where no cross shore flow is permitted, this boundary acts as kinematic barrier for Ekman transport. In this area, the frictional effects due to wind and bottom stresses compensate and maintain the flow in the alongshore direction throughout the entire water column. Reproduced from Estrade et al. (2008).

is subjected to mesoscale disturbances which bring important non 2D effects. In the northern part of the system, a recurrent expression of mesoscale turbulence during UPSEN2/ECOAO was through $50-100$ km anticyclones that remained quasi-stationnary for one to a few weeks offshore of the Cape Verde peninsula (see Fig. 3.7). These Cape Verde anticyclones (CVAs) develop as meanders of the system formed by the Mauritanian current and shelf upwelling currents abut on the Cape Verde peninsula. CVAs have a clear influence on the shelf upwelling structure. They tend to confine the upwelling tongue inshore in the northern SSUC and promote offshore export in the surface layer near 14^oN. A better understanding of the unstable behaviors of the shelf/slope current system would be useful and in particular i) the conditions under which they can influence the shallow parts of the shelf (as around 27 February) ii) their preferential evolution sequences and their relation to the environmental conditions.

Another possibly important mechanism affecting the distribution of upwelling and the evolution of the frontal zone is mixing by internal tide dissipation over the shelf. To frame the issue, we find useful to examine the fast upwelling limit case exemplified by central California where w^{up} is classically tens of meters per day **(Capet et al., 2004)**. In such a situation the upwelling process may be adequately pictured as adiabatic upward advection while vertical mixing and diabatic processes are ignored because they merely perform the unescapable incorporation of upwelling water into the mixed layer. That incorporation is tightly slaved to the vertical advection itself. Heterogeneities in vertical mixing, resulting from external processes (internal tide dissipation) or from heterogeneities directly associated with the upwelling dynamics (*e.g.,* nearshore wind drop-off) can only produce minute changes to where and when upwelling water is being entrained into the surface mixed layer. They also have a relatively limited time period during which they can act on upwelling water because w^{up} is large.

A radically different type of surface layer enrichment regime has been identified over some shelves where patchy episodes of vertical mixing triggered by inertia-gravity wave activity are the key process that incorporates subsurface water into the euphotic layer while unspecified adiabatic processes are in charge of renewing the pool of bottom water awaiting mixing with surface waters (Sharples et al., 2007; Williams et al., 2013; Tweddle et al., 2013) (see also Lucas et al. 2011b in which southern California internal tides are shown to be also responsible for the across-

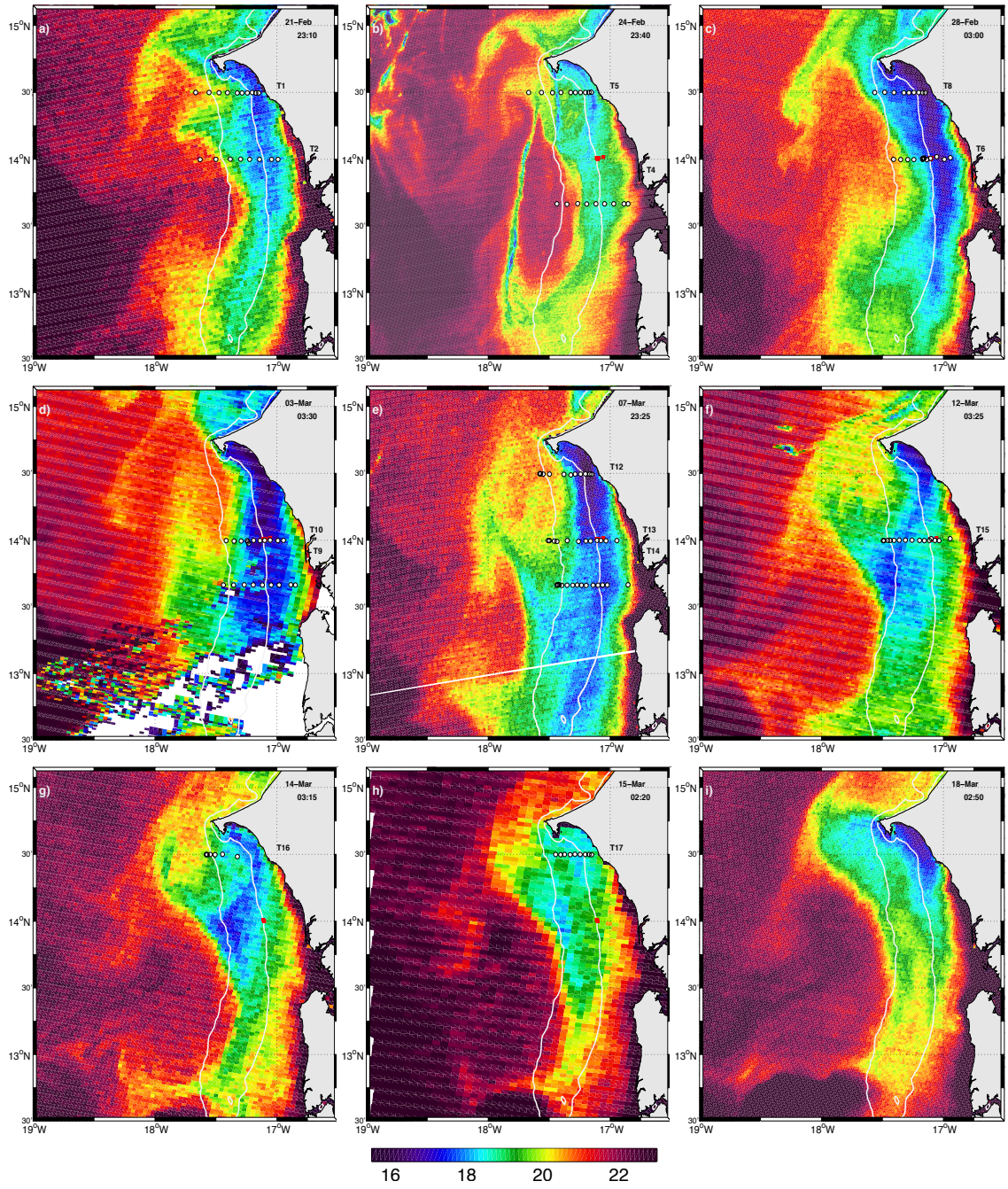

Figure 3.7: MODIS SST at different times (given in the upper right corner of each image) during the UPSEN2/ECOAO cruises. CTD transects carried out within 1.5 day (prior or after) of the scene are indicated with white dots and labeled on land. Mooring locations are indicated with red square markers when they are deployed at the time of the scene (indicated in the upper right corner). 30 m and 100 m isobath are shown with white lines. The latter adequately defines the shelf break. Small areas possibly contaminated by clouds are not flagged, e.g., along the line that joins (-18° W,13° 30'N and the Cape Verde peninsula in panel b). ∼ 50-80 km mesoscale eddies abutting on Cape Verde are frequently seen during the experiments. They are refered to as Cape Verde anticyclones or CVA.

shelf replenishment flux of nutrients).

The SSUC situation uncovered during UPSEN2/ECOAO may represent an intermediate situation where partial decoupling between upwelling-driven vertical advection and mixing leads to bottom water incorporation in the surface layer through multiple sporadic mixing episodes. In the SSUC we expect the onshore flow to be strongest near the bottom (Lentz and Chapman, 2004) and a scaling for upward velocities can thus be constructed as $w^{up} \sim u_b \times s$ where s is the bottom slope and u_b a typical near-bottom cross-shore velocity value. Based on mooring observations reported in this study and consistent with observations in other upwelling sectors $u_b \approx 5$ cm s^{-1}. Water parcels thus need around 10 days to travel from the shelf break to the mid-shelf upwelling zone and, with a shelf slope around 2 %, an estimate for w^{up} is 8 m d^{-1}. This provides ample time for mixing episodes to take place, along complex pathways that evolve under the influence of variable winds and mesoscale activity. As a result, upwelling dynamics may be more disrupted by IGWs in the SSUC than in other upwelling sectors (Schafstall et al., 2010; Avicola et al., 2007).

An unknown but presumably significant fraction of the energy driving mixing in the SSUC arises from the fission of internal tides into nonlinear internal waves that subsequently break and dissipate. The effect on tracer vertical fluxes is not known at present and depends on the distribution of IGW breaking aided by subinertial (Avicola et al., 2007) and possibly near-inertial shear, which was also observed during the experiment. Based on studies for other shelves this effect deserves careful attention. In particular, it would be interesting to know the extent to which IGW breaking contributes to the progressive enrichment of the shelf bottom layer in phytoplankton[2].

Thermohaline heterogeneities efficiently contribute to the disruption of IGW propagation. During UPSEN2 and the beginning of ECOAO an upwelling front is well marked and impinges on the continental shelf. Preferential dissipation of IGWs in the offshore vicinity of the upwelling front is supported by many vertical

[2]The significance of bottom layer enrichment for the SSUC ecosystem functioning is supported by the calculation of a time scale associated with the primary production head start due to the enrichment of bottom waters. Chlorophyl bottom concentrations increase by one half to over one order of magnitude between the shelf break and the 40-50 m isobath (where the water column is still stratified; see (Fig. 4 in Capet et al. 2015b). The corresponding head start for primary production should be of several days, given exponential growth rates in the range 0.2-0.5 d^{-1} (Landry et al., 2009).

profiles of tracers. This has potentially important dynamical implications. Additional observations will be needed to further evaluate the significance of IGWs "pounding" on the upwelling front in its tendency to migrate offshore. A tentative estimation of IGW energy at the mid-shelf moorings leads to upwelling front offshore displacements of a few hundred meters per day which is modest (*e.g.,* in regard to displacements associated with mesoscale disturbances) but uncertainties are large. A more qualitative element supporting the dynamical importance of IGW mixing is the sequence of satellite SST images during UPSEN2/ECOAO showing the progressive erosion of Cape Verde mesoscale anticyclones (Fig. 3.7). Concomitant in situ observations reveal intense interior mixing undergone by the thermocline waters within the CVAs. In contrast, SST images do not reveal significant submesoscale frontal activity in comparison to other situations (Capet et al., 2008e), hence lateral diffusive effects should be small. Our interpretation is that CVAs bring substantial stratification over the shelf, which in turn allows IGWs to exist and presumably erode that stratification, *i.e.,* contribute to the CVA decay.

Fig. 3.8 helps summarize our main findings and results. The southern Senegal upwelling system is situated over a broad continental shelf. So far its study had overwhelmingly relied on satellite images and focused on long time scales (seasonal to interannual, *e.g.,* Lathuilière et al., 2008). The in situ observations we present reveal the complexity and variability of the upwelling structure and functioning, owing to synoptic wind variability, mesoscale effects and possibly mixing due to superinertial wave activity. The manifestations of mesoscale turbulence involve preferential and persistent patterns that connect the shelf and open ocean environment and impact the shelf upwelling dynamics.

Superinertial wave activity also seems important to the upwelling sector functioning. Our study provides strong indications that internal tides and non linear internal gravity waves can play a systemic role in the SSUC through water mass transformation and vertical flux of properties. In sustained upwelling conditions where most of the subsurface water feeding the coastal divergence enters the shelf area in the northern SSUC and subsequently flows southward (Ndoye et al., manuscript in preparation) we expect the stratification to be increasingly impacted by IGWs toward the south (*i.e.,* downstream with respect to the dominant shelf circulation), as we generally observe during UPSEN2-ECOAO. However, residence time scales over the southern Senegal shelf are comparable to those of synoptic variability. Water

property modifications and biogeochemical activity thus take place along complex pathways that integrate the influence of synoptic wind variability, mesoscale and internal tide activity. How much of that complexity needs to be accounted for to properly understand the ecological functioning of the SSUC (*e.g.,* as a small pelagic nursery) and its long-term evolution will be the subject of future reseach (see perspectives in Sec. 3.3).

3.2.5 Model studies of the Southern Senegal Upwelling Center

P. Estrade, S. Ndoye and I are developing a ROMS configuration making use of the AGRIF nesting capability. A SST field for the 2^{nd} grid level is shown in Fig. 3.9. The 2nd level covers the entire Senegal domain at two 2 km horizontal resolution. It is the support of the PhD work of S. Ndoye on the subinertial functioning of the SSUC.

Pieces of the dynamical puzzle have started to accumulate and will be put together in a manuscript to be written in 2015. The model is able to reproduce the cross-shore zonation of the SSUC (see Fig. 3.9) and to some extent its climatological fluctuations. In particular, upwelling is displaced offshore a couple months after the beginning of the upwelling season. Despite good model skills at representing the key SSUC SST patterns (including mesoscale features) some model biases remain to be eliminated. Temperature gradient intensity is currently being quantified in the model and it appears to be larger than in the MODIS high resolution SSTs. One possible reason would be that, as developed in the previous section internal gravity wave mixing has a significant effect on the thermohaline structure over the shelf, including frontal intensity.

3.3 Perspectives

The SSUC investigations I am currently conducting or supervising will be remain an essential component of my research for the years to come. They combine the analysis of in situ observations, satellite observations, and regional/fine-scale modeling activities. In the near-future a key objective will be to strengthen synergies between these axes by bridging the gap between the scales and processes resolved by

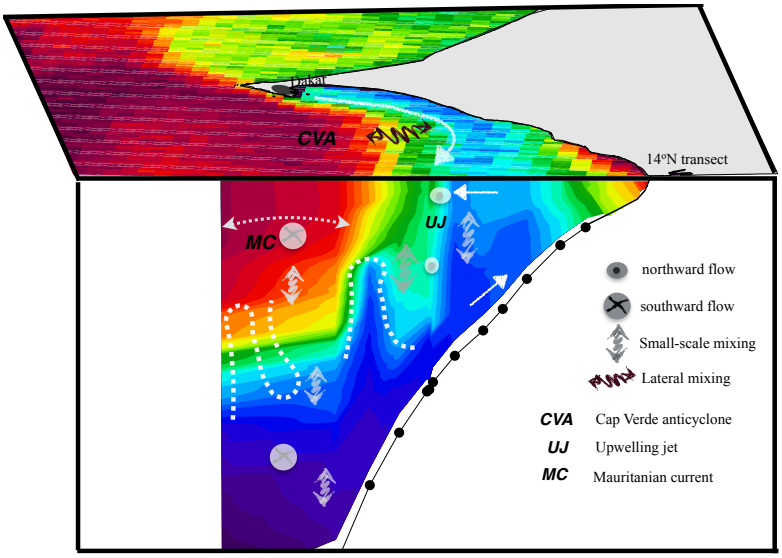

Figure 3.8: 3D schematic description of the upwelling dynamical and hydrological structure over the southern Senegal shelf, as observed during UPSEN2-ECOAO. The manifestation of upwelling takes the form of a cold SST tongue situated tens of kilometers away the shore. Its position and that of its offshore frontal edge are subjected to displacements that can be related to nearshore extensions of mesoscale disturbances. These mesoscale disturbances presumably arise from instabilities of the current system composed of the poleward flowing Mauritanian current and the equatorward upwelling currents. Ubiquitous internal gravity waves over the shelf are presumably implicated in substantial water mass transformation (and associated vertical fluxes of properties) that occur offshore of the upwelling zone. In particular interior mixing is frequently observed just offshore of the upwelling zone. Inshore of that zone, the classical 2D Ekman cell (onshore flow near the bottom, offshore flow in the surface layer) prevails. Therefore, the position of the upwelling zone may not solely result from the shutdown of the cross-shore Ekman driven circulation on its inshore flanck. Partial evidences suggest that IGW breaking may contribute to the offshore migration of the front in UPSEN2-ECOAO type situations. We hypothesize that the sharpness of the front separating upwelling and offshore waters is primarily controlled by IGW mixing in the front area as opposed to submesoscale frontal instabilities (which have no evident signature in high-resolution SST images).

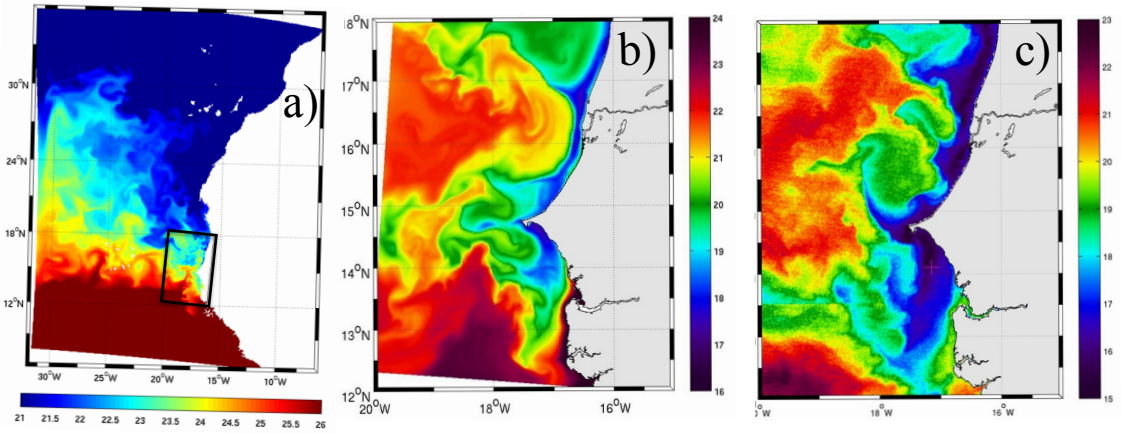

Figure 3.9: a-b) Instantaneous SST field from the $\Delta x = 10$ km (a) Northeastern Atlantic and $\Delta x = 2$ km (b) Senegal embedded grids. The black rectangle in panel a) delineates the Senegal grid extension. The model is able to produce a realistic southern Senegal upwelling center with a seasonal cycle resembling the observations and similar mesoscale patterns (compare with the MODIS SST image for 20 January 2009 (panel c). The dynamical balance and associated transport pathways in the model SSUC are currently being analysed. Courtesy S. Ndoye.

the modeling work ($\Delta x = 2$ km ; PE hydrostatic equations) and those that appear to play an important role based on in situ observations. Perhaps most importantly, the observations of the internal wave field during UPSEN2 (and the possibility that IGWs play a systemic role in its dynamical and biogeochemical functioning) raise a number of questions that will unlikely be answered without explicitely modeling the internal wave field and at least some of its interactions with the subinertial flow. This would require non-hydrostatic simulations.

Other perspectives laid out in section 2.7 would also strongly benefit from non-hydrostatic simulations. Indeed, although primitive equations models may remain the backbone of my research on open ocean turbulence the limitations of this framework for the study of weakly stratified frontal environments are quite clear: non-hydrostatic effects can introduce subtle but important modifications of the ocean dynamics (Magaldi and Haine, 2015; Bachman and Taylor, 2014). Furthermore, they are needed to establish the standards against which to evaluate models at lower resolution, even submesoscale-permitting ones.

Under the guidance of F. Auclair (Laboratoire d'Aérologie) and with the good will of several colleagues of COMODO (http://indi.imag.fr/wordpress/) a compressible

non-boussinesq model is under development that should satisfy these needs and those of the community. I intend to continue contributing to this effort in the coming years.

There are many fascinating marine enigmas remaining for oceanographers to explore. Among them one that has attracted my attention concerns the ways fine-scale dynamics[3] impacts, sometimes in profound ways, trophic interactions. Fine-scale oceanic motions impact the nutrient input and availibilty in the euphotic layer in many ways (Sharples et al., 2007; Bassin et al., 2005; Lathuilière et al., 2010; Lucas et al., 2011a,b; Tweddle et al., 2013; Lucas et al., 2014; Hernández-Carrasco et al., 2014; Capet et al., 2015b). As a result they have an overall bottom-up effect on the entire food chain. Also fine-scale processes can aggregate passive or slow-moving organisms, thereby providing potential fine-scale hotspots for their predators (Benoit-Bird and McManus, 2012; Nordstrom et al., 2013). Processes responsible for the aggregation can be of different nature. On the vertical hotspots often have scales of several meters or less, in which case they are termed "thin layers" (Franks, 1995; Durham et al., 2009). Thin layers are ubiquitous in the coastal ocean.
Indications that frontal regions about mesoscale eddies and submesoscale features are preferentially targeted by marine predators at different trophic levels are accumulating (Weimerskirch et al., 2004; Kai et al., 2009; Dragon et al., 2010; Nordstrom et al., 2013; Prants et al., 2014; Powell and Ohman, 2014; Sabarros et al., 2014),**(Bertrand et al., 2014)**[4] but the underlying processes still need clarification. Enrichment and/or accumulation of food by front lines or internal waves on horizontal scales from tens of meters to a few kilometers are two among several possible reasons (De Monte et al., 2012). Other mechanisms include disruption of the habitat distribution, *e.g.,* when fine-scale motions provoke vertical displacements of the oxycline **(Bertrand et al., 2014)**.

The UPSEN2 experiment has revealed circumstantial evidences that the internal gravity wave field exerts some influence on organisms distribution. A tantalizing perspective would be to explore observationally the trophic interactions in the SSUC and how they are affected by fine-scale dynamics. This would be done while carefully monitoring the physical and biogeochemical environment in which these

[3]In these perspective section "fine-scale" refers to submeso and smaller scales so that fine scale processes encompass, subinertial frontal processes discussed in Chapter 2 but also near-inertial and internal gravity wave activity, *e.g.,* as observed in the SSUC and over many other continental shelves.

[4]Counterexamples also exist, *e.g.,* see Scales et al. (2014).

interactions take place. Relatively slow currents and long residence times over the southern Senegal continental shelf would reduce the difficulties of conducting such an experiment, in comparison to other more dispersive upwelling sectors. With E. Machu and several AWA colleagues we will actively keep seeking fundings to carry out these experiments.

Chapter 4

Conclusion

Résumer, sélectionner, replacer dans son contexte, et tenter de regarder d'un oeil critique 15 ans de mon activité de recherche n'a pas été facile. Cela s'est finalement étalé sur plusieurs années. Toujours quelque chose à finir qui donnerait plus de sens et de cohérence à un parcours un peu éparpillé, thématiquement et surtout géographiquement. Cet éparpillement n'est pas seulement la conséquence de pas mal d'années de vagabondage postdoctoral. Il reflète également un intérêt profond pour l'abondante variété des processus dynamiques qui agitent l'océan. Il est possible que cette abondance ne cesse de m'émerveiller et que je n'apprenne pas á résister au sirènes d'une belle étude de processus, surtout lorsqu'elle se fait en bonne compagnie.

Tant pis donc pour la belle cohérence de mes activités passées. Peut-être une cohérence plus fondamentale est elle en gestation autour des processus qui structurent le fonctionnement de l'océan. En attendant, ce manuscrit comble les trous en prenant la forme d'une revue de l'état de l'art, forme qui j'espère n'aura pas rebuté mes quelques lecteurs. Malgré ou peut-être du fait de sa relative exhaustivité, cette revue aura été une bonne occasion de me demander ce que je désire **vraiment** comprendre du fonctionnement de l'océan dans les années qui viennent. Exercice sûrement salutaire dans une époque qui n'est pas à la rêverie scientifique.

Mon océan de travail a été pendant longtemps numérique. Les campagnes en mer UPSEN1-2 et AWA m'ont donné un petit bout d'océan réel à observer. Et des collègues sénégalais et français passionnés avec qui poser des questions fondamentales mêlant les disciplines et dont les applications sociales sont parmi les plus évidentes. Au Sénégal, l'océan côtier occupe et nourrit les humains. Il façonne aussi leur culture. Les fragilités, robustesses et niveaux de resilience de l'écosystème vis-à-vis des stress qu'il subit sont loin d'être cernés. Les éléments les plus simples du fonctionnement actuel de l'écosystème, par exemple son cycle annuel, sont eux même très mal connus. Le programme AWA a pour principale ambition scientifique de mieux relier les différents maillons de l'environnement marin Ouest-Africain, avec pour finalité une meilleure gestion de la ressource halieutique (petits pélagiques essen-

tiellement). Il n'est bien sur pas question d'obtenir en quelques années le niveau de compréhension atteint pour certaines zones clés du courant de Californie ou d'autres secteurs historiquement très observés. Mais cet océan côtier sénégalais est un environnement original propice à l'étude de processus marins complexes et notamment des couplages physique-biogéochimie-écosystème. Il est aussi un objet scientifique merveilleux pour la formation d'une génération de jeunes chercheurs africains consciente de l'importance de surveiller et préserver leur milieu marin nourricier.

Les études initiées depuis quelques années commencent à livrer des réponses, et avec elles de nombreuses nouvelles questions. Le domaine marin ouest africain occupera sans doute une part importante de mon activité scientifique dans les années qui viennent. Fidèle au principe de ne pas tout miser sur la cohérence, mais tenté de ne pas faire de trop grand écart, il me semble que ce volet de recherche local sera bien complété par l'étude de processus fine-échelle concernant de plus grandes étendues d'océan. Les processus de mélange et d'échanges verticaux dans l'océan global offrent une vaste gamme de problèmes. Dans ce manuscrit je propose de mettre l'accent sur les échanges verticaux dans l'océan des moyennes et hautes latitudes, en lien notamment avec les questions de flux de chaleur et de carbone entre la proche-surface et l'océan intérieur. Tout ceci devrait me tenir bien occupé scientifiquement.

Bibliography

Alford, M. H., A. Y. Shcherbina, and M. C. Gregg, 2013: Observations of near-inertial internal gravity waves radiating from a frontal jet. *J. Phys. Oceanogr.*, **43**, 1225–1239. (Cited on page 48.)

Allen, J. and D. Smeed, 1996: Potential vorticity and vertical velocity at the iceland-faeroes front. *J. Phys. Oceanogr.*, **26**, 2611–2634. (Cited on pages 28 and 30.)

Allen, J., D. Smeed, J. Tintoré, and S. Ruiz, 2001: Mesoscale subduction at the almeria–oran front: Part 1: Ageostrophic flow. *J. Mar. Sys.*, **30**, 263–285. (Cited on pages 28 and 30.)

Aoki, S. and K. Akitomo, 2007: Observations of small-scale disturbances of the Subantarctic Front south of Australia. *Deep Sea Res.*, **54**, 320–339. (Cited on page 38.)

Arbic, B. K., K. L. Polzin, R. B. Scott, J. G. Richman, and J. F. Shriver, 2013: On eddy viscosity, energy cascades, and the horizontal resolution of gridded satellite altimeter products. *J. Phys. Oceanogr.*, **43**, 283–300. (Cited on page 41.)

Arístegui, J., et al., 2009: Sub-regional ecosystem variability in the canary current upwelling. *Prog. Oceanog.*, **83**, 33–48. (Cited on page 58.)

Ascani, F., K. Richards, F. E., S. Grant, K. Johnson, Y. Jia, R. Lukas, and D. Karl, 2013: Physical and biological controls of nitrate concentrations in the upper subtropical North Pacific Ocean. *Deep Sea Res., Part II*, **93**, 119–134. (Cited on page 32.)

Avicola, G., J. N. Moum, A. Perlin, and M. D. Levine, 2007: Enhanced turbulence due to the superposition of internal gravity waves and a coastal upwelling jet. *J. Geophys. Res.*, **112 (C6)**. (Cited on page 71.)

Bachman, S. and J. Taylor, 2014: Modelling of partially-resolved oceanic symmetric instability. *Ocean Model.*, **82**, 15–27. (Cited on pages 48, 49 and 75.)

Barkan, R., K. B. Winters, and S. G. Llewellyn Smith, 2015: Energy cascades and loss of balance in a reentrant channel forced by wind stress and buoyancy fluxes. *J. Phys. Oceanogr.*, **45**, 272–293. (Cited on pages 41, 43 and 46.)

Bartello, P., 2000: Using low-resolution winds to deduce fine structure in tracers. *Atm. Ocean.*, **38**, 303–320. (Cited on page 17.)

Barth, J. A., T. J. Cowles, P. M. Kosro, R. K. Shearman, A. Huyer, and R. L. Smith, 2002: Injection of carbon from the shelf to offshore beneath the euphotic zone in the california current. *J. Geophys. Res.*, **107**, 10–1. (Cited on pages 32 and 62.)

Barton, E., 1989: The poleward undercurrent on the eastern boundary of the subtropical North Atlantic. *Poleward Flows Along Eastern Ocean Boundaries*, Springer, 82–95. (Cited on page 58.)

Barton, E. D., 1998: Eastern boundary of the north atlantic: northwest africa and iberia. coastal segment (18, e). *The sea*, **11**, 633–657. (Cited on page 58.)

Barton, E. D., J. Arístegui, P. Tett, and E. Navarro-Pérez, 2004: Variability in the canary islands area of filament-eddy exchanges. *Prog. Oceanog.*, **62 (2)**, 71–94. (Cited on page 62.)

Barton, E. D., A. Huyer, and R. L. Smith, 1977: Temporal variation observed in the hydrographic regime near Cabo Corveiro in the northwest African upwelling region, February to April 1974. *Deep Sea Res.*, **24 (1)**, 7–23. (Cited on page 60.)

Bassin, C. J., L. Washburn, M. Brzezinski, and E. McPhee-Shaw, 2005: Sub-mesoscale coastal eddies observed by high frequency radar: A new mechanism for delivering nutrients to kelp forests in the Southern California Bight. *Geophys. Res. Lett.*, **32**. (Cited on pages 21 and 76.)

Batteen, M., 1997: Wind-forced modeling studies of currents, meanders and eddies in the California Current System. *J. Geophys. Res.*, **28**, 2199–2221. (Cited on pages 2 and 52.)

Benazzouz, A., S. Mordane, A. Orbi, M. Chagdali, K. Hilmi, A. Atillah, J. L. Pelegrí, and D. Hervé, 2014: An improved coastal upwelling index from sea surface temperature using satellite-based approach - The case of the Canary Current upwelling system . *Cont. Shelf Res.*, **81**, 38 – 54. (Cited on page 57.)

Benítez-Barrios, V., J. L. Pelegrí, A. Hernández-Guerra, K. Lwiza, D. Gomis, P. Vélez-Belchí, and S. Hernández-León, 2011: Three-dimensional circulation in the nw africa coastal transition zone. *Prog. Oceanog.*, **91**, 516–533. (Cited on page 28.)

Benoit-Bird, K. J. and M. A. McManus, 2012: Bottom-up regulation of a pelagic community through spatial aggregations. *Biology letters*, **8**, 813–816. (Cited on page 76.)

Bertrand, A., et al., 2014: Broad impacts of fine-scale dynamics on seascape structure from zooplankton to seabirds. *Nat. Commun.*, **5**. (Cited on page 76.)

Bleck, R., R. Onken, and J. Woods, 1988: A two-dimensional model of mesoscale frontogenesis in the ocean. *Quart. J. Roy. Meteor. Soc.*, **114**, 347–371. (Cited on page 28.)

Blumen, W., 1978: Uniform potential vorticity flow: Part I. Theory of wave interactions and two-dimensional turbulence. *J. Atmos. Sci.*, **35**, 774–783. (Cited on page 22.)

Boccaletti, G., R. Ferrari, and B. Fox-Kemper, 2007: Mixed layer instabilities and restratification. *J. Phys. Oceanogr.*, 2228–2250. (Cited on pages 12, 13 and 17.)

Boé, J., A. Hall, F. Colas, J. C. McWilliams, X. Qu, J. Kurian, and S. B. Kapnick, 2011: What shapes mesoscale wind anomalies in coastal upwelling zones? *Clim. Dyn.*, **36**, 2037–2049. (Cited on page 56.)

Bograd, S. J., et al., 2015: Changes in source waters to the Southern California Bight. *Deep Sea Res.*, **112**, 42–52. (Cited on page 52.)

Bretherton, F. P., 1966: Critical layer instability in baroclinic flows. *Quart. J. Roy. Meteor. Soc.*, **92**, 325–334. (Cited on page 23.)

Bryan, K., J. Dukowicz, and R. Smith, 1999: On the mixing coefficient in the parameterization of bolus velocity. *J. Phys. Oceanogr.*, **29**, 2442–2456. (Cited on page 54.)

Burls, N. and C. Reason, 2008: Modelling the sensitivity of coastal winds over the Southern Benguela upwelling system to different SST forcing. *J. Mar. Sys.*, **74**, 561–584. (Cited on page 56.)

Callies, J. and R. Ferrari, 2013: Interpreting energy and tracer spectra of upper-ocean turbulence in the submesoscale range (1–200 km). *J. Phys. Oceanogr.*, **43**, 2456–2474. (Cited on page 15.)

Capet, X., E. J. Campos, and A. M. Paiva, 2008a: Submesoscale activity over the Argentinian shelf. *Geophys. Res. Lett.*, **35**, L15 605. (Cited on pages 3, 12, 17, 19, 20 and 21.)

Capet, X. and X. Carton, 2004: Nonlinear regimes of baroclinic boundary currents. *J. Phys. Oceanogr.*, **34**, 1400–1409. (Cited on page 5.)

Capet, X., L. Chérubin, and Y. Morel, 2002: Influence of the transport on the instability of a boundary current. *J. Phys. Oceanogr.*, **32**, 2806–2815. (Cited on page 5.)

Capet, X., F. Colas, P. Penven, P. Marchesiello, and J. C. McWilliams, 2008b: Eddies in eastern-boundary subtropical upwelling systems. *Ocean Modeling in an Eddying Regime*, M. Hecht and H. Hasumi, Eds., Am. Geophys. Union, Geophys. Monog. Ser., Vol. 177. (Cited on pages 3, 5, 12, 18, 52 and 54.)

Capet, X., P. Klein, B. L. Hua, G. Lapeyre, and J. C. McWilliams, 2008c: Surface kinetic energy transfer in surface quasi-geostrophic flows. *J. Fluid Mech.*, **604**, 165–174. (Cited on pages 5 and 41.)

Capet, X., P. Marchesiello, and J. C. McWilliams, 2004: Upwelling response to coastal wind profiles. *Geophys. Res. Lett.*, **31**, L13 311. (Cited on pages 3, 5, 54, 56 and 69.)

Capet, X., J. McWilliams, M. Molemaker, and A. Shchepetkin, 2008d: Mesoscale to submesoscale transition in the california current system. part iii: Energy balance and flux. *J. Phys. Oceanogr.*, **38**, 2256–2269. (Cited on pages 3, 12, 13, 15, 16, 41, 42, 43, 44 and 45.)

Capet, X., J. C. McWilliams, M. J. Molemaker, and A. Shchepetkin, 2008e: Mesoscale to submesoscale transition in the California Current System. part i: Flow structure and eddy flux. *J. Phys. Oceanogr.*, **38**, 29–43. (Cited on pages 3, 5, 12, 13, 14, 31 and 72.)

Capet, X., J. C. McWilliams, M. J. Molemaker, and A. Shchepetkin, 2008f: Mesoscale to submesoscale transition in the California Current System. part ii: Frontal processes. *J. Phys. Oceanogr.*, **38**, 44–64. (Cited on pages 3, 12, 13, 31, 33 and 37.)

Capet, X., G. Roullet, P. Klein, and G. Maze, 2015a: Intensification of upper ocean quasi-balanced turbulence through Charney instability. *Ocean Sci.*, submitted. (Cited on pages 5, 27, 34, 42 and 43.)

Capet, X., et al., 2015b: SST patterns and dynamics of the southern Senegal-Gambia upwelling center. *J. Geophys. Res.*, submitted. (Cited on pages 4, 64, 71 and 76.)

Carr, S., X. Capet, J. C. McWilliams, T. Pennington, and F. Chavez, 2008: The influence of diel vertical migration on zooplankton transport and recruitment in an upwelling region. *Fisheries Oceanogr.*, **17**, 1–15. (Cited on page 3.)

Charney, J. G., 1971: Geostrophic turbulence. *J. Atmos. Sci.*, **28**, 1087–1095. (Cited on page 22.)

Charney, J. G. and M. E. Stern, 1962: On the stability of internal baroclinic jets in a rotating atmosphere. *J. Atmos. Sci.*, **19**, 159–172. (Cited on page 26.)

Chavanne, C., P. Flament, and K.-W. Gurgel, 2010: Interactions between a submesoscale anticyclonic vortex and a front*. *J. Phys. Oceanogr.*, **40 (8)**, 1802–1818. (Cited on page 15.)

Chenillat, F., P. Rivière, X. Capet, P. J. Franks, and B. Blanke, 2013: California coastal upwelling onset variability: Cross-shore and bottom-up propagation in the planktonic ecosystem. *PloS One*, **8**, e62 281. (Cited on page 53.)

Citeau, J., L. Finaud, J. Cammas, and H. Demarcq, 1989: Questions relative to ITCZ migrations over the tropical Atlantic Ocean, sea surface temperature and Senegal River runoff. *Met. Atmos. Phys.*, **41**, 181–190. (Cited on page 58.)

Colas, F., X. Capet, J. C. McWilliams, and Z. Li, 2013: Mesoscale eddy buoyancy flux and eddy-induced circulation in eastern boundary currents. *J. Phys. Oceanogr.*, **43**, 1073–1095. (Cited on pages 3, 5, 17, 53 and 55.)

Colas, F., X. Capet, J. C. McWilliams, and A. Shchepetkin, 2008: 1997-98 El Nino off Peru: a numerical study. *Prog. Oceanog.*, **79**, 138–155. (Cited on page 3.)

Colas, F., J. C. McWilliams, X. Capet, and J. Kurian, 2012: Heat Balance and Eddies in the Peru-Chile Current System. *Clim. Dyn.*, **39**, 509–529. (Cited on pages 3, 53 and 54.)

Cole, S. T., D. L. Rudnick, and J. A. Colosi, 2010: Seasonal evolution of upper-ocean horizontal structure and the remnant mixed layer. *Journal of Geophysical Research: Oceans (1978–2012)*, **115 (C4)**. (Cited on page 15.)

Cropper, T. E., E. Hanna, and G. R. Bigg, 2014: Spatial and temporal seasonal trends in coastal upwelling off Northwest Africa, 1981–2012. *Deep Sea Res.*, **86**, 94–111. (Cited on page 57.)

Dadou, I., V. Garçon, V. Andersen, G. Flierl, and C. Davis, 1996: Impact of the North Equatorial Current meandering on a pelagic ecosystem: a modeling approach. *J. Mar. Res.*, **54**, 311–342. (Cited on page 2.)

D'Asaro, E., C. Lee, l. Rainville, R. Harcourt, and L. Thomas, 2011: Enhanced turbulence and energy dissipation at ocean fronts. *Science*, **15**, 318–322. (Cited on page 44.)

de Lavergne, C., G. Madec, J. Le Sommer, N. G, and N. Naveira Garabato, 2015: On Antarctic Bottom Water consumption in the abyssal ocean. *J. Phys. Oceanogr.*, in revision. (Cited on page 3.)

De Monte, S., C. Cotté, F. d'Ovidio, M. Lévy, M. Le Corre, and H. Weimerskirch, 2012: Frigatebird behaviour at the ocean–atmosphere interface: integrating animal behaviour with multi-satellite data. *Journal of The Royal Society Interface*, **9**, 3351–3358. (Cited on page 76.)

Demarcq, H. and V. Faure, 2000: Coastal upwelling and associated retention indices derived from satellite sst. application to octopus vulgaris recruitment. *Oceanolo. Acta*, **23**, 391 – 408. (Cited on page 57.)

Denis, B., J. Côté, and R. Laprise, 2002: Spectral decomposition of two-dimensional atmospheric fields on limited-area domains using the discrete cosine transform (DCT). *Mon. Wea. Rev.*, **130**, 1812–1829. (Cited on page 40.)

Dragon, A.-C., P. Monestiez, A. Bar-Hen, and C. Guinet, 2010: Linking foraging behaviour to physical oceanographic structures: southern elephant seals and mesoscale eddies east of kerguelen islands. *Prog. Oceanog.*, **87**, 61–71. (Cited on page 76.)

Duarte, R., X. Carton, X. Capet, and L. Chérubin, 2011: Trapped instability and vortex formation by an unstable coastal current. *Regul. Chaotic Dyn.*, **16**, 577–601. (Cited on page 5.)

Dufois, F., P. Penven, C. P. Whittle, and J. Veitch, 2012: On the warm nearshore bias in Pathfinder monthly SST products over Eastern Boundary Upwelling Systems. *Ocean Model.*, **47**, 113–118. (Cited on page 64.)

Durham, W. M., J. O. Kessler, and R. Stocker, 2009: Disruption of vertical motility by shear triggers formation of thin phytoplankton layers. *science*, **323**, 1067–1070. (Cited on page 76.)

Eden, C., L. Czeschel, and D. Olbers, 2014: Toward energetically consistent ocean models. *J. Phys. Oceanogr.*, **44**, 3160–3184. (Cited on page 43.)

Elliott, B. and T. Sanford, 1986: The subthermocline lens d1. part i: Description of water properties and velocity profiles. *J. Phys. Oceanogr.*, **16**, 532–548. (Cited on page 10.)

Espinoza-González, O., F. Figueiras, B. Crespo, I. Teixeira, and C. Castro, 2012: Autotrophic and heterotrophic microbial plankton biomass in the NW Iberian upwelling: seasonal assessment of metabolic balance. *Aquatic microbial ecology*, **67**, 77–89. (Cited on page 57.)

Estrade, P., P. Marchesiello, A. Colin de Verdière, and C. Roy, 2008: Cross-shelf structure of coastal upwelling: A two-dimensional extension of Ekman's theory and a mechanism for inner shelf upwelling shut down. *J. Mar. Res.*, **66 (5)**, 589–616. (Cited on pages 67 and 68.)

Flament, P., L. Armi, and L. Washburn, 1985: The evolving structure of an upwelling filament. *J. Geophys. Res.*, **90**, 11 765–11 778. (Cited on page 11.)

Fox-Kemper, B. and R. Ferrari, 2008: Parameterization of mixed layer eddies. II: Prognosis and impact. *J. Phys. Oceanogr.*, **38**, 1166–1179. (Cited on pages 12 and 45.)

Fox-Kemper, B., R. Ferrari, and R. Hallberg, 2008: Parameterization of mixed layer eddies. I: Theory and diagnosis. *J. Phys. Oceanogr.*, **38**, 1145–1165. (Cited on pages 12, 13, 17, 19, 31 and 43.)

Fox-Kemper, B., et al., 2011: Parameterization of mixed layer eddies. iii: Implementation and impact in global ocean climate simulations. *Ocean Model.*, **39**, 61–78. (Cited on pages 31 and 48.)

Franks, P. J., 1995: Thin layers of phytoplankton: A model of formation by near-inertial wave shear. *Deep Sea Res.*, **42**, 75–91. (Cited on page 76.)

Fu, l. L. and R. Ferrari, 2008: Observing oceanic submesoscale processes from space. *Eos Trans. AGU*, **89**, 488. (Cited on page 49.)

Garabato, A. C. N., H. Leach, J. T. Allen, R. T. Pollard, and V. H. Strass, 2001: Mesoscale subduction at the antarctic polar front driven by baroclinic instability. *J. Phys. Oceanogr.*, **31**, 2087–2107. (Cited on page 28.)

Garabato, A. C. N., V. H. Strass, and G. Kattner, 2002: Fluxes of nutrients in a three-dimensional meander structure of the Antarctic Polar Front. *Deep Sea Res.*, **49**, 3771–3792. (Cited on page 38.)

Gent, P. R. and J. C. McWilliams, 1990: Isopycnal mixing in ocean circulation models. *J. Phys. Oceanogr.*, **20**, 150–155. (Cited on page 2.)

Gent, P. R., J. Willebrand, T. J. McDougall, and J. C. McWilliams, 1995: Parameterizing eddy-induced tracer transports in ocean circulation models. *J. Phys. Oceanogr.*, **25**, 463–474. (Cited on page 2.)

Gil, J. and D. Gomis, 2008: The secondary ageostrophic circulation in the iberian poleward current along the cantabrian sea (bay of biscay). *J. Mar. Sys.*, **74**, 60–73. (Cited on page 28.)

Giordani, H., L. Prieur, and G. Caniaux, 2006: Advanced insights into sources of vertical velocity in the ocean. *Ocean Dynam.*, **56**, 513–524. (Cited on pages 29 and 30.)

Gomis, D. and M. A. Pedder, 2005: Errors in dynamical fields inferred from oceanographic cruise data: Part i. the impact of observation errors and the sampling distribution. *J. Mar. Sys.*, **56**, 317–333. (Cited on page 30.)

Grisouard, N. and L. N. Thomas, 2015: Critical and near-critical reflections of near-inertial waves off the sea surface at ocean fronts. *J. Fluid Mech.*, **765**, 273–302. (Cited on page 48.)

Grodsky, S. A., J. A. Carton, S. Nigam, and Y. M. Okumura, 2012: Tropical atlantic biases in ccsm4. *J. Clim.*, **25**, 3684–3701. (Cited on page 52.)

Gruber, N., Z. Lachkar, H. Frenzel, P. Marchesiello, M. Münnich, J. C. McWilliams, T. Nagai, and G.-K. Plattner, 2011: Eddy-induced reduction of biological production in eastern boundary upwelling systems. *Nat. Geophys.*, **4**, 787–792. (Cited on pages 32, 53 and 62.)

Gruber, N., et al., 2006: Eddy-resolving simulation of plankton ecosystem dynamics in the california current system. *Deep Sea Res.*, **53**, 1483–1516. (Cited on page 53.)

Gurova, E. and B. Chubarenko, 2012: Remote-sensing observations of coastal submesoscale eddies in the south-eastern baltic. *Oceanologia*, **54**, 631–654. (Cited on page 21.)

Haine, T. W. N. and J. Marshall, 1998: Gravitational, symmetric, and baroclinic instability of the ocean mixed layer. *J. Phys. Oceanogr.*, **28**, 634–658. (Cited on pages 34 and 37.)

Hamilton, P., K. Donohue, R. Leben, A. Lugo-Fernández, and R. Green, 2011: Loop current observations during spring and summer of 2010: Description and historical perspective. *Monitoring and Modeling the Deepwater Horizon Oil Spill: A Record-Breaking Enterprise, Geophys. Monogr. Ser*, **195**, 117–130. (Cited on page 2.)

Hamlington, P. E., L. P. Van Roekel, B. Fox-Kemper, K. Julien, and G. P. Chini, 2014: Langmuir–submesoscale interactions: Descriptive analysis of multiscale frontal spindown simulations. *J. Phys. Oceanogr.*, **44**, 2249–2272. (Cited on page 44.)

Hernández-Carrasco, I., V. Rossi, E. Hernández-García, V. Garçon, and C. López, 2014: The reduction of plankton biomass induced by mesoscale stirring: A modeling study in the benguela upwelling. *Deep Sea Res.*, **83**, 65–80. (Cited on pages 62 and 76.)

Hosegood, P., M. Gregg, and M. Alford, 2013: Wind-driven submesoscale subduction at the north pacific subtropical front. *J. Geophys. Res.*, **118**, 5333–5352. (Cited on page 37.)

Hoskins, B., 1982: The mathematical theory of frontogenesis. *Annu. Rev. Fluid Mech.*, **14**, 131–151. (Cited on pages 11 and 28.)

Hoskins, B., I. Draghici, and H. Davies, 1978: A new look at the ω-equation. *Quart. J. Roy. Meteor. Soc.*, **104**, 31–38. (Cited on page 28.)

Isern-Fontanet, J., B. Chapron, G. Lapeyre, and P. Klein, 2006: Potential use of microwave sea surface temperature for the estimation of oceanic currents. *Geophys. Res. Lett.*, **33**, L24 608. (Cited on page 24.)

Ito, T. and J. Marshall, 2008: Control of lower-limb overturning circulation in the southern ocean by diapycnal mixing and mesoscale eddy transfer. *J. Phys. Oceanogr.*, **38 (12)**, 2832–2845. (Cited on page 3.)

Jacox, M. and C. Edwards, 2012: Upwelling source depth in the presence of nearshore wind stress curl. *J. Geophys. Res.*, **117**. (Cited on page 56.)

Jin, X., C. Dong, J. Kurian, J. C. McWilliams, D. B. Chelton, and Z. Li, 2009: SST-wind interaction in coastal upwelling: Oceanic simulation with empirical coupling. *J. Phys. Oceanogr.*, **39**, 2957–2970. (Cited on page 56.)

Johnston, T., D. L. Rudnick, and E. Pallàs-Sanz, 2011: Elevated mixing at a front. *J. Geophys. Res.*, **116**. (Cited on pages 15 and 44.)

Jouanno, J., X. Capet, G. Madec, P. Klein, and S. Masson, 2015: Dissipation of the energy imparted by mid-latitude storms in the Southern Ocean. *J. Phys. Oceanogr.*, submitted. (Cited on pages 4, 5, 45, 47 and 48.)

Kai, E. T., V. Rossi, J. Sudre, H. Weimerskirch, C. Lopez, E. Hernandez-Garcia, F. Marsac, and V. Garçon, 2009: Top marine predators track lagrangian coherent structures. *Proc. Natl. Acad. Sci. USA*, **106**, 8245–8250. (Cited on page 76.)

Kaneko, H., I. Yasuda, K. Komatsu, and S. Itoh, 2012: Observations of the structure of turbulent mixing across the kuroshio. *Geophys. Res. Lett.*, **39**. (Cited on page 44.)

Kaneko, H., I. Yasuda, K. Komatsu, and S. Itoh, 2013: Observations of vertical turbulent nitrate flux across the kuroshio. *Geophys. Res. Lett.*, **40**, 3123–3127. (Cited on page 38.)

Kara, A. B., A. J. Wallcraft, C. N. Barron, H. E. Hurlburt, and M. Bourassa, 2008: Accuracy of 10 m winds from satellites and NWP products near land-sea boundaries. *J. Geophys. Res.*, **113**. (Cited on page 56.)

Kim, S. Y., et al., 2011: Mapping the us west coast surface circulation: A multiyear analysis of high-frequency radar observations. *J. Geophys. Res.*, **116**. (Cited on pages 15 and 24.)

Klein, P., B. L. Hua, G. Lapeyre, X. Capet, S. Le Gentil, and H. Sasaki, 2008a: Upper ocean turbulence from high-resolution 3D simulations. *J. Phys. Oceanogr.*, **38**, 1748–1763. (Cited on pages 3, 24, 25, 34, 41, 42, 43 and 49.)

Klein, P., B. L. Hua, G. Lapeyre, X. Capet, S. Le Gentil, and H. Sasaki, 2008b: Upper ocean turbulence from high-resolution 3D simulations. *J. Phys. Oceanogr.*, **38**, 1748–1763. (Cited on pages 27 and 45.)

Klein, P., J. Isern-Fontanet, G. Lapeyre, G. Roullet, E. Danioux, B. Chapron, and H. Sasaki, 2009: Diagnosis of mesoscale and submesoscale circulation in the upper ocean from high-resolution sea surface height. *J. Mar. Res.*, submitted. (Cited on page 24.)

Koch, A., A. Kurapov, and J. Allen, 2010: Near-surface dynamics of a separated jet in the coastal transition zone off oregon. *J. Geophys. Res.*, **115**. (Cited on page 15.)

Koszalka, I., A. Bracco, J. C. McWilliams, and A. Provenzale, 2009: Dynamics of wind-forced coherent anticyclones in the open ocean. *J. Geophys. Res.*, **114**. (Cited on pages 15 and 30.)

Kouketsu, S., I. Yasuda, and Y. Hiroe, 2007: Three-dimensional structure of frontal waves and associated salinity minimum formation along the kuroshio extension. *J. Phys. Oceanogr.*, **37**, 644–656. (Cited on page 28.)

Kudela, R. M., et al., 2008: New insights into the controls and mechanisms of plankton productivity along the US West Coast. *Oceanography*, **21**, 46–59. (Cited on page 57.)

Kunze, E., 1985: Near-inertial wave propagation in geostrophic shear. *J. Phys. Oceanogr.*, **15 (5)**, 544–565. (Cited on page 2.)

Kunze, E., 1986: The mean and near-inertial velocity fields in a warm-core ring. *J. Phys. Oceanogr.*, **16**, 1444–1461. (Cited on page 2.)

Kunze, E. and T. B. Sanford, 1996: Abyssal mixing: Where it is not. *J. Phys. Oceanogr.*, **26**, 2286–2296. (Cited on page 2.)

LaCasce, J. H. and A. Mahadevan, 2006: Estimating subsurface horizontal and vertical velocities from sea surface temperature. *J. Mar. Res.*, **64**, 694–721. (Cited on pages 24, 25 and 30.)

Landry, M. R., M. D. Ohman, R. Goericke, M. R. Stukel, and K. Tsyrklevich, 2009: Lagrangian studies of phytoplankton growth and grazing relationships in a coastal upwelling ecosystem off Southern California. *Prog. Oceanog.*, **83**, 208–216. (Cited on page 71.)

Lapeyre, G., 2009a: What mesoscale signal does the altimeter reflect? on the decomposition in baroclinic modes and on a surface-trapped mode. *J. Phys. Oceanogr.*, **39**, 2857–2874. (Cited on page 24.)

Lapeyre, G., 2009b: What mesoscale signal does the altimeter reflect? on the decomposition in baroclinic modes and on a surface-trapped mode. *J. Phys. Oceanogr.*, **39**, 2857–2874. (Cited on page 25.)

Lapeyre, G. and P. Klein, 2006: Dynamics of the upper oceanic layers in terms of surface quasigeostrophy theory. *J. Phys. Oceanogr.*, **36**, 165–176. (Cited on pages 12, 22, 24 and 25.)

Lapeyre, G., P. Klein, and B. Hua, 2006: Oceanic restratification forced by surface frontogenesis. *J. Phys. Oceanogr.*, **36**, 1577–1590. (Cited on page 12.)

Large, W., J. McWilliams, and S. Doney, 1994: Oceanic vertical mixing: A review and a model with a nonlocal boundary layer parameterization. *Rev. Geophys.*, **32**, 363–403. (Cited on page 2.)

Large, W. D. and G. Danabasoglu, 2006: Attributions and impacts of upper-ocean biases in CCSM3. *J. Clim.*, **19**, 2325–2346. (Cited on page 52.)

Lathuilière, C., V. Echevin, and M. Lévy, 2008: Seasonal and intraseasonal surface chlorophyll-a variability along the northwest african coast. *J. Geophys. Res.*, **113**. (Cited on pages 32, 57 and 72.)

Lathuilière, C., V. Echevin, M. Lévy, and G. Madec, 2010: On the role of the mesoscale circulation on an idealized coastal upwelling ecosystem. *J. Geophys. Res.*, **115**. (Cited on pages 53 and 76.)

Le Traon, P. Y., P. Klein, B. L. Hua, and G. Dibarboure, 2008: Do altimeter wavenumber spectra agree with interior or surface quasi-geostrophic theory? *J. Phys. Oceanogr.*, **38**, 1137–1142. (Cited on page 15.)

Leach, H., 1987: The diagnosis of synoptic-scale vertical motion in the seasonal thermocline. *Deep Sea Res.*, **34**, 2005–2017. (Cited on page 28.)

Legal, C., P. Klein, A.-M. Treguier, and J. Paillet, 2007: Diagnosis of the vertical motions in a mesoscale stirring region. *J. Phys. Oceanogr.*, **37**, 1413–1424. (Cited on pages 28 and 30.)

Lemarié, F., L. Debreu, A. Shchepetkin, and J. C. Mcwilliams, 2012: On the stability and accuracy of the harmonic and biharmonic isoneutral mixing operators in ocean models. *Ocean Model.*, **52**, 9–35. (Cited on pages 34 and 36.)

Lentz, S. J., 1992: The surface boundary layer in coastal upwelling regions. *J. Phys. Oceanogr.*, **22**, 1517–1539. (Cited on page 67.)

Lentz, S. J. and D. C. Chapman, 2004: The importance of nonlinear cross-shelf momentum flux during wind-driven coastal upwelling. *J. Phys. Oceanogr.*, **34**, 2444–2457. (Cited on page 71.)

Levy, M., P. Franks, A. P. Martin, and R. P., 2012: Bringing physics to life at the submesoscale. *Geophys. Res. Lett.*, **39**, L14 602. (Cited on page 49.)

Lévy, M., M. Gavart, L. Mémery, G. Caniaux, and A. Paci, 2005: A four-dimensional mesoscale map of the spring bloom in the northeast Atlantic (POMME experiment): Results of a prognostic model. *J. Geophys. Res.*, **110**. (Cited on page 30.)

Levy, M., P. Klein, and A. Treguier, 2001: Impact of sub-mesoscale physics on production and subduction of phytoplankton in an oligotrophic regime. *J. Mar. Res.*, **59**, 535–565. (Cited on pages 10, 31, 32 and 34.)

Lévy, M., P. Klein, A.-M. Tréguier, D. Iovino, G. Madec, S. Masson, and K. Takahashi, 2010: Modifications of gyre circulation by sub-mesoscale physics. *Ocean Model.*, **34**, 1–15. (Cited on page 31.)

Lindstrom, S. S. and D. Pandolph Watts, 1994: Vertical motion in the gulf stream near 68 w. *J. Phys. Oceanogr.*, **24**, 2321–2333. (Cited on page 30.)

Lochte, K. and O. Pfannkuche, 1987: Cyclonic cold-core eddy in the eastern north atlantic. ii. nutients, phytoplankton and bacteriaplankton. *Mar. Ecol. Prog.*, **39**, 153–167. (Cited on page 2.)

Lucas, A. J., C. L. Dupont, V. Tai, J. L. Largier, B. Palenik, and P. J. Franks, 2011a: The green ribbon: multiscale physical control of phytoplankton productivity and community structure over a narrow continental shelf. *Limnol. Oceanogr.*, **56**, 611–626. (Cited on pages 57 and 76.)

Lucas, A. J., P. J. Franks, and C. L. Dupont, 2011b: Horizontal internal-tide fluxes support elevated phytoplankton productivity over the inner continental shelf. *Limnol. Oceanogr. Fluids Environ.*, **1 (1)**, 56–74. (Cited on pages 69 and 76.)

Lucas, A. J., G. C. Pitcher, T. A. Probyn, and R. M. Kudela, 2014: The influence of diurnal winds on phytoplankton dynamics in a coastal upwelling system off southwestern africa. *Deep Sea Res.*, **101**, 50–62. (Cited on pages 57 and 76.)

Lueck, R. and T. Osborn, 1986: The dissipation of kinetic energy in a warm-core ring. *J. Geophys. Res.*, **91**, 803–818. (Cited on page 2.)

Lumpkin, R. and S. Elipot, 2010: Surface drifter pair spreading in the north atlantic. *J. Geophys. Res.*, **115**. (Cited on page 18.)

MacVean, M. and J. Woods, 1980: Redistribution of scalars during upper ocean frontogenesis: a numerical model. *Quart. J. Roy. Meteor. Soc.*, **106**, 293–311. (Cited on page 28.)

Magaldi, M. G. and T. W. Haine, 2015: Hydrostatic and non-hydrostatic simulations of dense waters cascading off a shelf: The east greenland case. *Deep Sea Res.*, **96**, 89–104. (Cited on pages 48 and 75.)

Mahadevan, A., E. D'Asaro, C. Lee, and M. J. Perry, 2012: Eddy-driven stratification initiates north atlantic spring phytoplankton blooms. *Science*, **337**, 54–58. (Cited on pages 38 and 44.)

Mahadevan, A. and A. Tandon, 2006: An analysis of mechanisms for submesoscale vertical motion at ocean fronts. *Ocean Model.*, **14**, 241–256. (Not cited.)

Marchesiello, P., X. Capet, and C. Menkes, 2011: Submesoscale turbulence in Tropical Instability Waves. *Ocean Model.*, **39**, 31–46. (Cited on pages 15, 17, 41, 42 and 43.)

Marchesiello, P. and P. Estrade, 2009: Eddy activity and mixing in upwelling systems: a comparative study of northwest Africa and California regions. *Int. J. Earth Sci.*, **98**, 299–308. (Cited on page 52.)

Marchesiello, P., J. C. McWilliams, and A. Shchepetkin, 2003: Equilibrium structure and dynamics of the California Current System. *J. Phys. Oceanogr.*, **33**, 753–783. (Cited on pages 2, 52 and 53.)

Marshall, J., D. Jamous, and J. Nilsson, 2001: Entry, flux and exit of potential vorticity in ocean circulation. *J. Phys. Oceanogr.*, **31**, 777–789. (Cited on page 35.)

Martin, A. P. and K. J. Richards, 2001: Mechanisms for vertical nutrient transport within a north atlantic mesoscale eddy. *Deep Sea Res.*, **48**, 757–773. (Cited on pages 28 and 30.)

McWilliams, J., 1985: Submesoscale, coherent vortices in the ocean. *Rev. Geophys.*, **23**, 165–182. (Cited on page 10.)

McWilliams, J., M. Molemaker, and I. Yavneh, 2001: From stirring to mixing of momentum: Cascades from balanced flows to dissipation in the oceanic interior. *'Aha Huliko'a Proceedings*, P. Muller, Ed., U. Hawaii, 59–66. (Cited on page 15.)

McWilliams, J. C., F. Colas, and M. J. Molemaker, 2009a: Cold filamentary intensification and oceanic surface convergence lines. *Geophys. Res. Lett.*, **36**, L18 602. (Cited on page 28.)

McWilliams, J. C., M. J. Molemaker, and E. I. Olafsdottir, 2009b: Linear fluctuation growth during frontogenesis. *J. Phys. Oceanogr.*, **39**, 3119–3129. (Cited on page 44.)

Mechoso, C., et al., 2014: Ocean-cloud-atmosphere-land interactions in the Southeastern Pacific: The VOCALS Program. *Bull. Am. Meteorol. Soc.*, **95**, 357–375. (Cited on page 51.)

Melet, A., R. Hallberg, S. Legg, and K. Polzin, 2013: Sensitivity of the ocean state to the vertical distribution of internal-tide-driven mixing. *J. Phys. Oceanogr.*, **43**, 602–615. (Cited on page 3.)

Mensa, J. A., Z. Garraffo, A. Griffa, T. M. Özgökmen, A. Haza, and M. Veneziani, 2013: Seasonality of the submesoscale dynamics in the gulf stream region. *Ocean Dynam.*, **63**, 923–941. (Cited on pages 15 and 21.)

Messié, M. and F. P. Chavez, 2014: Seasonal regulation of primary production in eastern boundary upwelling systems. *Progress in Oceanography*, in press. (Cited on page 57.)

Molemaker, M., J. McWilliams, and X. Capet, 2010: Balanced and unbalanced routes to dissipation in an equilibrated eady flow. *J. Fluid Mech.*, **654**, 35–63. (Cited on pages 15, 27, 41, 43 and 46.)

Molemaker, M., J. McWilliams, and I. Yavneh, 2005: Baroclinic instability and loss of balance. *J. Phys. Oceanogr.*, **35**, 1505–1517. (Cited on pages 15, 39 and 41.)

Molemaker, M. J., J. C. Mc Williams, and W. K. Dewar, 2015: Submesoscale instability and generation of mesoscale anticyclones near a separation of the california undercurrent. *J. Phys. Oceanogr.*, **45**, 613–629. (Cited on page 21.)

Molemaker, M. J. and J. C. McWilliams, 2010: Local balance and cross-scale flux of available potential energy. *J. Fluid Mech.*, **645**, 295–314. (Cited on page 41.)

Montes, I., F. Colas, X. Capet, and W. Schneider, 2010: On the pathways of the equatorial subsurface currents in the eastern equatorial Pacific and their contributions to the Peru-Chile Undercurrent. *J. Geophys. Res.*, **115**. (Cited on page 3.)

Müller, P., J. C. McWilliams, and M. J. Molemaker, 2005: Routes to dissipation in the ocean: The 2D/3D turbulence conundrum. *Marine Turbulence: Theories, Observations and Models*, H. Baumert, J. Simpson, and J. Sundermann, Eds., Cambridge University Press, 397–405. (Cited on pages 39 and 41.)

Munk, W., L. Armi, K. Fischer, and F. Zachariansen, 2000: Spirals on the sea. *Proc. R. Soc. Lond. A*, **456**, 1217–1280. (Cited on pages 11 and 20.)

Nagai, T., A. Tandon, and D. Rudnick, 2006: Two-dimensional ageostrophic secondary circulation at ocean fronts due to vertical mixing and large-scale deformation. *J. Geophys. Res.*, **111**. (Cited on page 29.)

Nagai, T., A. Tandon, H. Yamazaki, and M. J. Doubell, 2009: Evidence of enhanced turbulent dissipation in the frontogenetic Kuroshio Front thermocline. *Geophys. Res. Lett.*, **36**. (Cited on page 44.)

Nagai, T., A. Tandon, H. Yamazaki, M. J. Doubell, and S. Gallager, 2012: Direct observations of microscale turbulence and thermohaline structure in the kuroshio front. *J. Geophys. Res.*, **117**. (Cited on pages 28 and 44.)

Ndoye, S., X. Capet, P. Estrade, B. Sow, D. Dagorne, A. Lazar, A. Gaye, and P. Brehmer, 2014: SST patterns and dynamics of the southern Senegal-Gambia upwelling center. *J. Geophys. Res.*, **119**, 8315–8335. (Cited on pages 61, 62, 63, 64 and 65.)

Nencioli, F., F. d'Ovidio, A. Doglioli, and A. Petrenko, 2013: In situ estimates of submesoscale horizontal eddy diffusivity across an ocean front. *J. Geophys. Res.*, **118**, 7066–7080. (Cited on page 20.)

Nordstrom, C. A., B. C. Battaile, C. Cotte, and A. W. Trites, 2013: Foraging habitats of lactating northern fur seals are structured by thermocline depths and submesoscale fronts in the eastern bering sea. *Deep Sea Res.*, **88**, 78–96. (Cited on page 76.)

Nurser, A. and J. Zhang, 2000: Eddy-induced mixed layer shallowing and mixed layer-thermocline exchange. *J. Geophys. Res.*, **105**, 21 851–21 868. (Cited on page 32.)

Oka, A. and Y. Niwa, 2013: Pacific deep circulation and ventilation controlled by tidal mixing away from the sea bottom. *Nat. comm.*, **4**. (Cited on page 3.)

Özgökmen, T. M., A. C. Poje, P. F. Fischer, H. Childs, H. Krishnan, C. Garth, A. C. Haza, and E. Ryan, 2012: On multi-scale dispersion under the influence of surface mixed layer instabilities and deep flows. *Ocean Model.*, **56**, 16–30. (Cited on page 18.)

Özgökmen, T. M., A. C. Poje, P. F. Fischer, and A. C. Haza, 2011: Large eddy simulations of mixed layer instabilities and sampling strategies. *Ocean Model.*, **39**, 311–331. (Cited on page 18.)

Paci, A., G. Caniaux, M. Gavart, H. Giordani, M. Lévy, L. Prieur, and G. Reverdin, 2005: A high-resolution simulation of the ocean during the POMME experiment: Simulation results and comparison with observations. *J. Geophys. Res.*, **110**. (Cited on page 30.)

Pallàs-Sanz, E., T. Johnston, and D. Rudnick, 2010a: Frontal dynamics in a california current system shallow front: 1. frontal processes and tracer structure. *J. Geophys. Res.*, **115**. (Cited on page 15.)

Pallàs-Sanz, E., T. Johnston, and D. Rudnick, 2010b: Frontal dynamics in a california current system shallow front: 2. mesoscale vertical velocity. *J. Geophys. Res.*, **115**. (Cited on pages 15 and 28.)

Pascual, A., D. Gomis, R. L. Haney, and S. Ruiz, 2004: A quasigeostrophic analysis of a meander in the palamos canyon: Vertical velocity, geopotential tendency, and a relocation technique. *J. Phys. Oceanogr.*, **34**, 2274–2287. (Cited on pages 28 and 30.)

Pedlosky, J., 1987: *Geophysical Fluid Dynamics*. Springer-Verlag, 710 pp. (Cited on page 12.)

Peña-Izquierdo, J., J. L. Pelegrí, M. V. Pastor, P. Castellanos, M. Emelianov, M. Gasser, J. Salvador, and E. Vázquez-Domínguez, 2012: The continental slope current system between Cape Verde and the Canary Islands. *Scien. Mar.*, **76**, 65–78. (Cited on page 58.)

Peters, H., M. C. Gregg, and T. B. Sanford, 1995: On the parameterization of equatorial turbulence: Effect of fine-scale variations below the range of the diurnal cycle. *J. Geophys. Res.*, **100**, 18 333–18 348. (Cited on page 2.)

Pidcock, R., A. Martin, J. Allen, S. C. Painter, and D. Smeed, 2013: The spatial variability of vertical velocity in an iceland basin eddy dipole. *Deep Sea Res.*, **72**, 121–140. (Cited on page 30.)

Pinot, J.-M., J. Tintoré, and D.-P. Wang, 1996: A study of the omega equation for diagnosing vertical motions at ocean fronts. *J. Mar. Res.*, **54**, 239–259. (Cited on pages 29 and 30.)

Pitcher, G., F. Figueiras, B. Hickey, and M. Moita, 2010: The physical oceanography of upwelling systems and the development of harmful algal blooms. *Prog. Oceanog.*, **85 (1)**, 5–32. (Cited on page 57.)

Plattner, G.-K., N. Gruber, H. Frenzel, and J. C. McWilliams, 2005: Decoupling marine export production from new production. *Geophys. Res. Lett.*, **32**. (Cited on page 53.)

Plougonven, R. and C. Snyder, 2007: Inertia-gravity waves spontaneously generated by jets and fronts. Part 1: Different baroclinic life cycles. *J. Atmos. Sci.*, **64**, 2502–2520. (Cited on page 39.)

Poje, A. C., et al., 2014: Submesoscale dispersion in the vicinity of the Deepwater Horizon spill. *Proc. Natl. Acad. Sci. USA*, **111**, 12 693–12 698. (Cited on pages 18 and 21.)

Pollard, R. and L. Regier, 1992: Vorticity and vertical circulation at an ocean front. *J. Phys. Oceanogr.*, **22**, 609–624. (Cited on page 28.)

Ponte, A. L., P. Klein, X. Capet, P.-Y. Le Traon, B. Chapron, and P. Lherminier, 2013: Diagnosing surface mixed layer dynamics from high-resolution satellite observations: Numerical insights. *J. Phys. Oceanogr.*, **43**, 1345–1355. (Cited on pages 25, 29, 34 and 49.)

Powell, J. R. and M. D. Ohman, 2014: Covariability of zooplankton gradients with glider-detected density fronts in the Southern California Current System. *Deep Sea Res.* (Cited on page 76.)

Prants, S., M. Budyansky, and M. Y. Uleysky, 2014: Identifying lagrangian fronts with favourable fishery conditions. *Deep Sea Res.*, **90**, 27–35. (Cited on page 76.)

Qazi, W. A., W. J. Emery, and B. Fox-Kemper, 2014: Computing Ocean Surface Currents Over the Coastal California Current System Using 30-Min-Lag Sequential SAR Images. *Geoscience and Remote Sensing, IEEE Transactions*, **52**, 7559–7580. (Cited on page 15.)

Qiu, B., S. Chen, P. Klein, H. Sasaki, and Y. Sasai, 2014: Seasonal mesoscale and sub-mesoscale eddy variability along the North Pacific Subtropical Countercurrent. *J. Phys. Oceanogr.*, **44 (12)**, 3079–3098. (Cited on pages 34, 41 and 45.)

Ramp, S. R., P. F. Jessen, K. H. Brink, P. P. Niiler, F. L. Daggett, and J. S. Best, 1991: The physical structure of cold filaments near Point Arena, California, during June 1987. *J. Geophys. Res.*, **96**, 14 859–14 883. (Cited on page 62.)

Renault, L., et al., 2012: Upwelling response to atmospheric coastal jets off central Chile: A modeling study of the October 2000 event. *J. Geophys. Res.*, **117**. (Cited on page 56.)

Richter, I., 2015: Climate model biases in the eastern tropical oceans: causes, impacts and ways forward. *Wiley Interdisciplinary Reviews: Climate Change*. (Cited on page 52.)

Rixen, M., J. Allen, R. Pollard, and J.-M. Beckers, 2003: Along or across front ocean survey strategy? the estimation of quasi-geostrophic vertical velocities and temperature fluxes. *Geophys. Res. Lett.*, **30 (5)**. (Cited on page 30.)

Rixen, M. and J.-M. Beckers, 2002: A synopticity test of a sampling pattern in the alboran sea. *J. Mar. Sys.*, **35**, 111–130. (Cited on page 30.)

Rixen, M., J.-M. Beckers, and J. Allen, 2001: Diagnosis of vertical velocities with the qg omega equation: a relocation method to obtain pseudo-synoptic data sets. *Deep Sea Res.*, **48**, 1347–1373. (Cited on page 30.)

Romero, L., Y. Uchiyama, J. C. Ohlmann, J. C. McWilliams, and D. A. Siegel, 2013: Simulations of nearshore particle-pair dispersion in southern california. *J. Phys. Oceanogr.*, **43**, 1862–1879. (Cited on page 15.)

Rose, K. A., et al., 2015: Demonstration of a fully-coupled end-to-end model for small pelagic fish using sardine and anchovy in the California Current. *Prog. Oceanog.*, in press. (Cited on page 2.)

Rossi, V., V. Garçon, J. Tassel, J.-B. Romagnan, L. Stemmann, F. Jourdin, P. Morin, and Y. Morel, 2013: Cross-shelf variability in the Iberian Peninsula Upwelling System: Impact of a mesoscale filament. *Cont. Shelf Res.*, **59**, 97–114. (Cited on pages 57 and 62.)

Rosso, I., A. M. Hogg, P. G. Strutton, A. E. Kiss, R. Matear, A. Klocker, and E. van Sebille, 2014: Vertical transport in the ocean due to sub-mesoscale structures: Impacts in the kerguelen region. *Ocean Modelling*, **80**, 10–23. (Cited on pages 15 and 31.)

Roullet, G. and P. Klein, 2009: Available potential energy diagnosis in a direct numerical simulation of rotating stratified turbulence. *J. Fluid Mech.*, **624**, 45–55. (Cited on page 41.)

Roullet, G., J. C. McWilliams, X. Capet, and M. J. Molemaker, 2012: Properties of steady geostrophic turbulence with isopycnal outcropping. *J. Phys. Oceanogr.*, **42**, 18–38. (Cited on pages 5, 22 and 27.)

Roy, C., 1998: An upwelling-induced retention area off Senegal: a mechanism to link upwelling and retention processes. *South Afr. J. Mar. Sci.*, **19**, 89–98. (Cited on pages 57 and 61.)

Rudnick, D., 1996: Intensive surveys of the Azore front, 2, Inferring the geostrophic and vertical velocity field. *J. Geophys. Res.*, **101**, 16 291–16 303. (Cited on page 28.)

Ruiz, S., A. Pascual, B. Garau, I. Pujol, and J. Tintoré, 2009: Vertical motion in the upper ocean from glider and altimetry data. *Geophys. Res. Lett.*, **36**. (Cited on page 30.)

Ryan, J., et al., 2010: Recurrent frontal slicks of a coastal ocean upwelling shadow. *J. Geophys. Res.*, **115**. (Cited on page 57.)

Sabarros, P. S., D. Grémillet, H. Demarcq, C. Moseley, L. Pichegru, R. H. Mullers, N. C. Stenseth, and E. Machu, 2014: Fine-scale recognition and use of mesoscale fronts by foraging Cape gannets in the Benguela upwelling region. *Deep Sea Res.*, **107**, 77–84. (Cited on page 76.)

Salmon, R., 1980: Baroclinic instability and geostrophic turbulence. *Geophys. Astro. Fluid Dyn.*, **15**, 167–211. (Cited on page 38.)

Sanz, E. P. and Á. Viúdez, 2005: Diagnosing mesoscale vertical motion from horizontal velocity and density data. *J. Phys. Oceanogr.*, **35**, 1744–1762. (Cited on page 29.)

Sasaki, H. and P. Klein, 2012: Ssh wavenumber spectra in the north pacific from a high-resolution realistic simulation. *J. Phys. Oceanogr.*, **42**, 1233–1241. (Cited on pages 15 and 24.)

Sasaki, H., P. Klein, B. Qiu, and Y. Sasai, 2014: Impact of oceanic-scale interactions on the seasonal modulation of ocean dynamics by the atmosphere. *Nat. Commun.*, **5**. (Cited on pages 21 and 45.)

Scales, K. L., P. I. Miller, C. B. Embling, S. N. Ingram, E. Pirotta, and S. C. Votier, 2014: Mesoscale fronts as foraging habitats: composite front mapping reveals oceanographic drivers of habitat use for a pelagic seabird. *Journal of The Royal Society Interface*, **11**, 20140 679. (Cited on page 76.)

Schafstall, J., M. Dengler, P. Brandt, and H. Bange, 2010: Tidal-induced mixing and diapycnal nutrient fluxes in the mauritanian upwelling region. *J. Geophys. Res.*, **115**. (Cited on page 71.)

Schlösser, F. and C. Eden, 2007: Diagnosing the energy cascade in a model of the north atlantic. *Geophys. Res. Lett.*, **34**. (Cited on page 42.)

Schroeder, K., A. Haza, A. Griffa, T. Özgökmen, P. Poulain, R. Gerin, G. Peggion, and M. Rixen, 2011: Relative dispersion in the liguro-provencal basin: From sub-mesoscale to mesoscale. *Deep Sea Res.*, **58**, 209–228. (Cited on pages 18 and 21.)

Scott, R. and F. Wang, 2005: Direct evidence of an oceanic inverse kinetic energy cascade from satellite altimetry. *J. Phys. Oceanogr.*, **35**, 1650–1666. (Cited on page 41.)

Scott, R. K., 2006: Local and nonlocal advection of a passive scalar. *Phys. Fluids*, **56**, 122–125. (Cited on page 17.)

Sharples, J., et al., 2007: Spring-neap modulation of internal tide mixing and vertical nitrate fluxes at a shelf edge in summer. *Limnol. Oceanogr.*, **52**, 1735–1747. (Cited on pages 69 and 76.)

Shcherbina, A. Y., E. A. D'Asaro, C. M. Lee, J. M. Klymak, M. J. Molemaker, and J. C. McWilliams, 2013: Statistics of vertical vorticity, divergence, and strain in a developed submesoscale turbulence field. *Geophys. Res. Lett.*, **40**, 4706–4711. (Cited on page 15.)

Shearman, R. K., J. A. Barth, J. Allen, and R. L. Haney, 2000: Diagnosis of the three-dimensional circulation in mesoscale features with large rossby number. *Journal of physical oceanography*, **30 (11)**, 2687–2709. (Cited on page 29.)

Shearman, R. K., J. A. Barth, and P. M. Kosro, 1999: Diagnosis of the three-dimensional circulation associated with mesoscale motion in the california current. *Journal of Physical Oceanography*, **29 (4)**, 651–670. (Cited on page 28.)

Skyllingstad, E. D. and R. Samelson, 2012: Baroclinic frontal instabilities and turbulent mixing in the surface boundary layer. part i: Unforced simulations. *J. Phys. Oceanogr.*, **42**, 1701–1716. (Cited on page 44.)

Smith, C., K. Richards, and M. Fasham, 1996: The impact of mesoscale eddies on plankton dynamics in the upper ocean. *Deep Sea Res.*, **43**, 1807–1832. (Cited on page 2.)

Soufflet, Y., P. Marchesiello, J. Jouanno, X. Capet, L. Debreu, and F. Lemarié, 2015: On effective resolution in ocean models. *Ocean Model.*, **119**, 8315–8335, submitted. (Cited on page 5.)

Spall, S. and K. Richards, 2000: A numerical model of mesoscale frontal instabilities and plankton dynamics - i. model formulation and initial experiments. *Deep Sea Res.*, **47 (I)**, 1261–1301. (Cited on pages 32 and 34.)

Stone, P., 1966: On non-geostrophic baroclinic instability. *J. Atmos. Sci.*, **23**, 390–400. (Cited on pages 34 and 37.)

Sundermeyer, M. A. and J. R. Ledwell, 2001: Lateral dispersion over the continental shelf: analysis of dye-release experiments. *J. Geophys. Res.*, **106**, 9603–9621. (Cited on page 19.)

Talandier, C., et al., 2014: Improvements of simulated western north atlantic current system and impacts on the amoc. *Ocean Model.*, **76**, 1–19. (Cited on page 48.)

Taylor, J. R. and R. Ferrari, 2009: On the equilibration of a symmetrically unstable front via a secondary shear instability. *J. Fluid Mech.*, **622**, 103–113. (Cited on page 38.)

Taylor, J. R. and R. Ferrari, 2010: Buoyancy and wind-driven convection at mixed layer density fronts. *J. Phys. Oceanogr.*, **40**, 1222–1242. (Cited on pages 15 and 38.)

Taylor, J. R. and R. Ferrari, 2011: Ocean fronts trigger high latitude phytoplankton blooms. *Geophys. Res. Lett.*, **38**. (Cited on page 38.)

Thomas, L., 2005: Destruction of potential vorticity by winds. *J. Phys. Oceanogr.*, **35**, 2457–2466. (Cited on pages 12, 15, 26 and 37.)

Thomas, L., 2008: Formation of intrathermocline eddies at ocean fronts by wind-driven destruction of potential vorticity. *Dyn. Atm. Ocean*, **45 (3-4)**, 252 – 273. (Cited on pages 26 and 37.)

Thomas, L. and C. Lee, 2005: Intensification of ocean fronts by down-front winds. *J. Phys. Oceanogr.*, **35**, 1086–1102. (Cited on pages 12 and 15.)

Thomas, L., C. Lee, and Y. Yoshikawa, 2010: The subpolar front of the japan/east sea ii: inverse method for determining the frontal vertical circulation. *J. Phys. Oceanogr.*, **40**, 3–25. (Cited on pages 26, 28 and 37.)

Thomas, L. and J. Taylor, 2010: Reduction of the usable wind-work on the general circulation by forced symmetric. *Geophys. Res. Lett.*, **37**, L18 606. (Cited on pages 26, 29, 30 and 44.)

Thomas, L. N. and T. M. Joyce, 2010: Subduction on the northern and southern flanks of the gulf stream. *J. Phys. Oceanogr.*, **40**, 429–438. (Cited on pages 26, 28, 30, 37 and 38.)

Thomas, L. N., A. Tandon, and A. Mahadevan, 2008: Submesoscale processes and dynamics. *Ocean Modeling in an Eddying Regime*, M. Hecht and H. Hasumi, Eds., Am. Geophys. Union, Geophys. Monog. Ser., Vol. 177, 17–38. (Cited on page 28.)

Thomas, L. N., J. R. Taylor, R. Ferrari, and T. M. Joyce, 2013: Symmetric instability in the gulf stream. *Deep Sea Res.*, **91**, 96–110. (Cited on pages 30, 34, 38 and 44.)

Tourbillon, G., 1983: The tourbillon experiment: a study of a mesoscale eddy in the eastern north atlantic. *Deep Sea Res.*, **30**, 475–511. (Cited on page 2.)

Tulloch, R., J. Marshall, C. Hill, and S. Smith, 2011: Scales, growth rates and spectral fluxes of baroclinic instability in the ocean. *J. Phys. Oceanogr.*, **41**, 1057–1076. (Cited on page 27.)

Tweddle, J. F., J. Sharples, M. R. Palmer, K. Davidson, and S. McNeill, 2013: Enhanced nutrient fluxes at the shelf sea seasonal thermocline caused by stratified flow over a bank. *Prog. Oceanog.*, **117**, 37–47. (Cited on pages 69 and 76.)

Ullman, D. S. and P. C. Cornillon, 1999: Satellite-derived sea surface temperature fronts on the continental shelf off the northeast U.S. coast. *J. Geophys. Res.*, **104**, 23 459–23 478. (Cited on page 21.)

Vanneste, J., 2013: Balance and spontaneous wave generation in geophysical flows. *Annu. Rev. Fluid Mech.*, **45**, 147–172. (Cited on page 39.)

Veneziani, M., A. Griffa, Z. Garraffo, and J. A. Mensa, 2014: Barrier layers in the tropical south atlantic: Mean dynamics and submesoscale effects*. *J. Phys. Oceanogr.*, **44**, 265–288. (Cited on page 15.)

Vic, C., G. Roullet, X. Carton, and X. Capet, 2014: Mesoscale dynamics in the arabian sea and a focus on the great whirl life cycle: A numerical investigation using roms. *J. Geophys. Res.*, **119**, 6422–6443. (Cited on pages 3 and 5.)

Viúdez, Á. and D. G. Dritschel, 2004: Potential vorticity and the quasigeostrophic and semigeostrophic mesoscalevertical velocity. *J. Phys. Oceanogr.*, **34**, 865–887. (Cited on page 29.)

Weimerskirch, H., M. Le Corre, S. Jaquemet, M. Potier, and F. Marsac, 2004: Foraging strategy of a top predator in tropical waters: great frigatebirds in the Mozambique Channel. *Mar. Ecol. Prog.*, **275**, 297–308. (Cited on page 76.)

Whitt, D. B. and L. N. Thomas, 2013: Near-inertial waves in strongly baroclinic currents. *Journal of Physical Oceanography*, **43 (4)**, 706–725. (Cited on page 48.)

Whitt, D. B. and L. N. Thomas, 2015: Resonant generation and energetics of wind-forced near-inertial motions in a geostrophic flow. *J. Phys. Oceanogr.*, **45**, 181–208. (Cited on page 48.)

Williams, C., J. Sharples, C. Mahaffey, and T. Rippeth, 2013: Wind-driven nutrient pulses to the subsurface chlorophyll maximum in seasonally stratified shelf seas. *Geophys. Res. Lett.*, **40**, 5467–5472. (Cited on page 69.)

Woodson, C., L. Washburn, J. A. Barth, D. Hoover, A. R. Kirincich, M. McManus, J. P. Ryan, and J. Tyburczy, 2009: Northern monterey bay upwelling shadow front: Observations of a coastally and surface-trapped buoyant plume. *J. Geophys. Res.*, **114**. (Cited on page 57.)

Woodson, C., et al., 2007: Local diurnal upwelling driven by sea breezes in northern Monterey Bay. *Cont. Shelf Res.*, **27**, 2289–2302. (Cited on page 57.)

Wunsch, C. and R. Ferrari, 2004: Vertical mixing, energy, and the general circulation of the oceans. *Annu. Rev. Fluid Mech.*, **36**, 281–314. (Cited on page 38.)

Xu, Y. and L.-L. Fu, 2012: The effects of altimeter instrument noise on the estimation of the wavenumber spectrum of sea surface height. *J. Phys. Oceanogr.*, **42**, 2229–2233. (Cited on pages 15 and 24.)

Yelekci, O., et al., 2014: Observing submesoscale activity in the bay of biscay with satellite-derived sst and chlorophyll concentration. *European Geosciences Union General Assembly 2014*. (Cited on page 21.)

Yoshikawa, Y., C. M. Lee, and L. N. Thomas, 2012: The subpolar front of the japan/east sea. part iii: Competing roles of frontal dynamics and atmospheric forcing in driving ageostrophic vertical circulation and subduction. *J. Phys. Oceanogr.*, **42**, 991–1011. (Cited on pages 35 and 37.)

Young, W. and M. B. Jelloul, 1997: Propagation of near-inertial oscillations through a geostrophic flow. *J. Mar. Res.*, **55**, 735–766. (Cited on page 2.)

Zhong, Y. and A. Bracco, 2013: Submesoscale impacts on horizontal and vertical transport in the gulf of mexico. *J. Geophys. Res.*, **118**, 5651–5668. (Cited on pages 15, 18 and 31.)

Contributions to the understanding of meso/submesoscale turbulence and their impact on the ocean functioning

Abstract: The ocean is variable on a broad range of scales and for a variety of reasons. The role of mesoscale subinertial currents has been known for a long time to be an important aspect of the ocean circulation. At the other end of the spectrum superinertial motions (near-inertial waves, inertia-gravity waves) are also important to the ocean functioning. In between, subinertial turbulent processes termed "submesoscale" exist, with time and space scales that largely overlap with those of superinertial motions. Submesoscale activity results from the intensification of fronts in the upper ocean. In this manuscript I strive to describe my research contribution from 1998 to 2015 on mesoscale and submesoscale turbulence. Some of their interactions with superinertial processes on which I have also worked are also discussed. This work is put into the proper scientific context through a substantial review effort.

Keywords: Mesoscale, submesoscale, upwelling, ocean fronts

The southern Senegal upwelling center: state and functioning during the UPSEN2/ECOAO field experiments (Feb.-Mar. 2013)

Xavier Capet *

LOCEAN, Paris, France

Philippe Estrade

LPAO-SF,Dakar, Sénégal

Eric Machu

Laboratoire de Physique des Océans, Plouzané, France; LPAO-SF,Dakar, Sénégal

Siny Ndoye

LPAO-SF,Dakar, Sénégal; LOCEAN, Paris, France

Jacques Grelet

Imago, Plouzané, France

Alban Lazar

LOCEAN, Paris, France

Louis Marié

Laboratoire de Physique des Océans, Plouzané, France

Denis Dausse

LOCEAN, Paris, France

Patrice Brehmer

Laboratoire d'écologie marine, Plouzané, France

* *Corresponding author address:* LOCEAN, 75005 Paris,

E-mail: xavier.capett@locean-ipsl.upmc.fr

ABSTRACT

.Upwelling off southern Senegal and Gambia takes place over a wide shelf with a large area where depth is shallower than 20 m. This results in typical upwelling patterns that are distinct from those of other better known systems, including Oregon and Peru where inner shelves are comparatively narrower. A $\sim$ 4 weeks intensive measurement period sheds light on the synoptic and superinertial variability of this upwelling sector. The influence of mesoscale activity extends across/through the shelf break deep into the shelf where it impacts the mid-shelf upwelling, possibly in concert/synchrony with wind fluctuations. Internal tides and solitary waves of large amplitude are ubiquitous over the shelf. Our observations suggest that they and possibly other sources of mixing play a significant role in the overall system functioning. Both synoptic and superinertial variability exert a profound influence on the shelf biogeochemistry.

1. Introduction

Coastal upwelling systems have received widespread attention for several decades owing to their importance for human societies. Although the primary driving mechanism is generic important differences exist between systems and also between sectors of each given system. Stratification, shelf/slope topographic shapes, coastline irregularities and subtleties in the wind spatial/temporal structure have a major impact on upwelling water pathways and overall dynamical, hydrological, biogeochemical (**?**) and ecological (Pitcher et al. 2010) characteristics of upwelling regions. Over the past decade processes associated with short time scales (daily and faster) have progressively been incorporated which adds further complexity and many local specificities.

These advances have to a large extent taken place in the California Current System (Woodson et al. 2007, 2009; Ryan et al. 2010; Kudela et al. 2008; Lucas et al. 2011a) and to a lesser extent in the Benguela system Lucas et al. (2014) and Northern Canary system. Conversely, our understanding of West African upwellings remains to a large extent superficial (*i.e.,* guided by satellite and sometimes surface in situ measurements; Roy 1998; Demarcq and Faure 2000; Lathuilière et al. 2008), low-frequency and relatively large scale.

Despite an original large-scale context the southern end of the Canary system is thus one upwelling sector that is least well known, at least dynamically. Between the Cape Verde frontal zone (which approximately runs between Cape Blanc ($\sim 21^o$N, Mauritania) and the Cape Verde archipelago (Barton 1998), see Fig. 1) and Cape Roxo (12^o 20'N) the wind regime is responsible for quasi-permanent Ekman pumping and winter/spring-time coastal upwelling. The former extends hundreds of kilometres offshore and drives a large scale

cyclonic circulation whose manifestation includes the Mauritanian Current (MC hereafter, see Fig. 1). The MC differs from poleward undercurrents typical of many upwelling systems in that it is generally intensified at or close to the surface (Peña-Izquierdo et al. 2012; Barton 1989), reflecting the strength of the forcing. In the south, the MC connects with the complex equatorial current system and the connection involves a quasi-stationary cyclonic feature, the Guinea dome (more details can be found in Barton 1998, Arístegui et al. 2009). Fig. 1 is suggestive of the role of the MC in maintaining a relatively warm environment in the immediate vicinity of the shelf break over the latitude band 12^o-17^oN, despite sustained coastal upwelling.

Seasonality of hydrology and circulation of the coastal ocean off this part of West Africa are tightly controlled by the displacements of the Inter-Tropical Convergence Zone (**?**). During the monsoon season (Jul.-Oct.) weak westerly winds (interrupted by occasional storm passages and easterly waves) dominate and the region receives the overwhelming fraction of its annual precipitations. From approx. November to May the ITCZ is located to the south and upwelling favorable trade winds dominate. Their peak intensity is in February-April. The migration of the ITCZ also drives the cyle of freshwater run-offs to the coastal ocean, a presumably large fraction of which occurs through the Senegal outflow, with limited contributions from Sine-Saloum, Gambia and Casamance rivers. The effect of freshwater input to the coastal ocean is evident during the monsoon season when warm and fresh so called Guinea waters cover most of the area. It is conversely insignificant during the core of the upwelling season which is of interest in this study (*e.g.,* ≈ 100 m^3 s^{-1} in Feb.-March for the Senegal river to be compared with ≈ 2000 m^3 s^{-1} in Sep.-Oct. during the monsoon season, http://www.grdc.sr.unh.edu/).

Two coastal sectors can be distinguished in this region, based on small distinctions in their atmospheric forcings, influence of the surrounding ocean and also shelf/slope morphology. North of the Cape Verde peninsula the shelf is relatively narrow (up to the Banc d'Arguin), and, because this is the northern limit of the ITCZ migration, the upwelling season is longest. This study reports and analyses observations carried out in the southern sector offshore of southern Senegal (between Cape Verde peninsula and $\sim 13^o 40$'N, see Fig. 1) during $\sim$ 25 days in February-March 2013. The role of this coastal region as fishing ground and small pelagic fish nursery is an important motivation to this work.

During the upwelling season this sector acts as an upwelling center named Southern Senegal upwelling center (SSUC) below. The terminology "upwelling center" refers to the existence of a well-identified and persistent focal point where upwelling is enhanced, as vividly revealed by SST images. Downstream (*i.e.,* southward) of the center upwelling aided by alongshore advection forms a cold tongue (Fig. 1). In strongly turbulent upwelling systems with intense cross-shore exchanges the tongue is predominantly directed toward the slope and open ocean where it takes the form of filaments (Strub et al. 1991). Mesoscale activity is not particularly intense in the Canary system (Capet et al. 2008a; Marchesiello et al. 2011). In addition, the SSUC is characterised by a wide shelf except in its northern part: south of $14^o 30$'N the shelf break, roughly defined by 100 m isobath, is over 50 km from the shore while water depth is less than 30 m over a 1/3 to more than 1/2 of the shelf area (*e.g.,* see Fig. 3).

Thus, coastal upwelling in the SSUC is partly sheltered from the mesoscale turbulence taking place over the continental slope and open ocean. This has several related implications: the general orientation of the cold upwelling tongue is north to south and it preserves its coherence over long distances (up to three-four hundred kilometers in some circumstances);

temporal stability of the tongue is also noticeable over periods of many days to weeks; a substantial contribution of upwelling presumably complements alongshore advection downstream of the main upwelling area in the north[1]; export from the shelf to the open ocean is retarded.

This being said, the degree of insulation between coastal upwelling and offshore turbulent activity needs to be qualified. South of 14°30'N, the core of the upwelling tongue is frequently found 50 km or more away from the coast within the range of influence of large slope/shelf break eddies and meanders whose surface expression is frequently seen impinging on the outer shelf (Ndoye et al. 2014). Such situations occur preferentially between February and April and prevailed during our observational period.

Coalescence between the surface and bottom boundary layers has traditionally been invoked as the main explanation underlying the displacement of the upwelling tongue away from the shoreline (Estrade et al. 2008; Austin and Lentz 2002). Indeed, the alongshore momentum balance of well-mixed inner-shelf waters involves a compensation between wind and bottom friction with little or no offshore Ekman transport needed. Therefore coastal divergence is expected to take place where water is deep enough for the two boundary layers to separate, typically 15 to 40 m depending in part on wind intensity (stronger winds lead to both thicker surface boundary layers but also thicker bottom boundary layers because they tend to increase the strength of the upwelling jet as confirmed by observations described below).

[1]In other words the concept of wake in which water upwelled in a confined area would simply be advected horizontally may not be fully relevant. Also, note that the cold tongue should be distinguished from upwelling filaments in which a key dynamical process is subduction of recently upwelled water as it flows offshore past the shelf break)

The zonal migration of the upwelling tongue seasonally (very close to shore in the early season, farthest offshore in March and retreating back inshore in April-May) is consistent with the cycle of upwelling wind intensity Ndoye et al. (2014). On the other hand the analysis of SSUC SST also shows behaviors of the cold upwelling tongue (in terms of zonal position and displacements) suggestive that other processes are at play. Further north, over a wide continental shelf resembling ours Barton et al. (1977) observe an upwelling front migrate offshore during two consecutive upwelling events without any evident relation to changes in wind intensity. A similar behavior will be described below for the SSUC. Overall, the connection between offshore migration of the upwelling zone and wind intensity is not very clear, at least on synoptic time scales.

The purpose of this study is to clarify this issue and more generally shed light on the dynamical functioning of the SSUC. We do so based on the analysis of a dataset gathered during 2 intensive field experiments carried out in February-March 2012-2013 (amounting to 25 days at sea). The general strategy was to cover multiple times a relatively limited area of 1^o by 1^o (Fig. 1) with measurements of physical, biogeochemical and ecological parameters. We will focus on the former. Multiple observational evidences support the views that i) shelf break/open ocean mesoscale disturbances exert some influence on the shelf dynamics ii) interactions between subinertial and superinertial (internal gravity waves in particular) dynamics are fundamental to the system functioning.

The manuscript is organized as follows. Section 2 presents the data and methods. Section 3 describes the evolution of the SSUC state and circulation on time scales of days to the duration of the field experiments. Emphasis is placed on the mid-shelf area where moored instruments allow us to better characterize the SSUC dynamics. In Section 4 we present a

set of observations pertaining to the internal wave field, from the ship echosounder and also from moored instruments. The final section summarizes and elaborates on our findings and their consequences.

2. Data and Methods

a. Moored Instruments

A string of instruments (hereafter refered to as M28) was deployed in about 28 m water depth at 14^{o}N, 17^{o}05'950W on 23 February (8 AM) and recovered on 12 March (3 PM). It consisted of ten temperature (T) sensors and ten T, salinity (S) and pressure sensors. Instruments were irregularly spaced from 1m above the bottom to about 3m below the surface. Their position along the string was carefully measured and pressure measurements were used to infer pressure at T only locations using linear interpolations. Sampling interval was one minute for all instruments. Two thermistors did not record data but the vertical resolution remains adequate to capture temperature fluctuations. Measurements made by the remaining 18 sensors are used to obtain a temperature time-depth gridded field (see Fig. 7e) through objective analysis following Bretherton et al. (1976) (using 1 m and 2 mn for the vertical and time resolution of the grid and 1 m and 4 mn for the decorrelation depth and time scale ; the decorrelation time scale is chosen so that internal wave signals with periods $\sim$ 10 mn or more are preserved).

Three upward-looking ADCP moorings were also deployed 0.5 nm west and east (RDI 300 kHz respectively refered to as RDIW and RDIE) and south (AQUADOPP 400 Khz; AQDS)

of the thermistor line. Mean water depth at the moorings ranged from approximately 29 m (RDIW) to 26.5 m (RDIE). One ADCP was also present to the north but capsized a few hours after deployment. One additional ADCP AQUADOPP 600 kHz was moored a few miles to the east in 23m depth (AQDI). Deployment of the ADCPs took place on 22 Feb. between 10:20 AM and 12:10 PM. Recovery took place on 12 (RDIW) or 15 March. RDI (resp. AQUADOPP) ADCPs sampled every 2 mn (resp. 5 mn) with vertical bins of 1m. Accounting for the depth at which the instruments head was located ($\approx$ 0.5 m above ground) and a 1 m blanking distance the lowest valid measurement is centered at 2m above the bottom. Because of side lobe reflection from the air-sea interface the shallowest useable bin is centered 5m depth. The barotropic component of measured currents were detided using the software T_Tide (Pawlowicz et al. 2002). M2 is by far the dominant constituent (not shown).

b. Hydrographic Measurements

Zonal (approximately across-shore) CTD transects were repeated at 14^o, 14^o30' and 13^o40' N during the surveys and additional yoyo CTD stations were also performed. Data were acquired using a SBE911+, measuring redundantly pressure, temperature and conductivity at 24Hz, and fluorescence, oxygen at ?? Hz. Data postprocessing was performed using the seabird SBE processing software and follow standard practices as described in many studies (see Morison et al. 1994 for example). Only the downcast profiles are used for analysis; during the upcast sensors are in the wake of the package and CTD frame (Alford and Pinkel 2000). Raw pressure is filtered using a 15 point triangle window. This is enough to eliminate

all pressure reversals despite the relatively low drop speed we chose to increase vertical resolution (0.5 m s^{-1}). We attribute this to CTD operation through a moon pool located toward the center of R/V ANTEA which limits heave effects. Sea states were also generally favorable with limited swell in the area. A 5 point median filter is applied to temperature and salinity. A correction for the conductivity cell thermal mass (Morison et al. 1994) is also applied, requiring the knowledge of two parameters α (initial amplitude) and τ (time scale) that characterize conductivity measurement error when instantaneously applying a 1^oC step in temperature. SBE default values were checked and slightly modified using a series of profiles exhibiting abrupt T jumps at the interface of a well-mixed 20-30 m thick bottom layer. The salinity profile closest to a step was obtained for α=0.025 and τ=7 s and these values are used for all CTD profiles. For most purposes including the construction of hydrological transects, depth averaging is performed over 1 m bins. Bin size is reduced to 0.15 m to construct yoyo CTD profiles used to estimate dissipation and mixing intensity, through the computation of Thorpe scales (Sec. 4). This roughly corresponds to 7 scans at the drop speed of 0.5 m s^{-1}.

Alongtrack surface temperature and salinity are available from the ship thermosalinometer (SBE21).

Because of a malfunction on its system pressure sensor the SCANFISH embarked on R/V Antéa was used only occasionally, in conditions where the instrument depth was not easily controllable (depth changes required playing with the cable length) and generally restricted to the upper half of the water column to prevent bottom hitting. It carried recently calibrated temperature, salinity, fluorescence and BB3 sensors.

c. Other Measurements

R/V Antéa is equipped with a 4 frequencies scientific echo-sounder SIMRAD EK60 (38, 70, 120 and 200 kHz). Ping rate is 1 Hz which yields a 3.5 m native resolution for the echograms when the ship steams at 8 knots.

The weather station onboard R/V Antéa (Batos 1.1D) provides atmospheric condition information every 10 seconds. Wind speed and direction are mesured atop of the ?? at ?? m height. To minimize the effect of airflow distorsion by the ship superstructure measurements corresponding to aft-wind conditions are systematically discarded. Hourly wind at the Yoff weather station at Dakar Airport, Senegal (14^o44'N, 17^o30'W, 27 m above ground; hereafter DWS) are obtained from http://www.ogimet.com/metars.phtml.en. ASCAT scatterometers onboard METOP-A and B provide 2D wind measurements between 0 and 3 times a day, around 10:30 AM and/or 10:30 PM. We use the 12.5 km L2 products from NASA (ftp://podaac-ftp.jpl.nasa.gov/allData/ascat) and present these observations after spatial averaging over different subdomains of the SSUC.

Moderate Resolution Imaging Spectroradiometer 'MODIS' onboard the Terra (10:30 AM equator crossing time, descending) and Aqua (1:30 PM equator crossing time, ascending) provide numerous high quality SST during the experiment period. We use L2 SWATH products distributed by NASA (http://oceancolor.gsfc.nasa.gov). The metric ground resolution varies depending on view angle but remains close to the nominal 1 km value. Cloud masking produces numerous false positives in upwelling regions and we instead rely on visual examination over the SSUC to keep or discard images.

3. Subinertial SSUC dynamics

Several types of observations give a complementary perspective (discussed below) on the physical situation during the campaigns and particularly on the sequence of synoptic events.

a. Synoptic variability

DWS is generally quite representative of synoptic wind conditions over the SSUC, especially in situations where northwesterlies dominate (Ndoye et al. 2014), as during UPSEN2/ECOAO. Analysis of DWS wind records (Fig. 2a) suggest to define three coherent subperiods: a moderate relaxation period RL1 from the beginning of the cruise (22 February) to 27 February when the wind over the previous inertial period is back to above 5 m s^{-1}; 28 February to 12 March (UP1) during which the wind intensity remains essentially between 5 and 7 m s^{-1}; from 12 March to 17-18 March during which another relaxation period RL2 takes place that, beside a more rapid initiation and a longer duration ($\sim$ 5 days versus 3-4 days), resembles the early one. The short upwelling event taking place around 20-21 February just before UPSEN2 is refered to as UP0.

This description of DWS winds is not inconsistent with ship weather station observations made within 50 km from M28 reported in Fig. 2d. For example, weakest (respectively strongest) ship winds are found on 25 February and 15 March (resp. 28 February and 8 March). This being said, limited coverage and significant intradaily variability tend to overshadow the synoptic signal and curtail a detailed comparison.

During most of the experiment upwelling wind intensity at M28 peaks in the evening or early at night and is minimum around mid-day (Fig. 2e). The daily wind cycle has a

much lower amplitude at DWS and maximum wind intensity accurs around 2PM (see Ndoye et al. 2014). We note that upwelling events seem to manifest themselves through increased maximum wind intensities while morning winds remain generally weak.

In Fig. 2b we show the zonal minimum temperature over the shelf averaged in the latitude range 14^o-14^o30'N, computed for all cloud-free MODIS SST images (a subset of these images is presented in Fig. 3). The upwelling event finishing around the beginning of UPSEN2 UP0, short relaxation period RL1, central upwelling event UP1, and final relaxation RL2 are clearly identifiable as SST fluctuations of $\sim$ 2-3^{o}C. The termination date of RL1 cannot be determined precisely in SST because no MODIS SST is available on 25 and 26 February but declining temperatures on 27-28 February approximately coincide with the increase in upwelling wind intensity. As for the SST warming during the late part of the observation period its initiation precedes the marked wind drop on 12-13 March and closely follows the absolute SST minimum obtained on 8 March toward the end of UP1. In SST RL2 is most marked on 17 March, *i.e.,* at the return of more upwelling favorable wind conditions.

Overall, the storylines framed based on DWS winds or synoptic evolution of the system SST are in agreement, considering the measurement limitations and complexity of the ocean response to wind changes.

b. SSUC mesoscale variability

During the entire experiment period the frontal zone between the cold upwelling water and warmer offshore water is being distorted and forms $\sim$ 20-100 km filaments and meanders, some of which acquire quasi-circular shapes (Fig. 3). As demonstrated for other upwelling

systems these mesoscale structures are the manifestation of baroclinic-barotropic instability (Marchesiello et al. 2003). The tendency of filaments to orient themselves along a NW-SE axis (Fig. 3e-h) reflects the intense lateral shear between the poleward Mauritanian current and the inshore equatorward upwelling flow.

In their analysis of the MODIS SST database Ndoye et al. (2014) identify a recurrent mesoscale situation where a 30-100 km anticyclone (refered to as CVA for Cape Verde Anticyclonic structure) hugs the Cape Verde headland. In Feb.-March 2013 3 different CVAs consecutively occupy the northern SSUC following a sequence of events involving 1) northward propagation and deformation/amplification of a Mauritania current meander initially situated further south 2) phase-locking or reduced propagation of the meander which takes a more circular shape and remain in the immediate vicinity of the Cape Verde headland for several days 3) weakening of the structure (seemingly through dissipation and straining) to the point where it is blown northward.

At the beginning of UPSEN2 (21-23 Feb.) the remains of a small CVA (CVA-2) better identifiable at earlier times (18 Feb., not shown) are still visible within 50 km to the south/southwest of Cape Verde (Fig. 3a). On 27 February (Fig. 9) the SST signal of CVA-2 has strongly faded away. The SST scene for 28 February (Fig. 3c) captures the transient situation when $\sim 18^o$C water occupies the vicinity of Cape Verde and warmer water is located $\sim$ 30 km further offshore. It also reveals the final stage of the evacuation of CVA-2 which has been stirred beyond recognition in the deformation region near 17^o45'W, 14^o45'N; and the northward progression of the frontal edge oriented NW-SE that separates a warm MC meander from upwelling water between 13^o40'N and 14^o50'N (compare Fig. 3b and c). This frontal zone had remained quasi-stationary from 21 Feb to 24-25 Feb. By 3 March it has

shifted northward considerably (Fig. 3d). It is then partly located north of Cape Verde and hugs the headland toward its middle. The northern and southern parts of the front evolve somewhat independantly thereafter. North of Cape Verde, the front progresses northward and forms a barrier for cold upwelled water (Fig. 3e) even right at the coast where SST are systematically warmer than 20^oC during UP1. South of Cape Verde the front combines with a $\sim 20^oC$ water filament located at 17^o45'-18^oW to form the quasi-circular edge of what appears to be a mesoscale eddy (CVA-3) between 5 and 10-12 March (Fig. 3e,f).

The SST signature of CVA-3 is progressively eroded particularly its eastern side as seen on 12 March (Fig. 3f). On 14 March (Fig. 3g) remains of CVA-3 are barely visible as a bulge of $\sim 20^oC$ water near 17^o45'W, 14^o30'N . Later on during RL2 SST images reveal a major reorganization of the flow structure in the vicinity of the Cape Verde peninsula. The upwelling signature on SST is confined to the northern SSUC (note that the maintenance of some upwelling is consistent with DWS wind records). The orientation of the wake of waters upwelled at the Cape Verde peninsula suggests that the surface flow is directed offshore on 18 March (Fig. 3i) in the region between the coast and a subsequent warm meander still situated approximately 50 km offshore to the southwest. VIIRS ocean color images available for 17 and 18 March further support the onset of an offshore surface flow in the northern SSUC toward the end of RL2 (not shown).

The mesoscale features described above are typically located over the continental slope but they also frequently extend beyond the shelf break as described below using in situ observations. Their evolution is tied to that of the SSUC cold tongue over the shelf, *e.g.,* through upwelling filaments. Pending modeling sensitivity analyses our conceptual view of the SSUC dynamics considers wind and MC transport synoptic variability, upwelling response over the

shelf, and instability of the shelf/shelf break/slope current system as important ingredients with multiple interplays between them.

c. Subsurface properties and thermohaline structure

The set of CTD casts carried out during the experiments offers important subsurface information. In particular it allows us to examine the properties of the cold subsurface water that feeds the upwelling, including its temporal evolution. Stratification is also useful as a signature of mixing. Fig. 4 represents the across-shelf distribution of temperature, salinity, dissolved oxygen and fluorescence in the bottom layer, and surface to bottom temperature and salinity differences. Figs. 5 and 6 represent T and S along 13 of the 17 main cross-shore transect lines).

All transects exhibit the signature of cold (14-15^{o}C), fresh, dissolved oxygen and fluorescence poor subsurface water rising up the shelf to feed the Ekman divergence. A remarkable trait of this signature is that it tends to fade away when approaching the shore, although to various degrees depending on the transect and the tracer. The southern transects (T4, T9 and to a lesser extent T14) exhibit the most pronounced changes in bottom water T,S properties across the shelf. The northern transects (at 14^o 30'N) T1 and T12 are those where bottom water T,S properties are best preserved. Although this does not apply to T8 it confirms the visual impression from SST images that the shelf is preferentially fed with slope waters in the northern SSUC (see also the idealized work of Crépon et al. 1984).

The cross-shelf changes in tracer properties strongly depend on the tracer itself. Salinity and temperature experience marked relative changes between the shelf break and the 15 m

isobath. The changes can be significant over the outer shelf for salinity with a tendency to saturation at about 35.6 psu for depths shallower than 40-50 m (see Fig. 4b). The cross-shore structure is reversed for temperature with the most significant changes occuring at depths shallower than 30 m. However the warming trend from deep to shallow parts of the shelf is ubiquitous. For dissolved oxygen changes are very limited at depths greater than $\sim$ 30 m and consist in a slight reduction from offshore to nearshore (except from 2 hypoxic stations which will be analyzed in a forthcoming study). For shallower depths a large variability is found, particularly at the central and southern transects. Changes in fluorescence resemble those for oxygen although they are less concentrated to the shallowest depths, *e.g.,* the outer shelf variability is much more pronounced.

The tendency for bottom water properties to approach surface values when getting closer to shore goes in pair with a reduction in surface to bottom stratification (Fig. 4e,f), which occasionally vanishes inshore of the 30 m isobath. This points to the importance of vertical mixing as a process controlling the distribution of water column properties. Other processes shape the mean tracer distribution and in particular sources and sinks. We presume that biological activity is able to maintain sharp vertical contrasts in oxygen and fluorescence between the upper 20-40 meters and the layer below and prevent mixing from significantly affecting the distribution of these two tracers. This may be particularly true toward the bottom where the quasi-absence of oxygen and chlorophyl vertical gradient should make mixing relatively ineffective. Conversely, the absence of interior source/sink for temperature and salinity allows vertical mixing to have a major impact on these fields. Biogeochemical observations will be described and analyzed more thorougly in a forthcoming study.

A key dynamical feature of upwellings systems is the upwelling front. In idealized numer-

ical solutions this front possesses several defining characteristics (Allen et al. 1995; Austin and Lentz 2002; Estrade et al. 2008): it is the physical barrier between non-upwelling and cold upwelling waters, *i.e.,* it is the zone of maximum surface density gradient (this can also be true for other tracers); it is a place of equatorward alongshore velocity maximum; it coincides with the main pycnocline outcrop; and lowest/vanishing stratification should be found on its inshore flank, *i.e.,* the upwelling zone where cold interior waters are incorporated into the surface layer. The complexity of the SSUC upwelling structure leads to equivocal situations regarding the definition/localization of the upwelling front and zone. In particular the surface temperature and salinity across-shore gradients are most often weak and diffuse, *e.g.,* 2^o C over 25 km for T1, from CTD6 to CTD12. The only notable exception is found during T6 (14^oN) where a 1.4^oC change was observed over an horizontal distance of 250 m. Likewise, choosing an isopycnal as characteristic of the offshore pycnocline and following it across the shelf to its outcroping position does not reliably help define the location of the upwelling front. The main reason for this is that considerable changes in stratification and thermohaline structure occur across the shelf, not just in the bottom layer as decribed above but also at mid-depth. Manifestations of intense mixing of thermocline waters include the presence of blobs of water in temperature classes that are almost unrepresented offshore (CTD43 in T4, CTD55-56 in T5, CTD70 in T6, CTD108-111 in T10, CTD163 in T15).

In other words, except at the northern transects T1, T8 and T12 (which correspond to a classic coastal upwelling situation) and at the southern T14 (which resembles the idealized 2D subinertial mid-shelf upwelling studied in Estrade et al. 2008 and Austin and Lentz 2002) the exact location where upwelling is taking place is difficult to identify precisely. For example, T6 has a strong surface density gradient and an almost well mixed water column at

17^o10'W but a significant amount of cold bottom water resides inshore of that location. A more dramatic exemple is obtained for T15 at the end of upwelling event UP1. On 12 March the upwelling front location at 14^oN determined as the place of zonal minimum SST (from MODIS SST in Fig. 2c or TSG data, not shown) sits around 17^o25'W in 75 m water depth near CTD 163. On the other hand a secondary SST minimum (see Fig. 2c) is found much closer to shore near M28 and cold bottom water resides over most of the shelf, including at mooring M28 (see Fig. 7).

We attribute the loss of bottom water tracer properties toward the shore and, more generally, the complexity of the shelf thermohaline structure, to intense vertical mixing. Although bottom friction may be also implicated we present evidences that internal gravity waves breaking should play an important role as a source of mixing In Sec. 4.

d. Mid-shelf variability

The description above can be complemented by and confronted to the continuous current and temperature measurements available at 14^oN about the 28 isobath, although records cover a restricted period from 23 February to 12 or 15 March.

Heat content and stratification at M28 are mainly consistent with SST evolution there (or more broadly over the shelf), *i.e.,* they roughly follow the wind conditions. Heat content (Fig. 7c) undergoes a major increase from 25 to 27-28 February during RL1 and a rapid decrease on 28 February at the beginning of UP1. Changes before the 25th or after the 28th are comparatively modest in amplitude and rate but an upward trend is noticeable from 2 to 8 March and 10 to 12 March with a fall-off between these two periods. Assuming that only

air-sea exchanges contribute to the heat content increases during RL1 would imply a net air-sea heat flux of $\sim +$ 200 W m^{-2}. During UP1 onset phase a similar assumption would imply unrealistic heat losses of the order of -400 W m^{-2} and lateral advection is presumably implicated in the drop. Largest temperature changes are near the surface (Fig. 7e) where currents are about 3 times stronger than near the bottom ($\sim$ 25 versus 7-10 cm s^{-1}, see Fig. 8). This strongly suggests that a key term driving M28 heat changes in the beginning of UP1 is near-surface southward advection of cold water upwelled in the northern SSUC. Daily and intradaily fluctuations are also present in the heat change signal particularly during the early (23-28 March) and to a lesser extent late (10-12 March) phases. The time scale of the fluctuations span a wide range of scales but periods of $\sim$ 20 mn or less dominate and reflect the importance of nonlinear internal waves (see next section).

Near-surface to bottom stratification evolution is similar to heat content although it peaks about one day before on 26 March and drops more rapidly at the onset of UP1 (Fig. 7d). We relate this to differences in the controlling processes. Indeed, the return of stronger winds enhances 3D turbulence levels and may erode stratification on a time scale of hours. In contrast, changes in heat content should be more progressive because enhanced winds reduce air-sea heat fluxes by a few tens of W m^{-2} only (given the range of wind fluctuations between RL1 and UP1) and lateral advection of colder waters requires at least one inertial period to produce some effects.

Non zero stratification ($> 0.5^o$C) is maintained during most of UP1. This is despite the fact that the mooring is located inshore of the main upwelling front during that period, as revealed in CTD transects T6 on 26 February, T10 on 2 March and T13 on 7 March (see Fig. 5 and Fig. 6). There are only two brief moments when the water column is fully mixed

or very near so, on 1 and 7 March. Winds measured by the ship at these times near M28 are the strongest observed during the entire period (Fig. 2d).

Bottom temperature evolution during the early UP1 period (between 26 February and 1 March) shows a pronounced increase $\sim 0.5^o$C. This suggests that the initial response to increasing winds (enhanced mixing) remains perceptible for 3-4 days at M28. Alternatively warmer bottom waters may have been present north of M28 and the temperature evolution would simply result from their southward advection but T5 and T8 temperature sections (Fig. 5) are not particularly supportive of this. More generally, bottom temperature evolution at M28 illustrates the slow and complex response of bottom layer properties to the upwelling wind history: coldest bottom temperatures coincide with the maximum relaxation during RL1 and also with the very end of UP1 and onset of RL2 (the return of the cold bottom water variety found on 25 February only occurs on 10 March). Conversely, warmest temperatures are found after 8 days of sustained upwelling at the time when coldest surface temperatures are recorded in the system (Fig. 2b). The long inertial time period (of the order of two days at the SSUC latitude) and the shelf width are two important factors that must contribute to the delays and decouplings between the onset of an upwelling-favorable wind event, cold water flowing over the shelf break, and that water reaching the M28 mid-shelf region. In turn, because the flushing of bottom water takes more time than, *e.g.,* relaxation RL1 lasts, the shelf thermohaline structure integrates the history of a succession of upwelling events (such as UP0 and UP1).

Mid-shelf alongshore currents (Fig. 8 at RDIE) essentially reflect the RL1/UP1/RL2 succession of events with northward flow around 26 February and toward the end of the period (note that northward surface flows are only found in the core of RL2 with maximum

intensity 0.1 m s^{-1}). Southward flow prevails in between, with two surface peaks $\sim$ at approx. 0.4 m s^{-1} in conjunction with the well-mixed conditions on 1 and 7 March. Some important flow subtleties can also be noted.

Most surprisingly, a weak relaxation of the southward flow at RDIE stands out from 3 to 5 March. Alongshore currents do not reverse at RDIE but they do at RDIW and AQDI where the northward flow remains modest nonetheless, below 5 cm s^{-1} (not shown). Because the ship was not at sea during this time period we lack contextual information to interpret these changes and simply mention that wind intensity reduced slightly after 1 March (Fig. 2a) which may have been sufficient to trigger the southward flow relaxation. A similar explanation may be invoked to explain the timing of the alongshore current relaxation initiated around 9 March, *i.e.,* several days prior to the major wind drop but coincident with what appears as a limited wind reduction based on DWS and ship atmospheric informations (Fig. 2)a and d).

Cross-shore velocities evolutions have generally been more difficult to interpret than alongshore ones (Lentz and Chapman 2004). Subsurface cross-shore velocities are directed onshore during the entire UP1 period but also during RL1. During the first part of RL2 when RDIE is still moored the current alternates between onshore and offshore with a period $\sim$ 2 days suggestive of near-inertial oscillations (Millot and Crépon 1981). Cross-shore velocities are essentially offshore in the surface boundary layer. They are strongest during UP1 except for a short inversion to onshore coincident with the second time period when the water column is fully destratified. The first destratification episode (1 March) also coincides with reduced offshore flow near the surface. In both cases enhanced turbulent diffusion of momentum at times of intense mixing are likely responsible for the anomalous

onshore surface flow.

The largest cross-shore velocities are found at mid-depth on 26-27 February, *i.e.,* at a time when winds have started increasing moderately at DWS (wind evolution at M28 is less clear, see Fig. 2a and d) and the alongshore flow is not established to equatorward yet. The duration of this onshore pulse is too long to be consistent with a wind-induced inertial oscillation. An alternative explanation is suggested by the sequence of MODIS SST images for 24,27 and 28 February (see Figs. 3b,c and 9). These images offer a detailed view of the mesoscale activity and its evolution during that period. On 27-28 February a warm MC meander that will subsequently form CVA-3 impinges on the shelf with its edge reaching the 30 m isobath. Comparison with the image for 24 February indicates that a rapid displacement of the meander crest toward the northeast (*i.e.,* toward the mooring area) has taken place over 2-3 days. Concomitantly the cold upwelling tongue undergoes a noticeable shoreward displacement (followed by a rapid offshore retreat). On 27 October it occupies a zone inshore of M28 at 14^oN (Fig. 9). The signature of a short-lasting onshore advection episode is also consistent with the temperature observations at M28 where a substantial lateral flux contribution is required to explain the heat content increase around that day (Fig. 7c).

Because R/V Antéa steamed multiple times across the mid- and outer-shelf in the latitude range 14^o-14^o10'N between 26 February 3AM and 28 February 0:30AM additional observations are available to support the existence of a shelf-wide event of onshore flow driven by mesoscale activity. A cross-section of (u,v) velocities is obtained by averaging the ship ADCP measurements made during these transects. Data are binned using the native resolution of the ADCP in the vertical (8 m bins; the uppermost is centered at -19 m) and

a 0.025^o mesh size in longitude. The ADCP configuration used 5 min ensemble averaging. All the ensembles for a given transect falling into one 0.025^o longitude bin are pre-averaged and contribute for only one observation. We did not try to weight the transects so as to minimize the influence of tidal currents (*e.g.,* as done in Avicola et al. 2007) but we have verified that tidal phases are such that substantial canceling is happening in the averaging (which is only important for u given the shape of tidal ellipses, not shown). The result is shown in Fig. 9a,b and allows us to place the mooring observations around 27 February in a broader across-shore perspective. During this period subsurface currents over most of the shelf are toward the northeast. Onshore velocities reach 20 cm s^{-1} over the outer shelf with a maximum positioned at mid-depth. Onshore velocities remain $\sim$ 10 cm s^{-1} as close to shore as the ship ADCP can measure. (Closer to shore RDIW and RDIE velocities are also around 10 cm s^{-1}.) Inspection of all available ship ADCP transects near 14^oN confirm the unusual intensity of this onshore flow. Intense poleward currents as those depicted in Fig. 9b) are more commonly observed although they are generally more confined to the slope and outer shelf area.

SST images during the UPSEN2/ECOAO (and at other times) clearly show the frequent incursion of MC mesoscale meanders and eddies onto the shelf. These are presumably the manifestations of instability modes for the system formed by the poleward current and the equatorward upwelling flow. Based on the evidences described above we see the episode of onshore flow on 26-27 February as related to such a mesoscale event. The unstable behavior of a shelf/slope current system has recently been studied in the downwelling case (Wang and Jordi 2011). Our observational results highlight the need to perform a similar study in the context of upwelling systems. This would help explore and clarify the interactions between

the shelf upwelling jet and the slope current, the influence of the wind in modulating these interactions, and most importantly, the conditions under which mesoscale perturbations penetrate deeply into the shelf.

4. The SSUC internal wave field

Internal gravity waves are well known contributors to mixing in the coastal ocean. The accepted view is that internal tides generated at the shelf break tend to evolve nonlinearly and give rise to shorter-scale internal waves as they propagate nearshore. Steepening and breaking (Moum et al. 2007, 2003; Lamb 2014) is inherent to the propagation toward shallower waters but the subinertial environment can also enhance dissipation, *e.g.,* through mutually reinforcing shears (Avicola et al. 2007). This latter study indicates that, over the Oregon shelf, internal wave breaking has a modest impact on vertical fluxes of tracers, a conclusion also reached by Schafstall et al. (2010) for the central Mauritania outer shelf region, just a few degrees north of the SSUC.

Isolated satellite measurements suggest that the SSUC is also subjected to IGW wave activity (*e.g.,* Jackson and Apel 2009). In this section we describe circumstancial evidences that SSUC IGW activity was ubiquitous during UPSEN2 and ECOAO and that its intensity was at times very strong (Sec. 4a. Because we did not have any microstructure sensor onboard no reliable local dissipation estimates is available. On the other hand, our observations point to the importance of mixing, not only near the bottom where frictional effects may be implicated but also in the intermediate part of the water column where significant water mass transformation is revealed by CTD casts (Figs. 5 and 6, *e.g.,* CTDs 55-56 in T5; 108-111 in

T10). In addition, mid-shelf observations from moored instruments are used to estimate the energy associated with wave packets, which seems enough to influence the evolution of the upwelling front region (Sec. 4b).

a. Circumstantial evidences

ANTEA is equipped with a 4 frequencies EK60 echosounder (see Sec. 2). Inspection of all available echograms indicates ubiquitous nonlinear internal wave activity over the southern Senegal shelf. These waves manifest themselves as depressions of the main thermocline located in the vertical at about 1/3 of the water depth. Maximum crest to trough amplitude frequently reach 40 m or more over the outer shelf (see Fig. 10). Short internal waves (wavelengths of a few hundred meters) are embedded into longer waves (wavelengths around 10 km) as in situations where internal tides undergo fission (Gerkema 1996; Li and Farmer 2011).

Beside visual resemblance between the patterns exhibited in Fig. 10 and commonly observed internal gravity waves, both yoyo CTDs and Scanfish observations at constant depth confirm that echograms reflect displacements of the thermocline associated with time periods of a few minutes and amplitudes of tens of meters. Several yoyo CTDs were performed in the hope that they would help quantify mixing intensity. One took place on 25 February at 14^oN, 17^o20'W in about 60 m water depth as the leading edge of an internal tidal wave passed that location (Fig. 11a). A Thorpe scale analysis is performed on the 17 downcast profiles, following Thompson et al. (2007). Dominant salinity gradients are by far those associated with spikes induced by thermal lag in the conductivity sensor. As in Alford and Pinkel (2000)

we therefore compute Thorpe displacements and overturn scales based on temperature alone (see Fig. 11b-d).

The weakly stratified upper layer is where the largest Thorpe displacements and dissipations are found (as in Moum et al. 2007) with values occasionally reaching 10^{-5} W kg^{-1}. Much weaker dissipation maxima $\sim 10^{-7}$ W kg^{-1} are found in the lower half of the water column at that particular station. Mid-depth values one order of magnitude larger are obtained for one profile (not shown) carried out in the vicinity of CTD 89 (transect T8) where both temperature and salinity show conspicuous signs of interior mixing (see Fig. 5). Although many outer- and mid-shelf CTD profiles exhibit temperature staircases and overturns indicative of mixing the intensity of the underlying turbulence is however frequently too weak to be reliably quantified using standard CTD measurement. In particular, we are not able to diagnose systematic occurences of the IGW instability process studied by Moum et al. (2003).

b. Mid-shelf IGWs and their effect on the upwelling front

A different approach to IGW mixing relies on bulk estimates of IGW dissipated power over portions of the shelf (Jeans and Sherwin 2001). Depending on the SSUC thermohaline structure a fraction of the energy converted to baroclinic tides at the shelf break is able to propagate nearshore to the mid-shelf area. Sampling intervals of 2 moored ADCPs (2 mn for RDIW and RDIE) and thermistors mounted on M28 (1 mn) are adequate to resolve IGW activity when it is present. For example, the signature of wave packets is visible at M28 in temperature, mainly before 28 February and to a lesser extent after 10 March (Fig. 7).

In the remainder of the section, mooring data are used to compute 1) internal gravity wave energy at that location and, under some assumptions, 2) how much mixing can be achieved in the mid-shelf area where that energy can dissipate.

Given the observations at hand we choose to estimate the IGW energy flux F^w passing through M28 as $c_g \times (EKE^w + APE^w)$ where c_g is the speed at which wave trains propagate in the area and EKE^w (resp. APE^w) is the depth integrated kinetic (resp. available potential) energy associated with IGWs. This requires the definition of a low-pass operator $\overline{\cdot}$ such that high-pass deviations (denoted with a prime) adequately capture the flow and thermohaline fluctuations corresponding to the IGW activity. We use a running mean with flat averaging over time intervals of duration T_{lf} for $\overline{\cdot}$.

APE^w is quantified using the approach valid for arbitrary stratifications detailed in Holliday and McIntyre (1981) (see also Roullet and Klein 2009 and Kang and Fringer 2010):

$$APE^w(t) = \int_{-H}^{0} \left[\int_{z_r(\rho(z,t),t)}^{z} g\left(\rho - \rho_r^w(z',t)\right) dz' \right] dz \tag{1}$$

where $\rho_r^w(z,t)$ is the density profile of the reference state, $z_r^w(\rho)$ its bijection, *i.e.,* the equilibrium depth of a parcel of density ρ. Density reference states are determined by reordering density observations over overlapping time intervals of duration T_{lf}. Each resulting reference state is then used to compute APE^w(t) over a time subinterval of size T_{sub} smaller than T_{lf} (to limit edge effects). Choosing T_{lf} in the range [0.5 3] hours and T_{sub} from 1/3 to 1 T_{lf} does not reveal important sensitivities of either APE^w or EKE^w estimates. We present results for $\mathrm{T}_{lf} = 30$ mn and $\mathrm{T}_{sub} = 15$ mn.

EKE^w is quantified as

$$EKE^w(t) = \frac{1}{2}\rho \int_{-H}^{0} \left(u'^2 + v'^2 + w'^2\right) dz - EKE^{bg} \tag{2}$$

In this definition EKE^{bg} represents the non zero background value of the high-pass eddy kinetic energy found even during the period when the mooring is located inshore of the upwelling front and EKE^{w} may be due to other processes than internal gravity waves (including instrument noise) that we wish to exclude from the analysis. Based on Fig. 13 a conservative value for EKE^{bg} is 24 J m^{-2}. In practice vertical integration for APE^{w} and EKE^{w} does not cover the full water columns and only uses valid observations.

To determine c_g we estimate the delay between the arrival of particularly identifiable wavetrains at RDIW, M28 and RDIE. This method has inherent uncertainties because the wavetrains can be signicantly modified, particularly between RDIW and RDIE which are separated by $\sim$ 1 nm. c_g values are in the range 0.18-0.30 m s^{-1}. For the wavetrain shown in Fig. 12 the estimation is quite accurate between M28 and RDIE and leads c_g = 0.25 m s^{-1}, a central value we retain for further use below.

APE^{w} at M28 and $EKE^{w} + EKE^{bg}$ at RDIW are presented in Fig. 13 over the entire period of deployments. Several wave packets have clear signatures, both instantaneous and on average over a M2 period, particularly during RL1. For example between 24 February 8 PM and 25 February 8:30 AM (Fig. 12) the mean energy at the moorings is 20 J m^{-2} with a near exact equipartition between potential and kinetic wave energy. This yields F^{w}= 5 W m^{-1}, in line with mid- and inner-shelf values found off southern California (Lucas et al. 2011b) and Oregon (**?**). An interesting point of comparison can be obtained by computing the speed at which the wave energy can fully mix the water column at M28. During periods where the upwelling front is inshore M28 in its vicinity this should also be an estimate of the speed at which the upwelling front can migrate offshore under the influence of IGW mixing. To this end, we compute the potential energy excess E^{mix} required to destroy the

stratification present at M28 in the hours preceding the arrival of a given wave packet. E^{mix} values are in the range 300 to 450 J m^{-2} and close to 350 J m^{-2} on 24 February afternoon. Assuming a mixing efficiency $\gamma = 0.2$ (Osborn 1980) the time required to mix one across-shore meter of water column is $E^{mix}/(\gamma\, F^w) \approx 350$ s (per across-shore length unit). From this we obtain a order of magnitude for the speed c^w_{front} at which the upwelling front (or more precisely the well mixed region situated on its inshore flank) may be displaced offshore by IGW mixing, $c^w_{front} \approx 250$ m/day. This is modest and would translate into a 10 km offshore displacement over the duration of the field experiments. There are however several sources of uncertainties in the calculation that should be kept in mind. Perhaps most importantly, the internal wave field energy is estimated at M28 where it has already been strongly attenuated (through interactions with the bottom and also heterogeneities of the density field). An estimation performed farther offshore would result in larger F^w. On the other hand E^{mix} would also be larger so the outcome in terms of displacement of the front is unclear. During an earlier field experiment in March 2012 where only moored ADCP measurements are available EKE^w values of up to 30 J m^{-2} over a tidal period while E^{mix} is only marginally larger (UPSEN, Estrade et al, in preparation) so c^w_{front} may reach 1 km per day in some occasions.

The complications and uncertainties associated with the alongshore dimension should also be kept in mind. The manifestations of mixing observed at the central and southern transects result from a history of mixing along the 3D path of water parcels. These manifestations tend to be dominated by the presence of bulges of mixed water located immediately offshore of regions of strong SST gradients. This is particularly evident where upwelled and warm waters of offshore origin are in contact over the shelf (T6, T10 and to a lesser

extent T4). The pathway of the modified subsurface waters making up these bulges cannot be determined precisely. But general considerations on frontal dynamics suggest that this water may remain trapped in the frontal region while drifting alongshore and undergoing IGW mixing. Under upwelling favorable conditions slope waters should preferentially be upwelled onto the shelf in the northern SSUC (Crépon et al. 1984; Ndoye et al. 2014) and subsequently drift equatorward (Ndoye et al., manuscript in preparation), hence the weakest bottom salinities over the shelf found for T1 and T5 and the weaker signs of IGW mixing there. With these considerations in mind, the limitations of our eulerian estimate of IGW mixing potential at one particular location of the mid-shelf at 14^oN are evident. IGW trains with the largest amplitude ($\sim 70m$) found during UPSEN2/ECOAO were observed on 28 February around CTD 89 (T8) in 90-100 m water depth. The signature of mixing is noticeable on CTD profiles performed in the area shortly after their sight. That northern IGWs contribute to the formation of transformed waters present on 2 March in the frontal area near CTD 108-111 (approx 50 km to the south) cannot be determined but is consistent with ship ADCP measurements showing southward velocities over the shelf with velocities between 15 and 30 cm s^{-1}.

5. Conclusions

The present study is the first analysis of comprehensive physical in situ observations carried out in the SSUC. A number of findings complement and qualify previously known aspects of the SSUC dynamics.

The way the upwelling zone and front positions are established has previously been seen as a

consequence of the shutdown of surface Ekman transport in shallow waters, in a 2D vertical subinertial framework. Essential to the conceptual model is the assumption that momentum is vertically well mixed inshore of the upwelling zone so that wind and bottom friction equilibrate without involving the Coriolis force (Estrade et al. 2008). In this conceptual model it is wind strength which modulates the position of the front by affecting surface (Lentz 1992) and, more indirectly, bottom turbulence intensity. Overall, our continuous observations reveal that the water column is rarely destratified and momentum is not well mixed even tens of kilometers inshore of the upwelling front. Although the model may retain some validity at other times or on different time scales, other processes may be more important when trying to rationalize the functioning of upwelling over periods of a few weeks, and in particular where subsurface water is upwelled, which parts of the shelf it enriches and how the enriched area and its frontal edge may migrate across-shore with time. In the light of our analyses and findings we hypothesize that two key processes (with possible interplays between them) also play a systemic role in the functioning of the southern Senegal shelf upwelling.

First, the upwelling tongue and its frontal separation with the offshore waters is subjected to mesoscale disturbances which bring important non 2D effects. In the northern part of the system, a recurrent expression of mesoscale turbulence during UPSEN2/ECOAO was through $50 - 100$ km anticyclones that remained quasi-stationnary for one to a few weeks offshore of the Cape Verde peninsula. These Cape Verde anticyclones (CVAs) develop as meanders of the system formed by the Mauritanian current and shelf upwelling currents abut on the Cape Verde peninsula. CVAs have a clear influence on the shelf upwelling structure. They tend to confine the upwelling tongue inshore in the northern SSUC and promote off-

shore export in the surface layer near 14^oN. A better understanding of the unstable behaviors of the shelf/slope current system would be useful and in particular i) the conditions under which they can influence the shallow parts of the shelf (as around 27 February) ii) their preferential evolution sequences and their relation to the environmental conditions.

Another possibly important mechanism affecting the distribution of upwelling and the evolution of the frontal zone is mixing by internal tide dissipation over the shelf. To frame the issue, we find useful to examine the fast upwelling limit case exemplified by central California where w^{up} is classically tens of meters per day (Capet et al. 2004). In such a situation the upwelling process may be adequately pictured as adiabatic upward advection while vertical mixing and diabatic processes are ignored because they merely perform the unescapable incorporation of upwelling water into the mixed layer. That incorporation is tightly slaved to the vertical advection itself. Heterogeneities in vertical mixing, resulting from external processes (internal tide dissipation) or from heterogeneities directly associated with the upwelling dynamics (*e.g.,* nearshore wind drop-off) can only produce minute changes to where and when upwelling water is being entrained into the surface mixed layer. They also have a relatively limited time period during which they can act on upwelling water because w^{up} is large.

A radically different type of surface layer enrichment regime has been identified over some shelves where patchy episodes of vertical mixing triggered by inertia-gravity wave activity are the key process that incorporates subsurface water into the euphotic layer while unspecified adiabatic processes are in charge of renewing the pool of bottom water awaiting mixing with surface waters (Sharples et al. 2007; Williams et al. 2013; Tweddle et al. 2013) (see also Lucas et al. 2011b in which southern California internal tides are shown to be responsible

for the across-shelf replenishing flux of nutrients).

The SSUC situation uncovered during UPSEN2/ECOAO may represent an intermediate situation where partial decoupling between upwelling-driven vertical advection and mixing leads to bottom water incorporation in the surface layer through multiple sporadic mixing episodes. In the SSUC we expect the onshore flow to be strongest near the bottom (Lentz and Chapman 2004) and a scaling for upward velocities can thus be constructed as $w^{up} \sim u_b \times s$ where s is the bottom slope and u_b a typical near-bottom cross-shore velocity value. Based on mooring observations reported in this study and consistent with observations in other upwelling sectors $u_b \approx 5$ cm s^{-1}. Water parcels thus need around 10 days to travel from the shelf break to the mid-shelf upwelling zone and, with a shelf slope around 2 %, an estimate for w^{up} is 8 m d^{-1}. This provides ample time for mixing episodes to take place, along complex pathways that evolve under the influence of variable winds and mesoscale activity. As a result, upwelling dynamics may be more disrupted by IGWs in the SSUC than in other upwelling sectors (Schafstall et al. 2010; Avicola et al. 2007).

An unknown but presumably significant fraction of the energy driving mixing in the SSUC arises from the fission of internal tides into nonlinear internal waves that subsequently break and dissipate. The effect on tracer vertical fluxes is not known at present and depends on the distribution of IGW breaking aided by subinertial (Avicola et al. 2007) and possibly near-inertial, that was also observed during the experiment (Fig. 8) shear. Based on studies for other shelves this effect deserves careful attention. In particular, it would be interesting to know the extent to which IGW breaking contributes to the progressive enrichment of the shelf bottom layer in phytoplankton. [2]

[2]The significance of bottom layer enrichment for the SSUC ecosystem functioning is supported by the

Thermohaline heterogeneities efficiently contribute to the disruption of IGW propagation. During UPSEN2 and the beginning of ECOAO the upwelling front is well marked and impinges on the continental shelf. Preferential dissipation of IGWs in the offshore vicinity of the upwelling front is supported by many vertical profiles of tracers. This has potentially important dynamical implications. Additional observations will be needed to further evaluate the significance of IGWs "pounding" on the upwelling front in its tendency to migrate offshore. The tentative energetic analysis presented in Sec. 4 leads to upwelling front offshore displacements of a few hundred meters per day which is modest (*e.g.,* in regard to displacements associated with mesoscale disturbances) but uncertainties are large. A more qualitative element supporting the dynamical importance of IGW mixing is the sequence of satellite SST images during UPSEN2/ECOAO showing the progressive erosion of Cape Verde mesoscale anticyclones. Concomitant in situ observations reveal intense interior mixing undergone by the thermocline waters within the CVAs. In contrast, SST images do not reveal significant submesoscale frontal activity in comparison to other situations, hence lateral diffusive effects should be small (Capet et al. 2008b). Our interpretation is that CVAs bring substantial stratification over the shelf, which in turn allows IGWs to exist and presumably erode that stratification, *i.e.,* contribute to the CVA decay.

Fig. 14 helps summarize our main findings and results. The southern Senegal upwelling system is situated over a broad continental shelf. So far its study had overwhelmingly relied

calculation of a time scale associated with the phytoplankton bloom head start due to the enrichment of bottom waters. Chlorophyl bottom concentrations at the shelf break and over the stratified mid-shelf differ by one half to over one order of magnitude (Fig. 4) so this head start should be of several days, given exponential growth rates in the range 0.2-0.5 d^{-1} (Landry et al. 2009).

on satellite images and focused on long time scales (seasonal to interannual, *e.g.,* Lathuilière et al. 2008). The in situ observations we present reveal the complexity and variability of the upwelling structure and functioning, owing to synoptic wind variability, mesoscale effects and possibly mixing due to superinertial wave activity. The manifestations of mesoscale turbulence involve preferential and persistent patterns that connect the shelf and open ocean environment and impact the shelf upwelling dynamics.

Superinertial wave activity also seems important to the upwelling sector functioning. Our study provides strong indications that internal tides and non linear internal gravity waves can play a systemic role in the SSUC through water mass transformation and vertical flux of properties. In sustained upwelling conditions where most of the subsurface water feeding the coastal divergence enters the shelf area in the northern SSUC and subsequently flows southward (Ndoye et al., manuscript in preparation) we expect the stratification to be increasingly impacted by IGWs toward the south (*i.e.,* downstream with respect to the dominant shelf circulation), as we generally observe during UPSEN2-ECOAO. However, residence time scales over the southern Senegal shelf are comparable to those of synoptic variability. Water property modifications and biogeochemical activity thus take place along complex pathways that integrate the influence of synoptic wind variability, mesoscale and internal tide activity. How much of that complexity needs to be accounted for to properly understand the ecological functioning of the SSUC (*e.g.,* as a small pelagic nursery) and its long-term evolution will be the subject of future reseach.

Aknowledgements: genavir, captain and crew., B. Lecann, satellite products.

REFERENCES

Alford, M. H. and R. Pinkel, 2000: Observations of overturning in the thermocline: The context of ocean mixing. *J. Phys. Oceanogr.*, **30**, 805–832.

Allen, J., P. Newberger, and J. Federiuk, 1995: Upwelling circulation on the Oregon continental shelf. Part I: Response to idealized forcing. *J. Phys. Oceanogr.*, **25**, 18431866.

Arístegui, J., et al., 2009: Sub-regional ecosystem variability in the canary current upwelling. *Prog. Oceanog.*, **83**, 33–48.

Austin, J. A. and S. J. Lentz, 2002: The inner shelf response to wind-driven upwelling and downwelling*. *J. Phys. Oceanogr.*, **32**, 2171–2193.

Avicola, G., J. N. Moum, A. Perlin, and M. D. Levine, 2007: Enhanced turbulence due to the superposition of internal gravity waves and a coastal upwelling jet. *J. Geophys. Res.*, **112 (C6)**.

Barton, E., 1989: The poleward undercurrent on the eastern boundary of the subtropical North Atlantic. *Poleward Flows Along Eastern Ocean Boundaries*, Springer, 82–95.

Barton, E. D., 1998: Eastern boundary of the north atlantic: northwest africa and iberia. coastal segment (18, e). *The sea*, **11**, 633–657.

Barton, E. D., A. Huyer, and R. L. Smith, 1977: Temporal variation observed in the hydro-

graphic regime near Cabo Corveiro in the northwest African upwelling region, February to April 1974. *Deep Sea Res.*, **24 (1)**, 7–23.

Bretherton, F. P., R. E. Davis, and C. Fandry, 1976: A technique for objective analysis and design of oceanographic experiments applied to mode-73. *Deep Sea Res.*, **23**, 559–582.

Capet, X., F. Colas, P. Penven, P. Marchesiello, and J. C. McWilliams, 2008a: Eddies in eastern-boundary subtropical upwelling systems. *Ocean Modeling in an Eddying Regime*, M. Hecht and H. Hasumi, Eds., Am. Geophys. Union, Geophys. Monog. Ser., Vol. 177.

Capet, X., P. Klein, B. L. Hua, G. Lapeyre, and J. C. McWilliams, 2008b: Surface kinetic energy transfer in surface quasi-geostrophic flows. *J. Fluid Mech.*, **604**, 165–174.

Capet, X., P. Marchesiello, and J. C. McWilliams, 2004: Upwelling response to coastal wind profiles. *Geophys. Res. Lett.*, **31**, L13 311.

Crépon, M., C. Richez, and M. Chartier, 1984: Effects of coastline geometry on upwellings. *J. Phys. Oceanogr.*, **14**, 1365–1382.

Demarcq, H. and V. Faure, 2000: Coastal upwelling and associated retention indices derived from satellite sst. application to octopus vulgaris recruitment. *Oceanolo. Acta*, **23**, 391 – 408.

Estrade, P., P. Marchesiello, D. Verdière, A. Colin, and C. Roy, 2008: Cross-shelf structure of coastal upwelling: A twodimensional extension of Ekman's theory and a mechanism for inner shelf upwelling shut down. *J. Mar. Res.*, **66 (5)**, 589–616.

Gerkema, T., 1996: A unified model for the generation and fission of internal tides in a rotating ocean. *J. Mar. Res.*, **54**, 421–450.

Holliday, D. and M. E. McIntyre, 1981: On potential energy density in an incompressible, stratified fluid. *J. Fluid Mech.*, **107**, 221–225.

Jackson, C. and J. R. Apel, 2009: An atlas of internal solitary-like waves and their properties, second edition. URL `http://www.internalwaveatlas.com/Atlas_index.html`, URL `http://www.internalwaveatlas.com/Atlas_index.html`.

Jeans, D. and T. Sherwin, 2001: The evolution and energetics of large amplitude nonlinear internal waves on the portuguese shelf. *J. Mar. Res.*, **59**, 327–353.

Kang, D. and O. Fringer, 2010: On the calculation of available potential energy in internal wave fields. *J. Phys. Oceanogr.*, **40 (11)**, 2539–2545.

Kudela, R. M., et al., 2008: New insights into the controls and mechanisms of plankton productivity along the US West Coast. *Oceanography*, **21**, 46–59.

Lamb, K. G., 2014: Internal wave breaking and dissipation mechanisms on the continental slope/shelf. *Annu. Rev. Fluid Mech.*, **46**, 231–254.

Landry, M. R., M. D. Ohman, R. Goericke, M. R. Stukel, and K. Tsyrklevich, 2009: Lagrangian studies of phytoplankton growth and grazing relationships in a coastal upwelling ecosystem off Southern California. *Prog. Oceanog.*, **83**, 208–216.

Lathuilière, C., V. Echevin, and M. Lévy, 2008: Seasonal and intraseasonal surface chlorophyll-a variability along the northwest african coast. *J. Geophys. Res.*, **113**.

Lentz, S. J., 1992: The surface boundary layer in coastal upwelling regions. *J. Phys. Oceanogr.*, **22**, 1517–1539.

Lentz, S. J. and D. C. Chapman, 2004: The importance of nonlinear cross-shelf momentum flux during wind-driven coastal upwelling. *J. Phys. Oceanogr.*, **34**, 2444–2457.

Li, Q. and D. M. Farmer, 2011: The generation and evolution of nonlinear internal waves in the deep basin of the south china sea. *J. Phys. Oceanogr.*, **41**, 1345–1363.

Lucas, A. J., C. L. Dupont, V. Tai, J. L. Largier, B. Palenik, and P. J. Franks, 2011a: The green ribbon: multiscale physical control of phytoplankton productivity and community structure over a narrow continental shelf. *Limnol. Oceanogr.*, **56**, 611–626.

Lucas, A. J., P. J. Franks, and C. L. Dupont, 2011b: Horizontal internal-tide fluxes support elevated phytoplankton productivity over the inner continental shelf. *Limnol. Oceanogr. Fluids Environ.*, **1 (1)**, 56–74.

Lucas, A. J., G. C. Pitcher, T. A. Probyn, and R. M. Kudela, 2014: The influence of diurnal winds on phytoplankton dynamics in a coastal upwelling system off southwestern africa. *Deep Sea Res.*, **101**, 50–62.

Marchesiello, P., X. Capet, and C. Menkes, 2011: Submesoscale turbulence in Tropical Instability Waves. *Ocean Model.*, **39**, 31–46.

Marchesiello, P., J. C. McWilliams, and A. Shchepetkin, 2003: Equilibrium structure and dynamics of the California Current System. *J. Phys. Oceanogr.*, **33**, 753–783.

Millot, C. and M. Crépon, 1981: Inertial oscillations on the continental shelf of the gulf of lions-observations and theory. *J. Phys. Oceanogr.*, **11**, 639–657.

Morison, J., R. Andersen, N. Larson, E. D'Asaro, and T. Boyd, 1994: The correction for thermal-lag effects in Sea-Bird CTD data. *J. Atm. Ocean Tech.*, **11**, 1151–1164.

Moum, J., D. Farmer, E. Shroyer, W. Smyth, and L. Armi, 2007: Dissipative losses in nonlinear internal waves propagating across the continental shelf. *J. Phys. Oceanogr.*, **37**, 1989–1995.

Moum, J., D. Farmer, W. Smyth, L. Armi, and S. Vagle, 2003: Structure and generation of turbulence at interfaces strained by internal solitary waves propagating shoreward over the continental shelf. *J. Phys. Oceanogr.*, **33**, 2093–2112.

Ndoye, S., C. X, E. P, S. BA, D. D, L. A, G. AT, and P. Brehmer, 2014: SST patterns and dynamics of the Southern Senegal-Gambia upwelling center. *J. Geophys. Res.*, in press.

Osborn, T., 1980: Estimates of the local rate of vertical diffusion from dissipation measurements. *J. Phys. Oceanogr.*, **10**, 83–89.

Pawlowicz, R., B. Beardsley, and S. Lentz, 2002: Classical tidal harmonic analysis including error estimates in MATLAB using T_TIDE. *Computers & Geosciences*, **28**, 929–937.

Peña-Izquierdo, J., J. L. Pelegrí, M. V. Pastor, P. Castellanos, M. Emelianov, M. Gasser, J. Salvador, and E. Vázquez-Domínguez, 2012: The continental slope current system between Cape Verde and the Canary Islands. *Scien. Mar.*, **76**, 65–78.

Pitcher, G., F. Figueiras, B. Hickey, and M. Moita, 2010: The physical oceanography of

upwelling systems and the development of harmful algal blooms. *Prog. Oceanog.*, **85 (1)**, 5–32.

Roullet, G. and P. Klein, 2009: Available potential energy diagnosis in a direct numerical simulation of rotating stratified turbulence. *J. Fluid Mech.*, **624**, 45–55.

Roy, C., 1998: An upwelling-induced retention area off Senegal: a mechanism to link upwelling and retention processes. *South Afr. J. Mar. Sci.*, **19**, 89–98.

Ryan, J., et al., 2010: Recurrent frontal slicks of a coastal ocean upwelling shadow. *J. Geophys. Res.*, **115**.

Schafstall, J., M. Dengler, P. Brandt, and H. Bange, 2010: Tidal-induced mixing and diapycnal nutrient fluxes in the mauritanian upwelling region. *J. Geophys. Res.*, **115**.

Sharples, J., et al., 2007: Spring-neap modulation of internal tide mixing and vertical nitrate fluxes at a shelf edge in summer. *Limnol. Oceanogr.*, **52**, 1735–1747.

Strub, P. T., P. M. Kosro, and A. Huyer, 1991: The nature of the cold filaments in the california current system. *J. Geophys. Res.*, **96**, 14 743–14 768.

Thompson, A. F., S. T. Gille, J. A. MacKinnon, and J. Sprintall, 2007: Spatial and temporal patterns of small-scale mixing in drake passage. *J. Phys. Oceanogr.*, **37 (3)**, 572–592.

Tweddle, J. F., J. Sharples, M. R. Palmer, K. Davidson, and S. McNeill, 2013: Enhanced nutrient fluxes at the shelf sea seasonal thermocline caused by stratified flow over a bank. *Prog. Oceanog.*, **117**, 37–47.

Wang, D.-P. and A. Jordi, 2011: Surface frontogenesis and thermohaline intrusion in a shelfbreak front. *Ocean Model.*, **38**, 161–170.

Williams, C., J. Sharples, C. Mahaffey, and T. Rippeth, 2013: Wind-driven nutrient pulses to the subsurface chlorophyll maximum in seasonally stratified shelf seas. *Geophys. Res. Lett.*, **40**, 5467–5472.

Woodson, C., L. Washburn, J. A. Barth, D. Hoover, A. R. Kirincich, M. McManus, J. P. Ryan, and J. Tyburczy, 2009: Northern monterey bay upwelling shadow front: Observations of a coastally and surface-trapped buoyant plume. *J. Geophys. Res.*, **114**.

Woodson, C., et al., 2007: Local diurnal upwelling driven by sea breezes in northern Monterey Bay. *Cont. Shelf Res.*, **27**, 2289–2302.

List of Figures

2 a): Instantaneous (dashed) and low-passed filtered with one inertial period forward shift (black solid) meridional wind at DWS [m s^{-1}]. Gray rectangles delineate the periods with no in situ observations. b): MODIS zonal minimum of SST averaged meridionally over the northern SSUC (14^o-14^o30'N). Only nighttime images are used. This time series index is insensitive to cross-shore displacements of the upwelling zone. c): Longitude of the SST zonal minimum around 14^oN ($\pm$ 10'). Gray dots are estimated from MODIS cloud-free L2 images. Black diamonds are SST minima revealed TSG temperature measurements along the 14^oN transect. When secondary minima are found that are less than 0.1^oC (respectively 0.3^oC) they are also indicated with black (resp. open) diamonds. Longitude at M28 is indicated with a dashed line. d): 2 hourly averaged meridional wind measured by the ship weather station when the ship mean position is within 50 km from M28. ASCAT measurements within 50 km from M28 (area averaging) are also shown with daytime (resp. nighttime) data as red (resp. blue) crosses. e):diurnal wind cycle computed from all ship measurements made in the vicinity of M28 (50 km; arrows with gray lines). Morning and evening ASCAT winds for the same period and domain are also represented (two black arrows at 10:40AM and 10:40PM). In a)-d), absissa are days from the beginning of the month (Feb. or Mar.). 52

7 Top: Mid-shelf (M28) time series of temperature at 5 m (a), 28 m (b), depth integrated heat change (c ; relative to the average over the entire deployment period see text for details), near-surface (5 m) to bottom temperature difference (d) and time-depth temperature diagram (e). The time range represented in a) extends beyond the deployment period to represent MODIS SST (blue/red symbols for nighttime/daytime scenes). The dashed lines in c) represent heat content trends for a 1D ocean receiving a constant heat flux of 100 or 200 W m^{-2}. The frame delineated with black lines in e) represent the time interval used to compute the typical energy and mixing potential of internal gravity waves in the mid-shelf (Sec. 4b). 57

8 Mid-shelf (RDIE) time-depth diagram of zonal (*i.e.,* cross-shore u; top) and meriodional (*i.e.,* alongshore; bottom) subinertial currents [cm s^{-1}] over the entire deployment period. The white solid line represent the 0 isocontour. Note the different colorscales. 58

9 MODIS SST (top) and ship ADCP velocities (across-shore and along-shore) around the 27 February, during the episode of intense onshore flow. The number of transects contributing to every binned velocity data is also indicated (bottom). 59

10 Top: 70 kHz echograms obtained on 23 February between 2 and 6.20 AM while R/V ANTEA steamed eatward at a nearly constant speed $\sim$ 5 kt. High backscatter levels in yellow indicate the position of sharpest density gradients. They exhibit oscillations with wavelengths of the order of a few hundred meters embedded into longer internal tides (2 wavelength around 10 km are visible with troughts at 17.47^{o}W, 17.37^{o}W and 17.29^{o}W, and crests at 17.45^{o}W and 17.34^{o}W). Bottom: zoom over the time subinterval 3am to 3.40 am indicated by a grey rectable in the top panel. Bottom depth measured by the ship ADCP is indicated by a thick black line. 60

11 a): 70 kHz echograms obtained on 25 February between 5 and 5.40 AM while R/V ANTEA was in station around 14^{o}N, 17^{o}20'W. The position of the CTD is superimposed as white segments forming a zig-zag pattern. b-d): Profiles of temperature (b, with a 15^o shift between them), anomaly between the measured and stable reordered temperature profile (c, 0.15^{o}C shift), Thorpe displacement (d, the extremities of the segments below each profile indicate $\pm$ 5 m) and energy dissipation (e). In e) values below 10^{-8} are not shown. Also, only dissipation values for overturns with temperature amplitudes larger than 0.05^{o}C (for which the role of salinity can be neglected) are filled. 61

12 Time series of available potential energy (top) and temperature vertical profiles at M28 from 24 Feb. 18.20PM to 25 Feb. 4.20AM. during the period of clear IGW activity contributing to the mixing estimates in Sec. 4b). The x-axis scale is identical for the two panels. 62

14 3D schematic description of the upwelling dynamical and hydrological structure over the southern Senegal shelf, as observed during UPSEN2-ECOAO. The manifestation of upwelling takes the form of a cold SST tongue situated tens of kilometers away the shore. Its position and that of its offshore frontal edge are subjected to displacements that can be related to nearshore extensions of mesoscale disturbances. These mesoscale disturbances presumably arise from instabilities of the current system composed of the poleward flowing Mauritanian current and the equatorward upwelling currents. Ubiquitous internal gravity waves over the shelf are presumably implicated in substantial water mass transformation (and associated vertical fluxes of properties) that occur offshore of the upwelling zone. In particular interior mixing is frequently observed just offshore of the upwelling zone. Inshore of that zone, the classical 2D Ekman cell (onshore flow near the bottom, offshore flow in the surface layer) prevails. Therefore, the position of the upwelling zone may not solely result from the shutdown of the cross-shore Ekman driven circulation on its inshore flanck. Partial evidences suggest that IGW breaking may contribute to the offshore migration of the front in UPSEN2-ECOAO type situations. We hypothesize that the sharpness of the front separating upwelling and offshore waters is primarily controlled by IGW mixing in the front area as opposed to submesoscale frontal instabilities (which have no evident signature in high-resolution SST images). 64

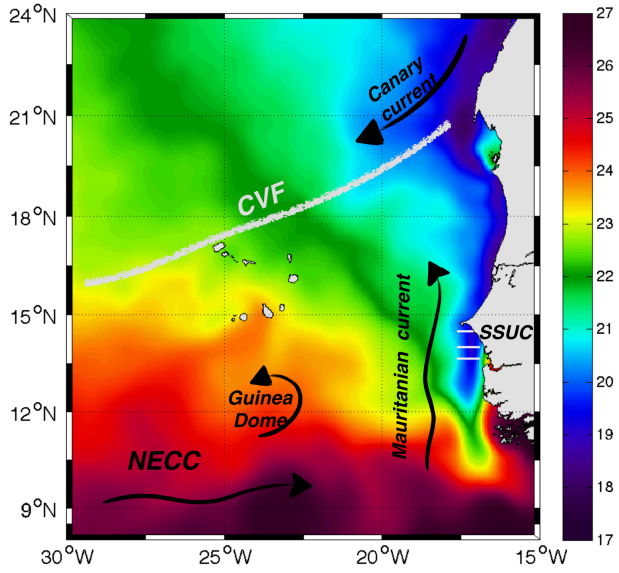

FIG. 1. Averaged OSTIA composite SST over the northeastern tropical Atlantic for the period 21 February - 18 March 2013 corresponding to the UPSEN2-ECOAO field experiments. Superimposed is a schematic representation of the main circulation features of the region including the North Equatorial counter-current (NECC) and the Cape Verde Frontal zone (CVF, thick gray). Our study area, the southern Senegal upwelling center (SSUC), stands out as the tip of the coastal upwelling system. White lines indicate the location of our three main hydrological transects.

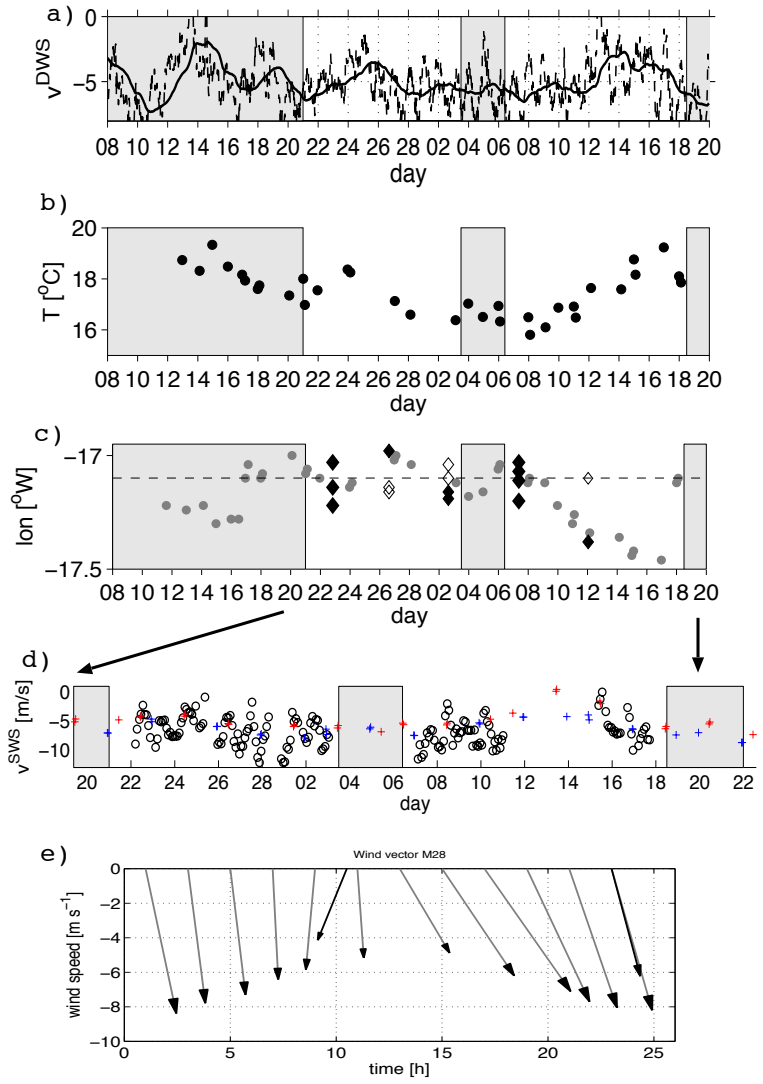

FIG. 2. a): Instantaneous (dashed) and low-passed filtered with one inertial period forward shift (black solid) meridional wind at DWS [m s^{-1}]. Gray rectangles delineate the periods with no in situ observations. b): MODIS zonal minimum of SST averaged meridionally over the northern SSUC (14^o-14^{o}30'N). Only nighttime images are used. This time series index is insensitive to cross-shore displacements of the upwelling zone. c): Longitude of the SST zonal minimum around 14^{o}N ($\pm$ 10'). Gray dots are estimated from MODIS cloud-free L2 images. Black diamonds are SST minima revealed TSG temperature measurements along the 14^{o}N transect. When secondary minima are found that are less than 0.1^{o}C (respectively 0.3^{o}C) they are also indicated with black (resp. open) diamonds. Longitude at M28 is indicated with a dashed line. d): 2 hourly averaged meridional wind measured by the ship weather station when the ship mean position is within 50 km from M28. ASCAT measurements within 50 km from M28 (area averaging) are also shown with daytime (resp. nighttime) data as red (resp. blue) crosses. e):diurnal wind cycle computed from all ship measurements made in the vicinity of M28 (50 km; arrows with gray lines). Morning and evening ASCAT winds for the same period and domain are also represented (two black arrows at 10:40AM and 10:40PM). In a)-d), absissa are days from the beginning of the month (Feb. or Mar.).

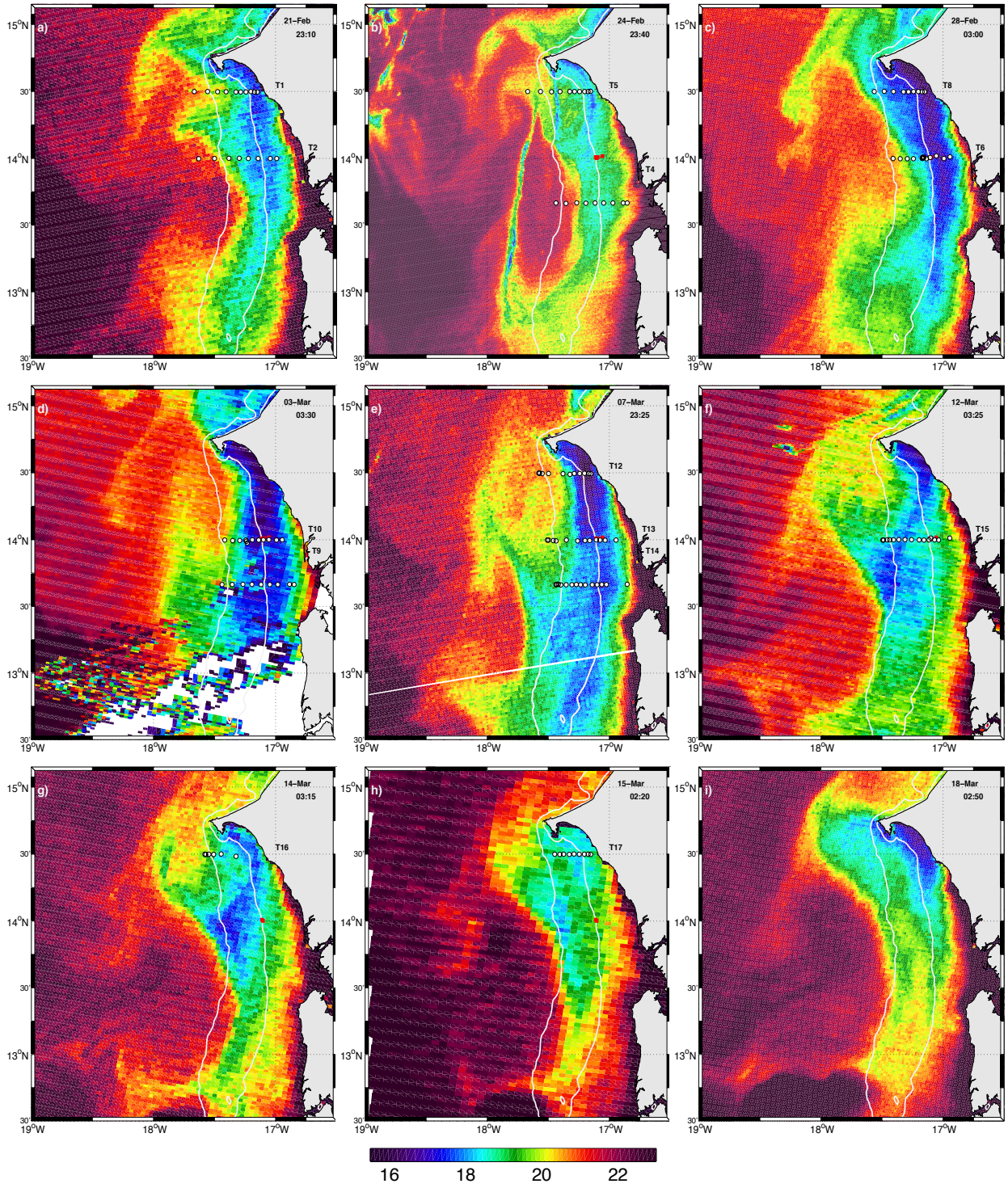

FIG. 3. MODIS SST at different times (given in the upper right corner of each image) during the UPSEN2/ECOAO cruises. CTD transects carried out within 1.5 day (prior or after) of the scene are indicated with white dots and labeled on land. Mooring locations are indicated with red square markers when they are deployed at the time of the scene (indicated in the upper right corner). 30 m and 100 m isobath are shown with white lines. The latter adequately defines the shelf break. Small areas possibly contaminated by clouds are not flagged, *e.g.*, along the line that joins (18°W,13°30'N and the Cape Verde peninsula in panel b).

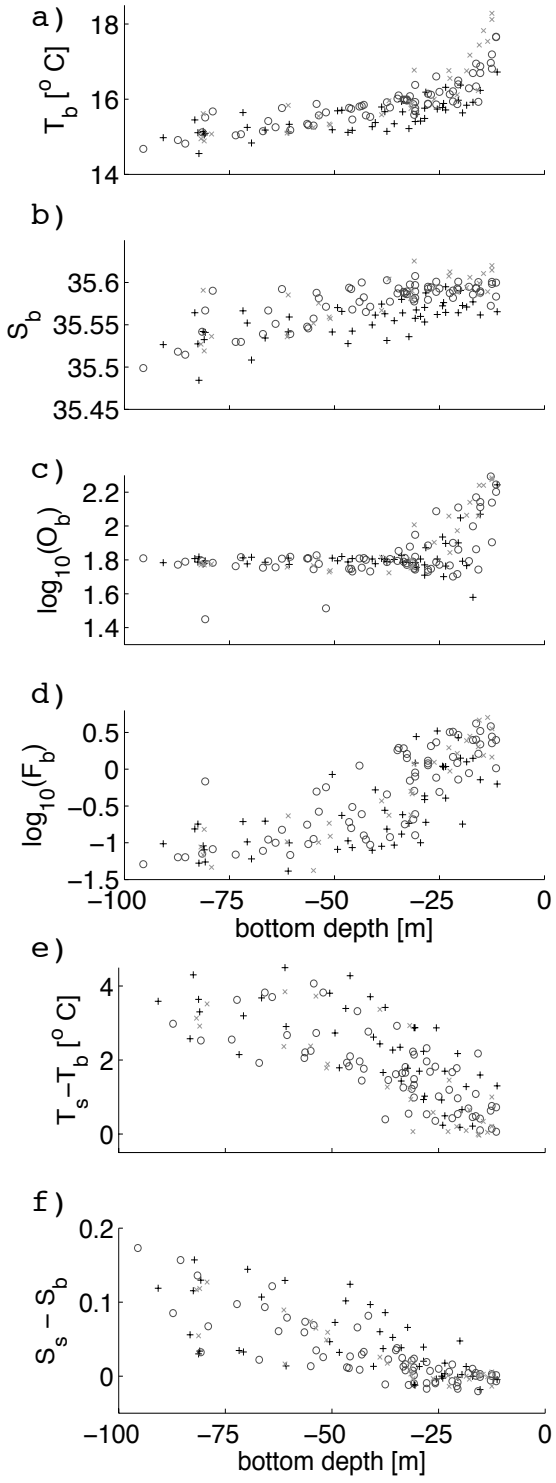

FIG. 4. Bottom temperature (a), salinity (b), dissolved oxygen (c, log scale) and fluorescence (d, log scale) for all CTD casts along the northern (+), central (circles) and southern (x) transects carried out during UPSEN2 and ECOAO. Near-surface (5 m) to bottom temperature (e) and salinity (f) are also shown.

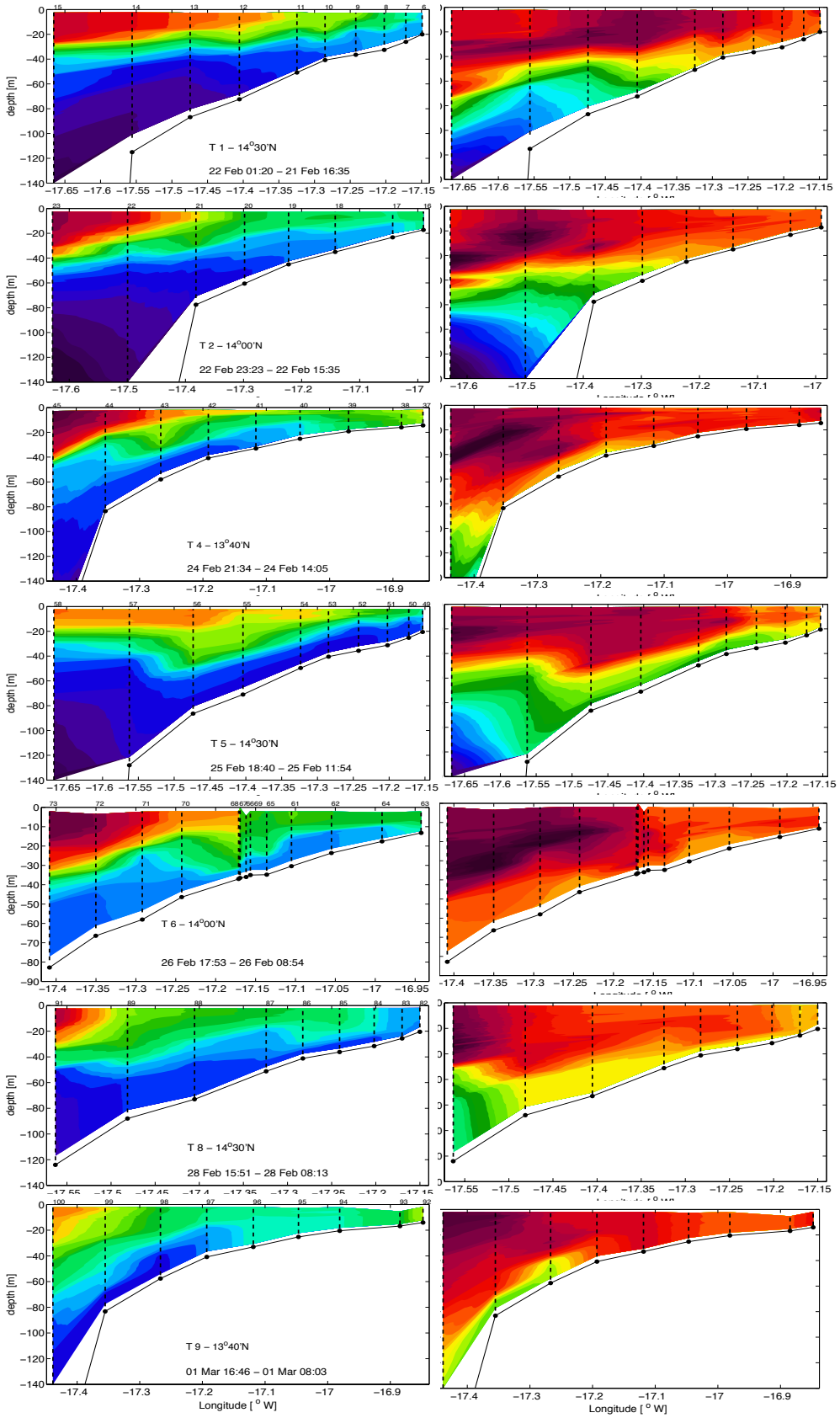

FIG. 5. Temperature (left) and salinity (right) CTD transects.

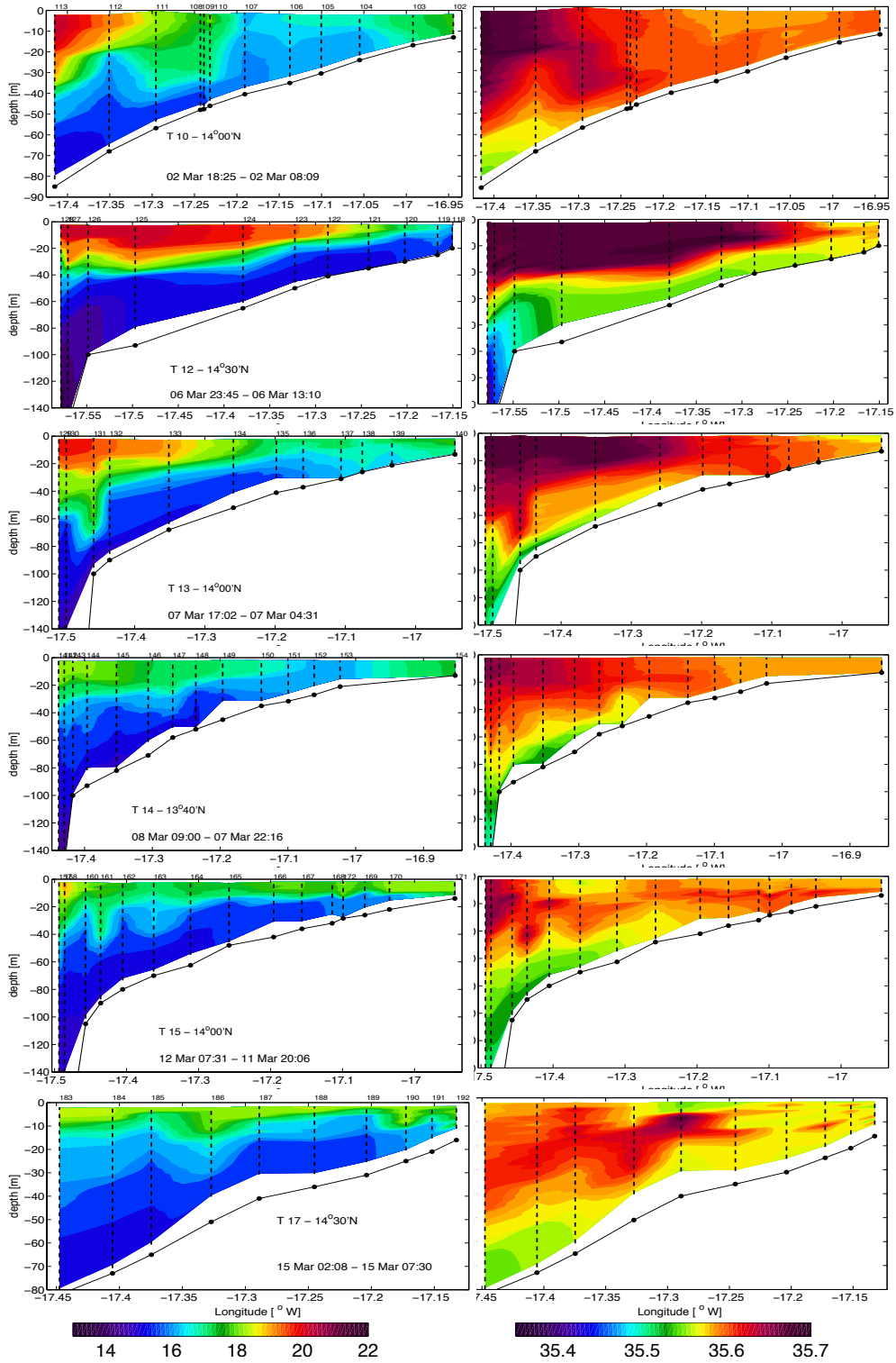

FIG. 6. Temperature (left) and salinity (right) CTD transects. Exact longitude range and maximum depth vary. Exact locations of CTD casts is shown with dashed lines above which the CTD number is given. Transect number, corresponding latitude and time period are indicated in each temperature section in the blanked area below the ocean floor.

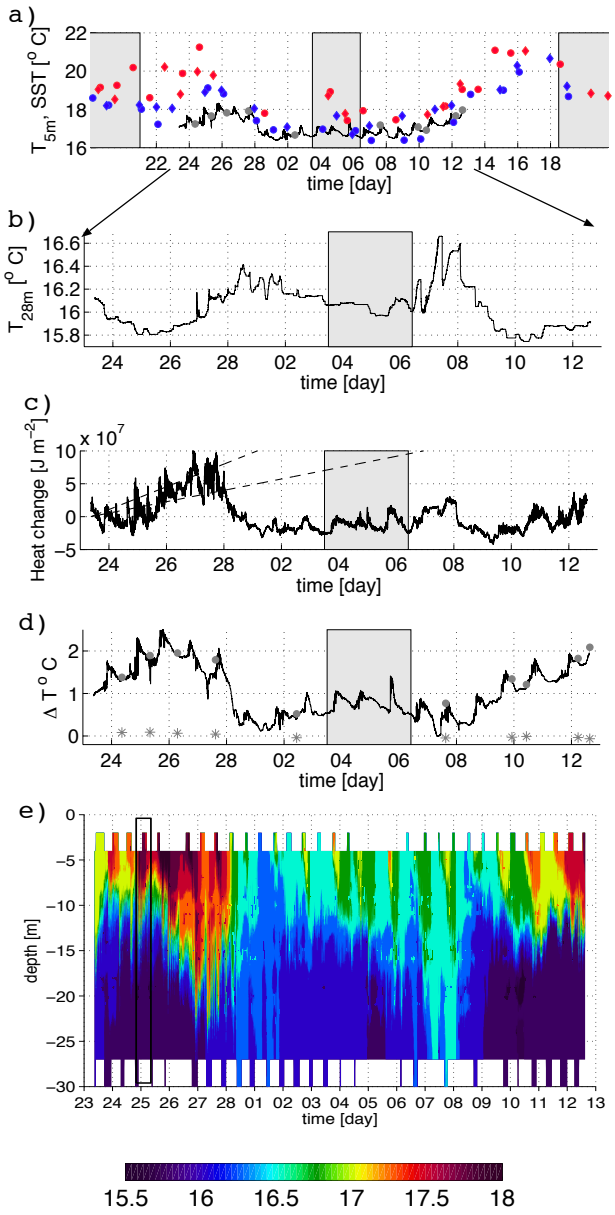

FIG. 7. Top: Mid-shelf (M28) time series of temperature at 5 m (a), 28 m (b), depth integrated heat change (c ; relative to the average over the entire deployment period see text for details), near-surface (5 m) to bottom temperature difference (d) and time-depth temperature diagram (e). The time range represented in a) extends beyond the deployment period to represent MODIS SST (blue/red symbols for nighttime/daytime scenes). The dashed lines in c) represent heat content trends for a 1D ocean receiving a constant heat flux of 100 or 200 W m^{-2}. The frame delineated with black lines in e) represent the time interval used to compute the typical energy and mixing potential of internal gravity waves in the mid-shelf (Sec. 4b).

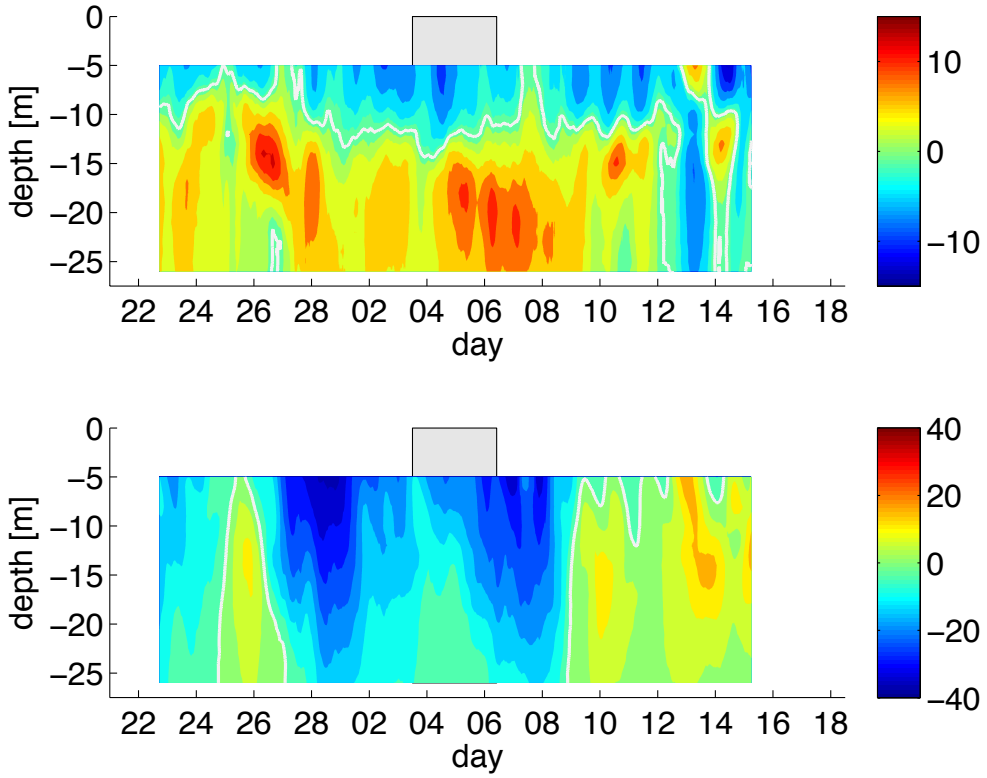

FIG. 8. Mid-shelf (RDIE) time-depth diagram of zonal (*i.e.,* cross-shore u; top) and meridional (*i.e.,* alongshore; bottom) subinertial currents [cm s^{-1}] over the entire deployment period. The white solid line represent the 0 isocontour. Note the different colorscales.

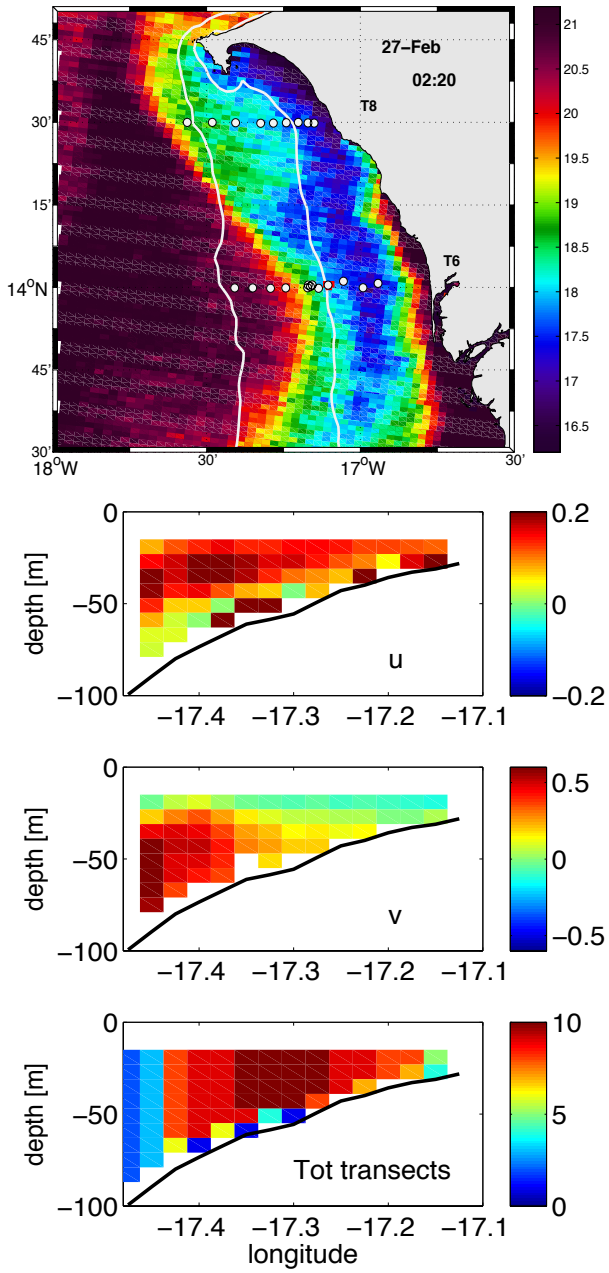

FIG. 9. MODIS SST (top) and ship ADCP velocities (across-shore and along-shore) around the 27 February, during the episode of intense onshore flow. The number of transects contributing to every binned velocity data is also indicated (bottom).

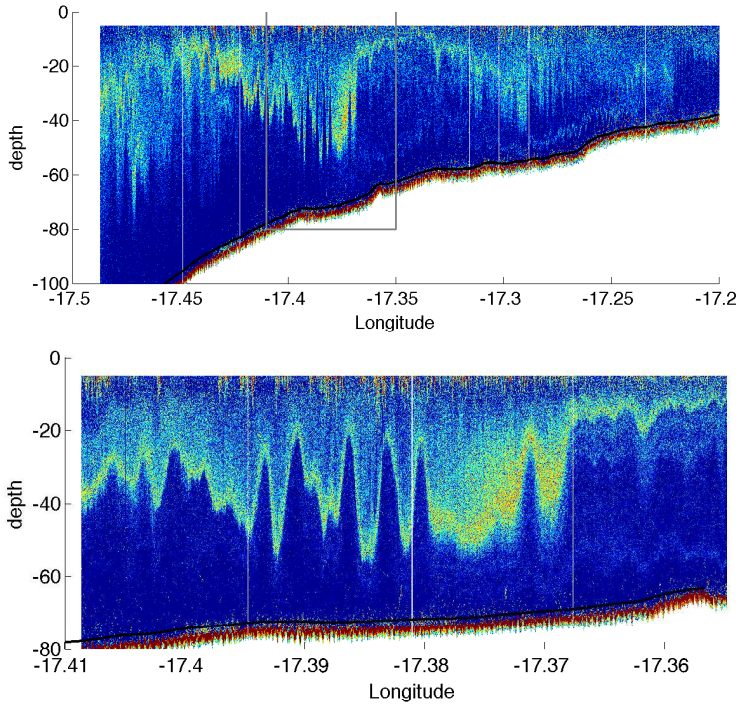

FIG. 10. Top: 70 kHz echograms obtained on 23 February between 2 and 6.20 AM while R/V ANTEA steamed eatward at a nearly constant speed $\sim$ 5 kt. High backscatter levels in yellow indicate the position of sharpest density gradients. They exhibit oscillations with wavelengths of the order of a few hundred meters embedded into longer internal tides (2 wavelength around 10 km are visible with troughts at 17.47^{o}W, 17.37^{o}W and 17.29^{o}W, and crests at 17.45^{o}W and 17.34^{o}W). Bottom: zoom over the time subinterval 3am to 3.40 am indicated by a grey rectable in the top panel. Bottom depth measured by the ship ADCP is indicated by a thick black line.

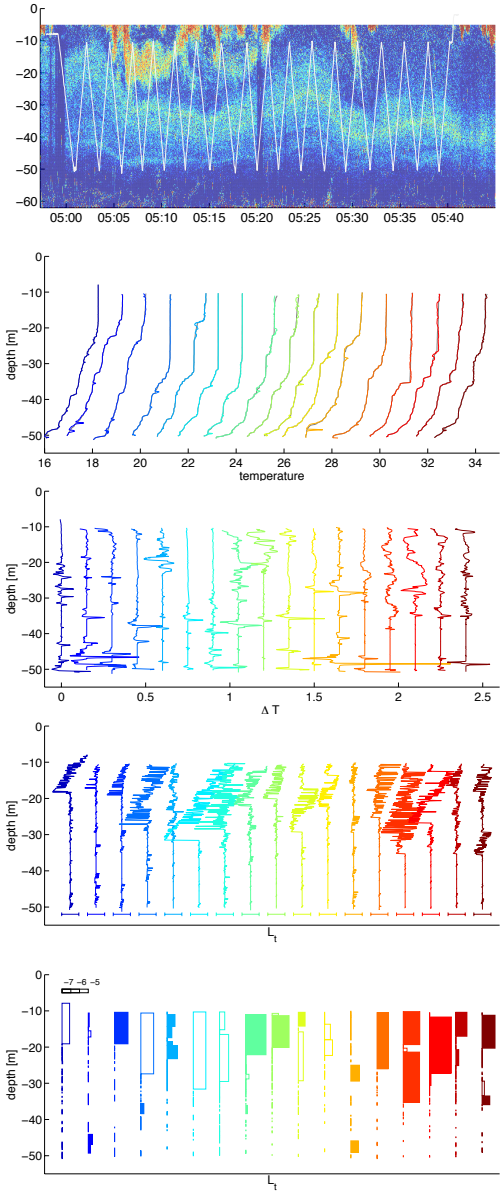

FIG. 11. a): 70 kHz echograms obtained on 25 February between 5 and 5.40 AM while R/V ANTEA was in station around 14ºN, 17º20'W. The position of the CTD is superimposed as white segments forming a zig-zag pattern. b-d): Profiles of temperature (b, with a 15^o shift between them), anomaly between the measured and stable reordered temperature profile (c, 0.15^oC shift), Thorpe displacement (d, the extremities of the segments below each profile indicate $\pm$ 5 m) and energy dissipation (e). In e) values below 10^{-8} are not shown. Also, only dissipation values for overturns with temperature amplitudes larger than 0.05^oC (for which the role of salinity can be neglected) are filled.

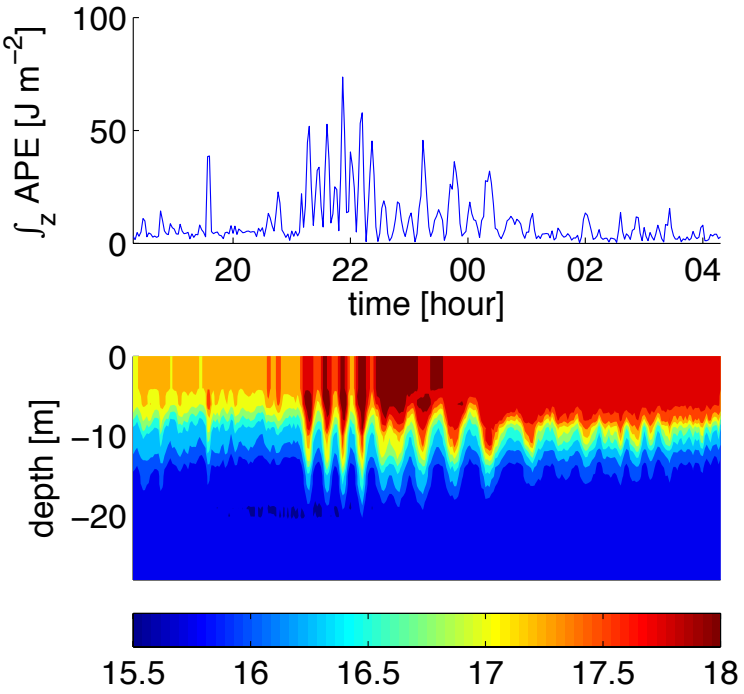

FIG. 12. Time series of available potential energy (top) and temperature vertical profiles at M28 from 24 Feb. 18.20PM to 25 Feb. 4.20AM. during the period of clear IGW activity contributing to the mixing estimates in Sec. 4b). The x-axis scale is identical for the two panels.

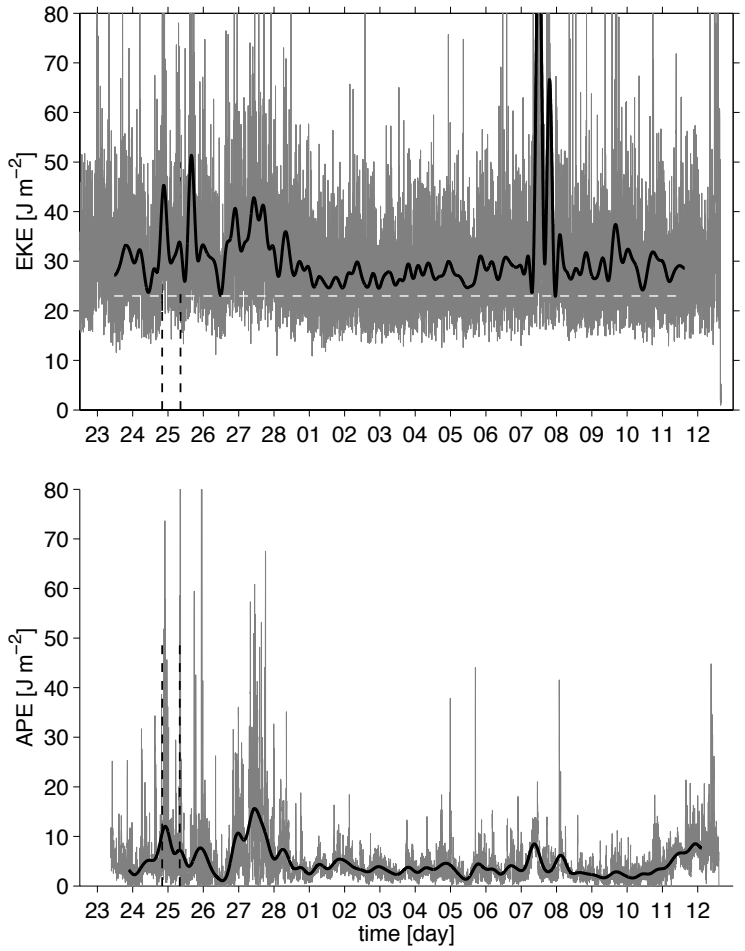

FIG. 13. Time series of (top) eddy kinetic energy EKE^w and (bottom) available potential energy (EKE^w+EKE^{bg}) at M28. In both cases unfiltered (thin gray) and low-passed (lanczos filter with cut-off at the M2 frequency, black) signals are shown. Lower signal to noise ratio for the ADCP observations is evident. For the EKE panel, the background level EKE^{bg} is shown with a white dashed line. The time interval 24 February 8PM - 25 February 8:30 AM chosen to estimate IGW mixing in Sec. 4b is indicated with black dashed lines.

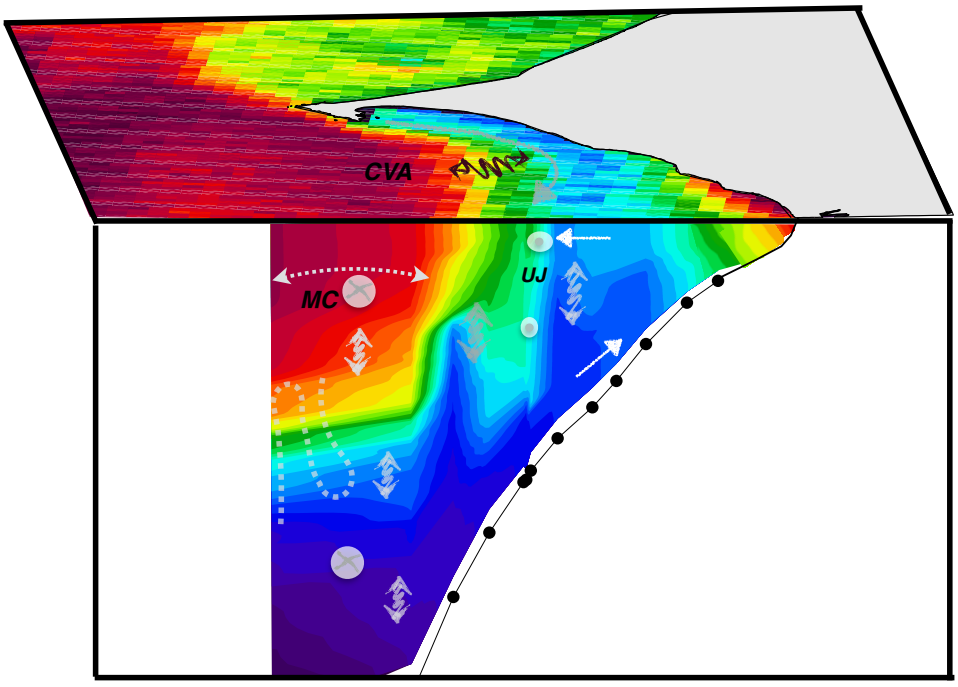

FIG. 14. 3D schematic description of the upwelling dynamical and hydrological structure over the southern Senegal shelf, as observed during UPSEN2-ECOAO. The manifestation of upwelling takes the form of a cold SST tongue situated tens of kilometers away the shore. Its position and that of its offshore frontal edge are subjected to displacements that can be related to nearshore extensions of mesoscale disturbances. These mesoscale disturbances presumably arise from instabilities of the current system composed of the poleward flowing Mauritanian current and the equatorward upwelling currents. Ubiquitous internal gravity waves over the shelf are presumably implicated in substantial water mass transformation (and associated vertical fluxes of properties) that occur offshore of the upwelling zone. In particular interior mixing is frequently observed just offshore of the upwelling zone. Inshore of that zone, the classical 2D Ekman cell (onshore flow near the bottom, offshore flow in the surface layer) prevails. Therefore, the position of the upwelling zone may not solely result from the shutdown of the cross-shore Ekman driven circulation on its inshore flanck. Partial evidences suggest that IGW breaking may contribute to the offshore migration of the front in UPSEN2-ECOAO type situations. We hypothesize that the sharpness of the front separating upwelling and offshore waters is primarily controlled by IGW mixing in the front area as opposed to submesoscale frontal instabilities (which have no evident signature in high-resolution SST images).